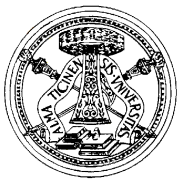

Dottorato di Ricerca in Ingegneria Civile
Graduate School in Civil Engineering

Sede: Facoltà di Ingegneria - Università di Pavia - via Ferrata 1 – 27100 Pavia – Italy

Dottorato di Ricerca in Ingegneria Civile X Nuova serie (XXIV Ciclo)

Experimental and numerical analysis of a confined two-phase turbulent jet system

Tesi di Dottorato
Ing. Emanuela Torti

Relatore:
Prof. Stefano Sibilla

Controrelatore:
Prof. Mario Gallati

Pavia, Ottobre 2011

Alla mia famiglia

Dottorato di Ricerca in Ingegneria Civile
Graduate School in Civil Engineering

Settore: **Field:**	Ingegneria Engineering
Sede Amministrativa non consortile: **Administrative location:**	Università degli Studi di PAVIA University of Pavia
Durata: **Duration:**	3 anni 3 years
Periodo formativo estero: **Period in foreign organization:**	come previsto dal regolamento del Dottorato di Ricerca as required by the school's rules
Numero minimo di corsi: **Minimum number of courses:**	6 6

Recapiti - Addresses

Dipartimento di Meccanica Strutturale
via Ferrata 1 - 27100 Pavia - Italy
Tel. +39 0382 / 505458 Fax +39 0382 / 528422

Dipartimento di Ingegneria Idraulica e Ambientale
via Ferrata 1 - 27100 Pavia - Italy
Tel. +39 0382 / 505300 Fax +39 0382 / 505589

Coordinatore - Coordinator

CASCIATI Fabio - Professore Ordinario di Scienza delle Costruzioni (ICAR/08)

Dipartimento di Meccanica Strutturale
via Ferrata 1 - 27100 Pavia – Italy Tel. +39 0382 / 505458 Fax +39 0382 / 528422
e-mail: fabio@dipmec.unipv.it

Collegio dei Docenti – Teaching Staff

CIAPONI Carlo	Professore Straordinario (ICAR02)
DEL GROSSO Andrea	Professore Ordinario, UniGe (ICAR/08)
FARAVELLI Lucia	Professore Ordinario (ICAR/08)
GALLATI Mario	Professore Ordinario (ICAR/01)
GOBETTI Armando	Professore Associato (ICAR/08)
MOISELLO Ugo	Professore Ordinario (ICAR/02)
PAPIRI Sergio	Professore Associato (ICAR/02)
SALA Roberto	Professore Associato (ING-IND/08)
MARCELLINI Alberto	Dirigente di ricerca. CNR - Milano

Organizzazione del corso

Il dottorato di ricerca in *Ingegneria Civile* presso la Scuola di Dottorato in Scienze dell'Ingegneria dell'Università degli Studi di Pavia è stato istituito nell'anno accademico 1994/95 (X ciclo).

Il corso consente al dottorando di scegliere tra quattro curricula: idraulico, sanitario, sismico e strutturale. Il dottorando svolge la propria attività di ricerca presso il Dipartimento di Ingegneria Idraulica e Ambientale, per i primi due curricula, o quello di Meccanica Strutturale per gli ultimi due.

Durante i primi due anni sono previsti almeno sei corsi, seguiti da rispettivi esami, che il dottorando è tenuto a sostenere. Il Collegio dei Docenti, composto da professori dei due Dipartimenti e da alcuni esterni all'Università di Pavia, organizza i corsi con lo scopo di fornire allo studente di dottorato opportunità di approfondimento su alcune delle discipline di base per le varie componenti. Corsi e seminari vengono tenuti da docenti di Università nazionali ed estere.

Il Collegio dei Docenti, cui spetta la pianificazione della didattica, si è orientato ad attivare ad anni alterni corsi sui seguenti temi:

- Meccanica dei solidi e dei fluidi
- Metodi numerici per la meccanica dei solidi e dei fluidi
- Rischio strutturale e ambientale
- Metodi sperimentali per la meccanica dei solidi e dei fluidi
- Intelligenza artificiale

più corsi specifici di indirizzo.

Al termine dei corsi del primo anno il Collegio dei Docenti assegna al dottorando un tema di ricerca da sviluppare sotto forma di tesina entro la fine del secondo anno; il tema, non necessariamente legato all'argomento della tesi finale, è di norma coerente con il curriculum, scelto dal dottorando.

All'inizio del secondo anno il dottorando discute con il Coordinatore l'argomento della tesi di dottorato, la cui assegnazione definitiva viene deliberata dal Collegio dei Docenti.

Alla fine di ogni anno i dottorandi devono presentare una relazione particolareggiata (scritta e orale) sull'attività svolta. Sulla base di tale relazione il Collegio dei Docenti, "previa valutazione della assiduità e dell'operosità dimostrata dall'iscritto", ne propone al Rettore l'esclusione dal corso o il passaggio all'anno successivo.

Il dottorando può svolgere attività di ricerca sia di tipo teorico che sperimentale, grazie ai laboratori di cui entrambi i Dipartimenti dispongono, nonché al Laboratorio Numerico di Ingegneria delle Infrastrutture.

Il "Laboratorio didattico sperimentale" del Dipartimento di Meccanica Strutturale dispone di:

1. una tavola vibrante che consente di effettuare prove dinamiche su prototipi strutturali;
2. opportuni sensori e un sistema di acquisizione dati per la misura della risposta strutturale;
3. strumentazione per la progettazione di sistemi di controllo attivo e loro verifica sperimentale;
4. strumentazione per la caratterizzazione dei materiali, attraverso prove statiche e dinamiche.

Il laboratorio del Dipartimento di Ingegneria Idraulica e Ambientale dispone di:

1. un circuito in pressione che consente di effettuare simulazioni di moto vario;
2. un tunnel idrodinamico per lo studio di problemi di cavitazione;
3. canalette per lo studio delle correnti a pelo libero.

Course Organization

The Graduate School of Civil Engineering, a branch of the Doctorate School in Engineering Science, was established at the University of Pavia in the Academic Year of 1994/95 (X cycle). The School allows the student to select one of the four offered curricula: Hydraulics, Environment, Seismic engineering and Structural Mechanics. Each student develops his research activity either at the Department of Hydraulics and Environmental Engineering or at the Department of Structural Mechanics. During the first two years, a minimum of six courses must be selected and their examinations successfully passed. The Faculty, made by Professors of the two Departments and by internationally recognized scientists, organizes courses and provides the student with opportunities to enlarge his basic knowledge. Courses and seminars are held by University Professors from all over the country and abroad. The Faculty starts up in alternate years common courses, on the following subjects:

– solid and fluid mechanics,
– numerical methods for solid and fluid mechanics,
– structural and environmental risk,
– experimental methods for solid and fluid mechanics,
– artificial intelligence.

More specific courses are devoted to students of the single curricula.

At the end of each course, for the first year the Faculty assigns the student a research argument to develop, in the form of report, by the end of the second year; the topic, not necessarily part of the final doctorate thesis, should be consistent with the curriculum selected by the student. At the beginning of the second year the student discusses with his Coordinator the subject of the thesis and, eventually, the Faculty assigns it to the student. At the end of every year, the student has to present a complete report on his research activity, on the basis of which the Faculty proposes to the Rector his admission to the next academic year or to the final examination. The student is supposed to develop either theoretical or experimental research activities, and therefore has access to the

Department Experimental Laboratories, even to the Numerical Laboratory of Infrastructure

Engineering. The Experimental Teaching Laboratory of the Department of Structural Mechanics offers:

1. a shaking table which permits one to conduct dynamic tests on structural prototypes;
2. sensors and acquisition data system for the structural response measurements;
3. instrumentation for the design of active control system and their experimental checks;
4. an universal testing machine for material characterization through static and dynamic tests.

The Department of Hydraulics and Environmental Engineering offers:

1. a pressure circuit simulating various movements;
2. a hydrodynamic tunnel studying cavitation problems;
3. micro-channels studying free currents.

Ringraziamenti

Sono molte le persone a cui dovrei rivolgere i miei più cari ringraziamenti per i consigli, il sopporto e i confronti che sono stati alla base di tutte le attività che ho avuto il piacere di svolgere durante il dottorato.

Ringrazio il mio relatore, Stefano Sibilla, per aver condiviso con me parte delle sua smisurata conoscenza e della sua esperienza, per avermi lasciata libera di imparare e di sbagliare, aiutandomi in questo modo a sviluppare la capacità critica, indispensabile per trovare nuove soluzioni.

Un ringraziamento particolare va a Massimo, Sauro e Gabriella per l'appoggio professionale e umano che mi hanno sempre offerto generosamente nonché per l'instancabile e contagiosa passione che infondono nel loro lavoro, un esempio per tutti coloro che muovono i primi passi nel mondo della ricerca.

Ringrazio la mia famiglia, i miei amici, le persone che hanno condiviso con me questo percorso e che hanno creduto in me a volte con più tenacia di quanto non credessi io in me stessa.

Infine ringrazio il CILEA (Centro Interuniversitario Lombardo per l'Elaborazione Automatica) che attraverso il progetto LISA (Laboratorio interdisciplinare per la Simulazione Avanzata) ha contribuito allo svolgimento di una parte delle simulazioni numeriche alla base dell'attività di ricerca.

Elenco delle tesi – Previous PhD Theses

Battaini Marco (X Ciclo)	Sistemi strutturali controllati: progettazione e affidabilità (Novembre 1998).
Mariani Claudia (X Ciclo)	Problemi di ottimizzazione per strutture bidimensionali anisotrope (Novembre 1998).
Negri Antonella (X Ciclo)	Stima delle perdite idrologiche nei bacini di drenaggio urbani (Aprile 1999).
Pisano Aurora Angela (XI Ciclo)	Structural System Identification :Advanced Approaches and Applications (Aprile 1999).
Saltalippi Carla (XI Ciclo)	Preannuncio delle piene in tempo reale nei corsi d'acqua naturali (Aprile 1999).
Barbieri Eugenio (XI Ciclo)	Thermo fluid Dynamics and Topology: Optimization of an Active Thermal Insulation Structure (Aprile 2000).
Barbolini Massimiliano (XII Ciclo)	Dense Snow Avalanches: Computational Models, Hazard Mapping and Related Uncertanties (Aprile 2000).
Espa Paolo (XII Ciclo)	Moti atmosferici generati da forze di galleggiamento: simulazioni numeriche e studio su modello fisico (Aprile 2000).
Petrini Lorenza (XII Ciclo)	Shape Memory Alloys: Modelling the Martensitic Phase Behaviour for Structural Engineering Exploitation (Aprile 2000).

Podestà Stefano (XIII Ciclo)	Risposta sismica di antichi edifici religiosi: una nuova proposta per un modello di vulnerabilità.
Sturla Daniele (XIII Ciclo)	Simulazioni lagrangiane di flussi rapidamente variati nell'approssimazione di acque poco profonde.
Marazzi Francesco (XV Ciclo)	Semi -active Control of Civil Structures: Implementation Aspects (Gennaio 2003).
Nascimbene Roberto (XV Ciclo)	Sail Modelling for Maximal Speed Optimum Design (Gennaio 2003).
Giudici Massimo (XVI Ciclo)	Progettazione in regime non lineare di strutture in CAP a cavi aderenti e non aderenti (Aprile 2004).
Mutti Matteo (XVI Ciclo)	Stability Analysis of Stratified Three-phase Flows in Pipes (Febbraio 2004).
Petaccia Gabriella (XVI Ciclo)	Propagazione di onde a fronte ripido per rottura di sbarramenti in alvei naturali (Febbraio 2004).
D'Amico Tiziana (XVI Ciclo)	Ricerca e sviluppo di metodologie diagnostiche per il recupero di edifici monumentali: prove vibroacustiche sul tufo (Febbraio 2005).
Casciati Sara (XVII Ciclo)	Damage Detection and Localization in the Space of the Observed Variables (Febbraio 2005).
Barco Olga Janet (XVII Ciclo)	Modeling the Quantity and Quality of Storm Water Runoff Using SWMM (Marzo 2006).

Boguniewicz Joanna (XVIII Ciclo)	Integration of Monitoring and Modelling in the Surface Water State Evaluation Process of a Sub-Alpine Lake Watershed (Marzo 2006).
Bornatici Laura (XVIII Ciclo)	L'impiego degli algoritmi generici per la risoluzione dei problemi di progetto di reti di distribuzione idrica (Marzo 2006).
Collivignarelli M Cristina (XVIII Ciclo)	Trattamento di rifiuti liquidi mediante processi biologici aerobici termofili e mesofili e processi avanzati di ossidazione chimica in diversa (Marzo 2006).
Domaneschi Marco (XVIII Ciclo)	Structural Control of Cable-stayed and Suspended Bridges (Febbraio 2006).
Ráduly Botond (XVIII Ciclo)	Artificial Neural Network applications in Urban Water Quality Modeling (MArzo 2006).
Antoci Carla (XVIII Ciclo)	Simulazione numerica dell'interazione fluido-struttura con la tecnica SPH (Luglio 2006).
Cappabianca Federica (XVIII Ciclo)	La valutazione del rischio valanghivo attraverso la modellazione dinamica (Luglio 2006).
Callegari Arianna (XVIII Ciclo)	Applicazione di tecnologie di monitoraggio on-line per la gestione dei processi di trattamento reflui (Luglio 2006).
Gazzola Elisa (XVIII Ciclo)	Applicazione di processi biologici anaerobici al trattamento di acque reflue e fanghi di depurazione: aspetti tecnici ed energetici (Febbraio 2007).

Maranca Federica (XVIII Ciclo)	Valutazione del ciclo di vita (LCA): confronto tra sistemi di trasporto gas via gasdotto (Febbraio 2007).
Giuliano Fabio (XIX Ciclo)	Performance Based Design and Structural Control for Cable Suspension Bridges (Febbraio 2007).
Falappi Stefano (XIX Ciclo)	Simulazioni numeriche di flussi di fluidi viscosi e materiali granulari con la tecnica SPH (Febbraio 2007).
Zanaboni Sabrina (XIX Ciclo)	Pre-trattamento di rifiuti liquidi industriali mediante ossidazione ad umido (Febbraio 2007).
Bruggi Matteo (XX Ciclo)	Topology optimization using mixed finite elements (Febbraio 2008).
Cimellaro Gian Paolo (XX Ciclo)	Passive Control of Industrial Structures for Natural Hazard Mitigation: Analytical Studies and Applications (Febbraio 2008).
Pagliardi Matteo (XX Ciclo)	Application of PIV technique to the study of subaqueous debris flows (Febbraio 2008).
Todeschini Sara (XX Ciclo)	Il controllo degli scarichi fognari in tempo di pioggia mediante vasche di prima pioggia: aspetti progettuali e gestionali (Febbraio 2008).
Alessandro Abbà (XXI Ciclo)	Recupero dei rifiuti speciali nel settore delle costruzioni: studio delle possibilità di recupero e valutazione dei meccanismi di lisciviazione (Febbraio 2009).

Karim Hamdaoui (XXI Ciclo)	Experimental Applications on Cu-based shape Memory Alloys: Retrofitting of Historical Monuments and Base Isolation (Febbraio 2009).
Thomas Messervey (XXI Ciclo)	Integration of Structural Health Monitoring into the Design, Assessment, and Management of Civil Infrastructure (Febbraio 2009).
Filippo Ubertini (XXI Ciclo)	Wind Effects on Bridges: Response, Stability and Control (Febbraio 2009).
Clemente Fuggini (XXII Ciclo)	Using satellites systems for structural monitoring: accuracy, uncertainty and reliability (Febbraio 2010).
Raboni Massimo (XXII Ciclo)	Impiego di tecniche numeriche e sperimentali per l'analisi di fenomeni multiphysics (Luglio 2010).
AlSaleh Raed (XXIII Ciclo)	Verification of wind pressure and wind induced response of a supertall structure using a long term structural health monitoring system (Febbraio 2011).
Crotti Barbara Marianna (XXIII Ciclo)	Verifiche di funzionalità e criteri di ottimizzazione degli impianti di potabilizzazione: alcuni casi di studio (Gennaio 2011).
Franchioli Luigi (XXIII Ciclo)	Analisi prestazionale dei sistemi di distribuzione idrica e calcolo della loro affidabilità (Marzo 2011).

Marzi Alessandro (XXIII Ciclo)	Impianti in materiale plastico per il trasporto dei fluidi nel settore navale (Febbraio 2011).

Index

Introduction

Turbulent jet systems are used to provide mixing and aeration in many fields of chemical, pharmaceutical and environmental engineering. In particular, within wastewater treatment plants, turbulent jet systems are used in the biological oxidation tanks as they enable the simultaneous mixing and oxygenation of the reactor. The issues related to oxygenation of the biological oxidation tank play a crucial role in the management of the system, as dissolved oxygen concentration within the reactor can be a limiting factor for biomass growth, resulting in the simultaneous reduction of the purification performance expectations. Hence, the estimate of an adequate oxygen supply for the degradation of the organic substrate, which is often difficult to be predicted during the design phase, is essential to the proper design of the reactor. To gain this objective, bubble oxygen fed inside the tank must become dissolved oxygen (DO) which is the amount of oxygen really available for substrate removal by active biomass. Hence, the efficiency of the oxygenation process depends largely on the transfer from oxygen bubbles to dissolved oxygen. Moreover, the bubbles are transported inside the tank, so relating the amount of oxygen transferred to the fluid mass also to the hydrodynamics patterns of the fluid flow.

In recent years, besides the traditional methods used for the hydrodynamic verification of the biological process units of treatment plants (e.g. Retention Time Distribution technique) CFD (Computational Fluid Dynamics) tools have confirmed their usefulness, both during the check out and the design stage, in order to identify the optimal operating configurations.

In the first part of the research, a numerical method has been developed with the aim to predict the evolution of the dissolved oxygen concentration by a confined turbulent two-phase jet system (water-oxygen).

A scale model of a bioreactor equipped with a turbulent jet system was used during the experimental stages in support of and as validation tool of the numerical method.

The operating conditions adopted justified the formulation of the hypothesis of a "one-way coupling" numerical model, for which liquid and gas phases are treated separately. In particular, a Eulerian-Lagrangian (E-L) model has been developed: Eulerian for the part concerning the calculation of DO concentration, Lagrangian for the determination of the trajectory of the bubbles injected into the system and of the consequent oxygen transfer.

The DO balance equation was solved through a second order finite difference method for the convective and diffusive terms, while a source term has been considered to model the mass transfer from the gas phase to the liquid phase, considering both the exchange between bubbles and fluid and between the free liquid surface and the atmosphere. Lab tests and numerical simulations considered tap water and pure oxygen.

The liquid flow field and bubble size distribution (BSD) constitute the two main inputs of the numerical model. The flow field was determined by solution of the Navier-Stokes equation by a finite volume method, while BSD was evaluated by applying an optical method for the post-processing of high-resolution images. The validation of the numerical velocity field was made by comparison with velocity measurements made with ADV velocimeter. At a later stage of the research activity, a qualitative analysis of the signal characteristics was conducted by applying two different signal processing methods.

In addition, the numerical model has been completed to include the possibility of simulating the evolution in time of several dissolved species which could be simultaneously present inside the system, starting from the implementation of the heterotrophic biomass growth and of a readily biodegradable substrate consumption kinetics.

In Chapter 1 the main features of a turbulent jet are presented, illustrating the main characteristics and presenting the literature solutions for the circular turbulent free jet and the experimental results for a circular turbulent jet located above a solid wall. This framework will be useful for the characterization of the turbulent jet examined during the research activity.

Chapter 2 deals with the main aspects involved in a two-phase gas-liquid system. Particular attention is given to illustrate the processes related to the diffusion and mass transfer processes between gas and liquid phase. A thorough analysis of the main models proposed in the literature is addressed. Finally, the analysis of the dynamic forces acting on the bubbles is performed, in order to explain the aspects which determine their motion within the surrounding fluid.

A presentation of the processes that take place in an oxidation tank of an activated sludge wastewater treatment plant is carried out inside Chapter 3, focusing on models proposed for the kinetics of biomass growth, substrate removal and consumption of dissolved oxygen.

In Chapter 4 the structure of the E-L model developed is presented, focusing on the theoretical assumptions, on the proposed solution methodology, and on the implemented models considered in order to allow the bubbles motion within the system and to determine the concentration of DO and other dissolved species.

The methodology used for determining the necessary inputs for the E-L numerical model is presented in Chapter 5. The methodology applied for the liquid flow dynamics solution and for the BSD determination is also presented, together with the proposed method for carrying out the velocity measurements used to validate the numerical model, as well as the procedure followed for the post-processing of the acquired velocity signal.

In Chapter 6 is discussed the comparison between the results of the numerical model and experimental values available in literature.

The experimental values of both the velocity and the concentration field of a passive scalar transported by a turbulent jet has been used to verify the correct modelling of the concentration balance equation (for the convective and diffusive terms). Furthermore, the experimental values of Pseudomonas Putida, glucose and BOD concentrations were considered to determine the kinetic constants for biomass, substrate and dissolved oxygen and to evaluate the correct implementation of the related models within the computer code.

Finally, in Chapter 7, the results of the numerical model applied to two different experimental set-up made on the laboratory physical model is presented. The sensitivity analysis on the key variables that influence the outcome of simulations is also discussed.

Chapter 1

Turbulent jets as a solution for mixing and aeration

1.1 Main features of turbulent jets

A complete understanding of the benefits of turbulent jet use requires the definition of their main features and especially of the different ones which occur in all of the configurations that can be adopted.

In fact, several configurations are possible, depending on the needs that have to be satisfied (e.g. downward jet systems, upward jet systems, single or multiple flow exit) on the different nozzle geometries which can be used (e.g. plane, circular, radial jet) and on the different placement within the physical boundaries of the installation environment (e.g. free or confined jets, jets with or without offset from a solid boundary). However, independently from the specific features of each device, they all share the goal of ensuring the mixing of the environment in which they are placed.

For this reason turbulent jets are commonly applied in several industrial applications, especially in pharmaceutical and chemical industry, where the

homogeneity of the dissolved species is fundamental to achieve the expected results of a reaction.

From a more general point of view, the possibility to diffuse into an environment, in such a rapid way, a gas or a fluid flow has guaranteed the wide application of turbulent jet devices in those fields where combustion processes are involved.

Starting from these considerations, another widespread application of jet systems is the possibility to inject a fluid flow which is different from the fluid of the destination environment or which is composed by a mixture of several different phases.

This is the situation of the so called *multiphase jet systems* which are a central subject of this dissertation. Hence, jet systems can be used not only to achieve the mixing of the environment but also to diffuse, at the same time and without using other mechanical devices, substances into it.

This is the reason why turbulent jet systems are widely used in untraditional fields such as potable or wastewater treatment plants. In particular, activated sludge wastewater treatment plants include, as a basic process unity, a biological oxidation tank, where the biomass must deplete the organic load of the incoming sewage (this subject will be analyzed thoroughly in Chapter 3). What we want point out, for the moment, is the power associated with turbulent jet systems which allow (e.g. in the situation just described above) the simultaneous mixing and oxygenation of a compound.

These features are not the only ones that can drive in the selection of a jet system as a solution in certain installations. Turbulent jet systems present the advantage of an easier installation which can lead to lower management costs during the operational life of a system. Besides this, the easy handling of jet systems is the basis of their flexibility and can represent a good reason to choose this solution during emergency events in addition or in place of the traditional mixing/aeration/injection devices.

1.2 Characterization of turbulent jets

As introduced in the last paragraph, several type of turbulent jet geometries can be adopted but, despite of the intrinsic differences that obviously subsist among them, a similar behaviour regarding the flow development downstream of the nozzle exit (or more generally downward the flow exit) can be noticed.

First, it has to be defined what is meant by "turbulent jet" and when a jet can be classified as turbulent.
We have a jet every time a flow exits from an orifice by an abrupt decrease of pressure. This pressure decay causes (for the energy conservation law) a corresponding velocity at the orifice. If the dimensionless number $\mathrm{Re} = U_0 \cdot D/\nu$ (Reynolds number), calculated by multiplying the exit velocity (U_O) by the characteristic dimension of the orifice (generally identified by D) and dividing by the kinematic viscosity of the flow (ν), is greater then the limit of identification of the transitional turbulent flow ($\mathrm{Re} \approx 4000$) a turbulent jet is established.

As mentioned before, the flow development from the orifice is similar for a very large number of jet geometries, in which we can identify two distinct regions. The first one, just downstream the exit of the nozzle, is characterized by a zone of undiminished mean velocity, where the turbulence produced at the boundary of the jet hasn't influenced yet the initial velocity at the nozzle. This region has the typical shape of a cone (or wedge) and is known as the *potential core* or *flow development region*, and it is surrounded by a turbulent shear layer. In the second region, the turbulent shear layer penetrates inside the jet and the maximum velocity at the centreline of the jet decreases moving downstream with a characteristic shape depending by the orifice geometry: this region is known as the *fully developed region*. In this region observations of the mean velocity reveal that the distribution of the velocity profile at a certain distance from the nozzle exit obeys a similarity law.

Similarity means that, when same reference non-dimensional velocities and lengths scale, are employed to represent the behaviour of the velocity profile of the jet at different distances from the nozzle all the plots collapse on the same curve.

In general, the velocity scale is derived by dividing the local mean velocity (u) by the local maximum mean velocity (u_m), while the length scale is obtained by dividing the local transversal coordinate by the coordinate (b) where the local mean velocity is equal to $u_m/2$.

Another relevant aspect regarding turbulent jets is represented by the fact that the jet during its development increases its discharge when compared to the initial one, owing to the entrainment of fluid from the external environment: this property is known as the entrainment hypothesis.

Moreover, when one deals with turbulent jets it is convenient to identify the so-called virtual origin, which is the jet fictitious origin, from which the axial distance from the nozzle is measured to describe the hydrodynamic behaviour of the jet. The location of this origin depends from the typical shape of the diffusing jet. In fact, moving further downstream the jet usually increases its transversal dimension approximately linearly and the envelope containing the turbulent shear layer due to the jet is generally encompassed by a cone (or wedge) shaped region, whose vertex can fall downstream or upstream the plane of orifice. Therefore, the virtual origin and the actual one may not coincide. This displacement is mainly due to the level of turbulence at the nozzle, while it seems to be more or less insensitive to the nozzle geometry (Rajaratnam, 1976). A graphical representation of the location of the virtual origin of a turbulent circular free jet is shown in Figure 1.1.

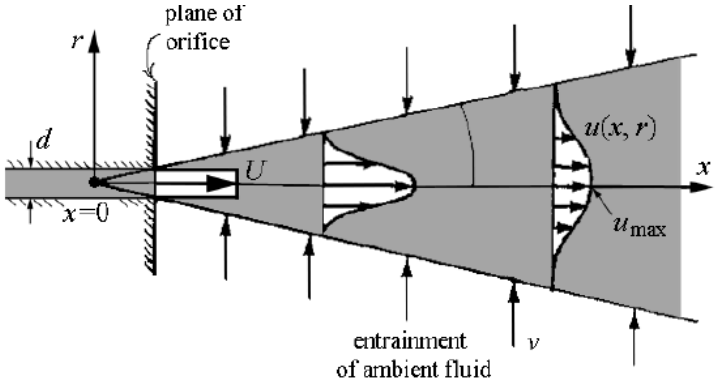

Figure 1.1 Identification of the virtual origin (x=0)

A description of the turbulent jet behaviour can be achieved either by studying experimentally the velocity field induced by the jet or by regarding the equations of motion and trying to solve them analytically, imposing the necessary closure equations. Actually the theory describing a turbulent jet usually refers to both of these two approaches because the analytical solution generally needs the definition of a high number of constants. In particular, depending on the adopted closure model for turbulence shear stresses, we can identify two main classical solutions. The Prandtl mixing length formula to estimate turbulent shear stresses leads to the Tollmien solution, while the choice of the second equation of Prandtl (or eddy-viscosity model) leads to the Goertler solution instead. We will analyse in detail these solutions in paragraph 1.2.1.1 and 1.2.1.2.

1.2.1 Circular turbulent free jet

When a momentum flux originated from a circular nozzle discharges into a large quiescent ambient of the same fluid (with no interactions with any type of boundary), we have a turbulent circular free jet. If the velocity at the nozzle exit is U_0, we can represent the turbulent jet behaviour as shown in Figure 1.2.

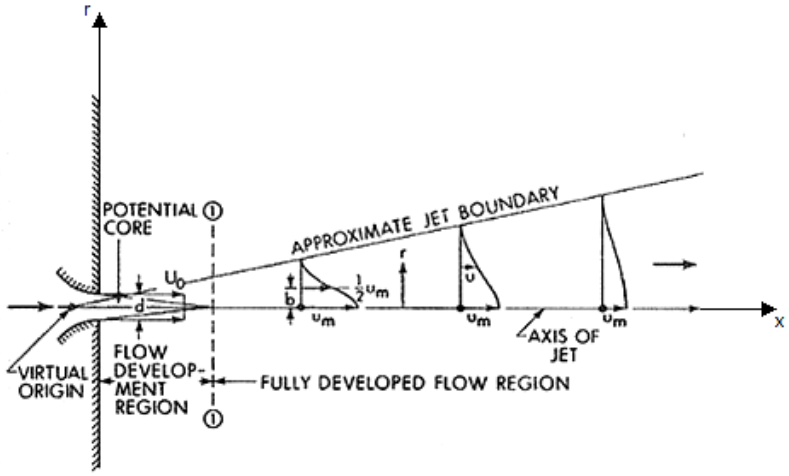

Figure 1.2 Scheme of the turbulent free jet behaviour

We can observe that, in the fully developed region, the maximum velocity along the jet axis (u_m) decreases when moving downstream (x direction). The transversal velocity distributions at different locations from the nozzle show the self-similarity property of the turbulent jet: considering the velocity and the length scale (respectively u/u_m and $\eta=r/b$) each experimental velocity profile of Figure 1.3(a) collapses in the same curve depicted in Figure 1.3(b).

So, given the velocity and length scales and the axial evolution of the maximum time-averaged velocity with respect to the initial value U_0, it is possible to derive the time-averaged velocity at any point inside the fully developed turbulent region of the jet.

To do this, we must consider the equations of motion for a steady axisymmetric flow of an incompressible fluid in the cylindrical coordinate system (r, ϕ, z). First of all, we can consider that, when no swirl is imposed at the nozzle exit, the velocity component in the angular direction ϕ is zero ($v_\phi = 0$) as well as any of its derivatives.

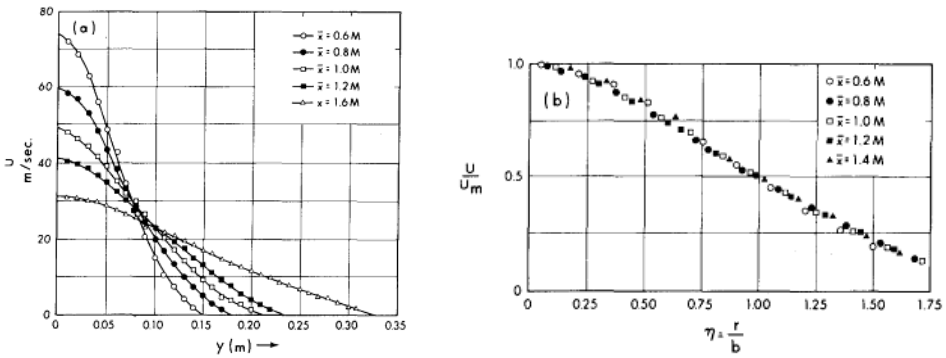

Figure 1.3 Radial velocity profile at different x positions (a) and dimensionless radial velocity profile (b)

Moreover, the velocity component v_z is in general much larger than the mean radial velocity, while the velocity gradients in the radial direction are larger than those in the axial direction. Finally, viscous stresses can be neglected and we can consider only the contribution of turbulent stresses. After some mathematical simplifications and considering zero pressure gradients in the axial direction, we can derive the equations of motion for the circular turbulent jet (now being x the axial coordinate):

$$u\frac{\partial u}{\partial x}+v\frac{\partial u}{\partial r}=\frac{1}{\rho}\frac{1}{r}\frac{\partial r\tau}{\partial r} \tag{1.2.1}$$

$$\frac{\partial}{\partial x}ru+\frac{\partial}{\partial r}rv=0 \tag{1.2.2}$$

where, u and v are the velocity component in axial and radial direction respectively, ρ is the fluid density and $\tau=\left\langle u'v'\right\rangle$ is the only relevant component of the turbulent stress tensor.

The equations for the velocity and length scales can be obtained by regarding the problem from a different point of view.

First we have to consider that, since no other accelerating or decelerating forces are involved, the momentum flux in the axial direction is preserved. Integrating equation (1.2.1) from $r = 0$ to $r = \infty$, being $\tau(r = 0) = \tau(r = \infty)$ and $v(r = 0) = v(r = \infty) = 0$, we obtain:

$$\frac{\partial}{\partial x}\int_0^\infty 2\pi\rho u^2 r dr = 0 \tag{1.2.3}$$

We assume that the velocity scale can be written as a function of the length scale:

$$\frac{u}{u_m} = f(r/b) = f(\eta) \tag{1.2.4}$$

Moreover, let:

$$u_m \propto x^p \tag{1.2.5}$$

$$b \propto x^q \tag{1.2.6}$$

Substituting equation (1.2.4) in equation (1.2.3) and changing the integration variable from r to η, we obtain:

$$\frac{d}{dx}\rho u_m^2 b^2 \int_0^\infty 2\pi\eta f(\eta)^2 d\eta = 0 \tag{1.2.7}$$

Since the integral in equation (1.2.7) is constant, the product $u_m^2 b^2$ can be written as Cx^0 with C being a suitable constant. Taking into account equations (1.2.5) and (1.2.6) we obtain:

$$2p + 2q = 0 \text{ or } p + q = 0 \tag{1.2.8}$$

The evaluation of the exponents p and q can be performed by considering several methods. To limit the mathematical steps needed to derive their value, we consider the entrainment hypothesis, from which we can write the flow rate Q at any x section from the nozzle as:

$$Q = \int_0^\infty 2\pi u r dr \tag{1.2.9}$$

and its derivative in the axial direction, as:

$$\frac{dQ}{dx} = \frac{d}{dx}\int_0^\infty 2\pi u r dr = 2\pi \bar{b} v_e \tag{1.2.10}$$

where v_e is the entrainment velocity (i.e. the radial velocity necessary to entrain the quiescent fluid inside the jet region; see Figure 1.1), and $\bar{b}$ is a length scale corresponding to the position of nearly zero velocity (outer boundary of the jet). Consistently with equations (1.2.5) and (1.2.6) we can assume the proportionality:

$$v_e = \alpha_e u_m \propto x^p \tag{1.2.11}$$

$$\bar{b} \propto x^q \tag{1.2.12}$$

The same transformation adopted to obtain equation (1.2.7) can be repeated to yield:

$$\frac{d}{dx}\left(u_m b^2\right)\Big/\bar{b}\, v_e \propto x^0 \tag{1.2.13}$$

Considering the exponents involved in equation (1.2.13) we obtain:

$$p + 2q - 1 - q - p = 0 \tag{1.2.14}$$

And finally q = 1, so and from equation (1.2.8) p = -1, or considering equation (1.2.5) and (1.2.6):

$$u_m \propto 1/x \tag{1.2.15}$$
$$b \propto x \tag{1.2.16}$$

This means that the behaviour of the local maximum time-averaged velocity of a turbulent circular free jet is inversely proportional to the displacement in the axial direction *x*, while the jet width increases linearly in *x*.

In this way, we have just defined the spatial evolution of the velocity and length scales but not yet the velocity distribution at a given transversal section of the jet. As mentioned earlier (paragraph 1.2) the description of the velocity distribution needs a closure equation for the turbulent stresses.

1.2.1.1 Tollmien solution

The closure equation adopted by Tollmien (1926) is based on the Prandtl's mixing length theory for the turbulent shear stress, τ:

$$\tau = -\rho l^2 (\partial u/\partial r)^2 \tag{1.2.17}$$

where l is the mixing length, considered to be proportional to the length scale b, that we know from equation (1.2.16) to be proportional to x:

$$l \propto b = Cx \tag{1.2.18}$$

where C is a suitable constant, from which it can be imposed $C^2=a^3$, where a is another constant which has to be determined experimentally.

Considering equations (1.2.4) and (1.2.16), we can impose:

$$\frac{u}{u_m} = f_2\left(\frac{r}{b}\right) = f(\phi) \text{ being:}$$
$$\phi = \frac{r}{ax} \tag{1.2.19}$$

Introducing the Stokes function, ψ:

$$ru = \frac{\partial \psi}{\partial r} \text{ and } rv = -\frac{\partial \psi}{\partial r} \tag{1.2.20}$$

and combining the first relation of equation (1.2.20) with equation (1.2.19), we get:

$$\psi = u_m a^2 x^2 F(\phi) \text{ with:} \tag{1.2.21}$$
$$F(\phi) = \int_0^{\phi} \phi f(\phi) d\phi$$

Combining equation (1.2.21) with equation (1.2.20) and rewriting equation (1.2.17) introducing $F(\phi)=F$, the equation of motion (1.2.1) assumes the form:

$$\left(F'' - \frac{1}{\phi} F'\right)^2 = FF' \tag{1.2.22}$$

Tollmien solved equation (1.2.22) and got the behaviour of u/u_m (which is equal to $F'(\phi)/\phi$) and v/u_m respect to the variation of ϕ.
Considering the equation of the momentum flux (integral into equation (1.2.3)) and observing that for Tollmien solution $b = 1.24ax$, it's possible to derive the local maximum velocity at any x section by the equation:

$$\frac{u_m}{U_0} = \frac{0.965 r_0}{a x_0} \tag{1.2.23}$$

where U_0 and r_0 are the velocity at the nozzle exit and the nozzle radius respectively.
From several experimental observations (Abramovich, 1963) the value of a seems to increase from a value of 0.066 to a value of 0.076 increasing the ratio between the mean and the maximum velocity at the nozzle and with the level of turbulence of the jet.

1.2.1.2 Goertler-type solution

The closure equation adopted by Goertler (1942) to obtain the theoretical form of the velocity distribution was the eddy-viscosity model (or Prandtl's second equation) for the turbulent shear stress, τ:

$$\tau = \rho \varepsilon (\partial u / \partial r) \tag{1.2.24}$$

where ε is the kinematic eddy viscosity, which is considered to be proportional to u_m and b by an unknown constant k. In a similar way to that adopted by Tollmien, defining:

$$\frac{u}{u_m} = f(\xi) \text{ being: } \xi = \frac{\sigma r}{x} \tag{1.2.25}$$

where σ is a constant which has to be determined experimentally. Using now the Stokes stream function defined as:

$$\psi = \frac{u_m x^2}{\sigma^2} F(\xi) \quad \text{with:}$$
$$F(\xi) = \int_0^{\xi} \xi f(\xi) d\xi \tag{1.2.26}$$

Coupling equation (1.2.26) with equation (1.2.2) and equation (1.2.24), the equation of motion takes the form:

$$F' - \xi F'' = FF' \tag{1.2.27}$$

By imposing the necessary boundary conditions Goertler obtained the solution for the equation (1.2.27) and, finally the behaviour of u/u_m and v/u_m varying the independent variable ξ. Looking at the Goertler solution we noticed that $b = 1.81 \cdot x/\sigma$. Regarding the integral momentum equation (integral into equation (1.2.3)) after some simplifications we get:

$$\frac{u_m}{U_0} = \frac{\sigma r_0}{1.61 x_0} \tag{1.2.28}$$

From Reichardt experimental observations (Reichardt, 1942) we can assume a value of σ equal to 18.5.

The comparison between Tollmien, Goertler-type solution and the experimental observations of Reichardt are shown in Figure 1.4.

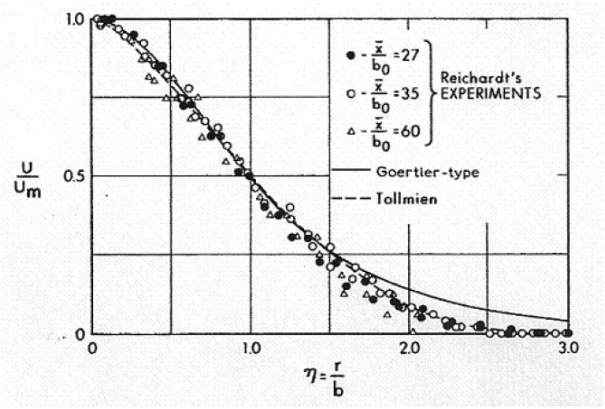

Figure 1.4 Comparison between Tollmien, Goertler-type solution and experimental observations of Reichardt

Looking at Figure 1.4 it can be noticed how Goertler-type solution seems to fit the experimental data of Reichardt near the jet axis more closely than the Tolmien solution; on the other hand, Tollmien solution agrees well with experiments for larger values of η. Some other experimental works suggest analytical interpretation of the velocity distribution, and some of them (e.g. Hinze and Zinjnen, 1949; Abramovich, 1963; Albertson et al., 1950) detected a location of the virtual origin different from the nozzle exit. However, owing to the uncertainty to define the exact location, the virtual origin and the actual one can be considered coincident.

1.2.2 Circular turbulent jet above a plane wall

It frequently occurs, inside several industrial applications, to have turbulent jets positioned at a distance from a solid wall that does not allow their schematization as free turbulent jets. Actually, this occurs whenever the solid interacts with the development of the turbulent jet by changing the diffusion behaviour and the velocity decay downstream of the nozzle exit. This situation has been experimentally studied with interest by many authors (e.g. Davis and

Winarto, 1980; Newman et al., 1972) who tried to understand the effect of the plane wall on the flow structure.

In particular, Davis and Winarto (1980) focused their efforts on the role played by the distance of the centre of the nozzle from the solid wall (*h*). For instance, they studied four different cases characterized by a ratio *h/D* (with *D* diameter of the nozzle) varying from 0.5 to 4. The general representation of the flow behaviour is shown in Figure 1.5, where the separation between the corresponding regions of development flow for the turbulent free jet can be noticed. The first interaction with the plane takes place in the initial zone for a clearance (*h/D*) smaller than 1.2, whereas the interaction-point will move downward for a greater value of the defined ratio; in particular, for *h/D* between 1.2 and 2.6 the interaction will be in the transition region while for *h/D* greater than 2.6 it will lay in the zone of fully free jet.

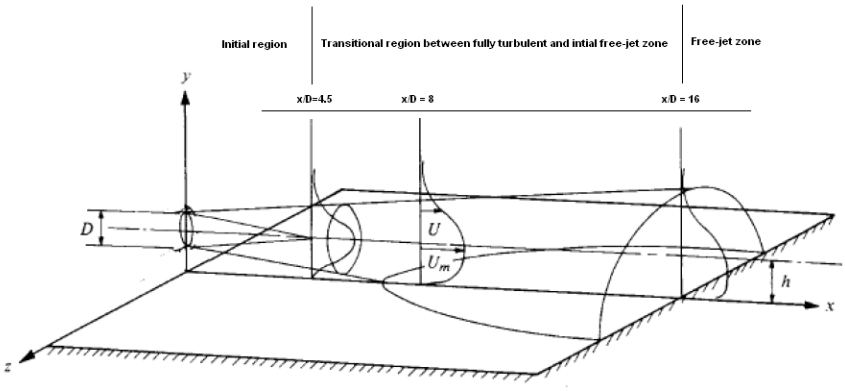

Figure 1.5 General representation of flow behaviour (for h/D = 1) (Davis and Winarto, 1980)

Their observations of the velocity field show that the rapid sidewall diffusion involves at first the outer region of the mixing flow and that the shape of the jet looks increasingly pressed toward the plane, at a given *x/D* position, when the value of *h/D* is reduced. Furthermore, the transitional process from a free jet to a three-dimensional wall jet seems very long-lasting, due to the fact that the jet has to change its shape from circular to elongated, even if the delay is lower for the larger value of *h/D*. Moreover, the decay of the maximum velocity along the

direction aligned with the nozzle axis is modified by the presence of the wall: in fact, at a given *x/D* position, the maximum velocity increases if compared with the corresponding value in a free jet. It also can be noticed that the virtual origin of the jet moves downward as *h/*D increases.

Nevertheless, the spatial rate of decay of the radial velocity seems not so different from the behaviour of a free jet, both for the rate of the velocity decay perpendicular to the plane and for the behaviour of u/u_m parallel to the wall, as depicted in Figure 1.6 and Figure 1.7 respectively, where experimental results are compared with the Goertler-type solution for a free jet (dashed line) and with an exponential profile describing the turbulent free jet behaviour (solid line). Looking at Figure 1.6 it can be noticed how near the solid wall ($\eta < 0$) the local maximum velocity seems greater than the free jet velocity at *x/D* = 32 (square symbol) that corresponds to the position of first interaction with the wall. Instead, it seems that the local velocity remains smaller than the free jet in the outer region for each position *x/D*. From Figure 1.7 it can be noticed that the configuration characterized by the smallest value of clearance seems to overcome the dimensionless velocity profile of a free jet in the outer region and to have a lower value close to the jet axis.

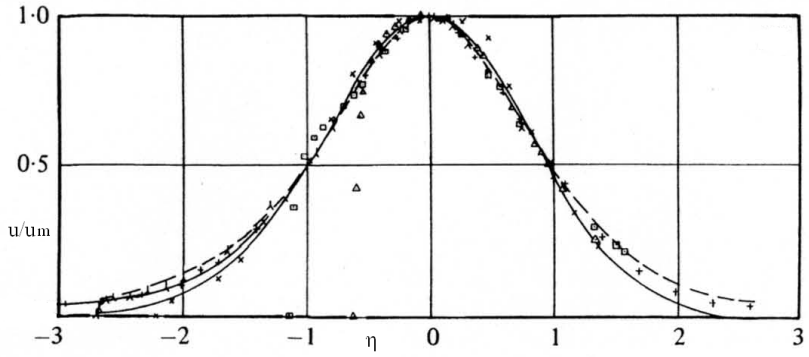

Figure 1.6 Dimensionless velocity profile perpendicular to the plane wall ($\eta = (y - y_m)/(b-y_m)$) for *h/D* = 4. Lines: circular turbulent free jet solutions; Experiments: ×, *x/D* =4.5;+, *x/D* =8;λ, *x/D* =16;□, *x/D* = 32;○, *x/D* =48; ∆, *x/D* =64

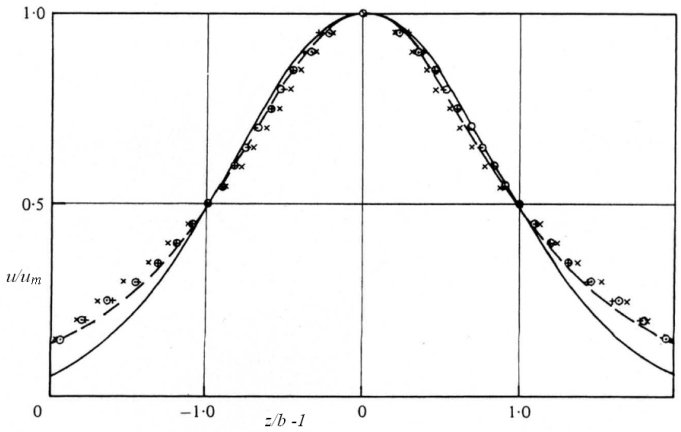

Figure 1.7 Dimensionless velocity profile parallel to the plane wall. Lines: circular turbulent free jet solutions; Experiments: +, *h/D* =4; ○, *h/D* =1; ×, *h/D* =0.5

Finally, it can be seen that the location of the point of maximum velocity above the surface in the vertical plane passing through the centre of the jet nozzle, tends to be displaced from the nozzle axis towards the wall, until the jet merges with the wall boundary layer (Figure 1.8). This merging occurs close to the nozzle for low values of *h/D* and moves downstream from higher *h/D*.

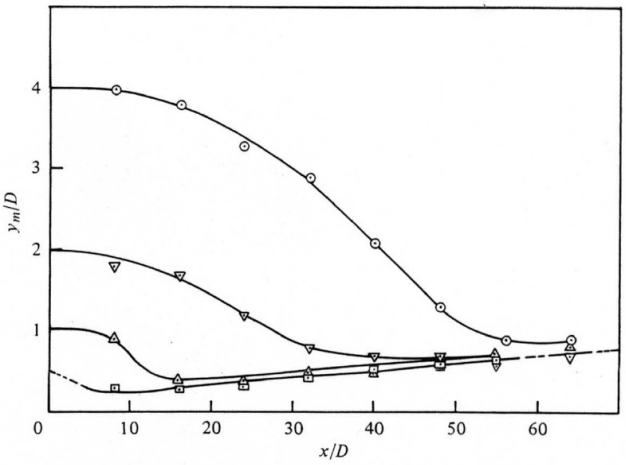

Figure 1.8 Location of the maximum velocity position above the solid wall. □, h/*D* = 0.5; ∆, h/*D* =1; ▽, h/D= 2; ○, *h/D* =4

Chapter 2

Two phase liquid-gas systems

2.1 Dissolution, diffusion and mass transfer of gas species in water

As observed inside Chapter 1, the dissolution of gases in liquids is the basis of many operations in the field of chemical and environmental engineering. In order to properly evaluate and model diffusion phenomena, it is essential to understand the issues related to the dynamics of dissolution and diffusion processes, highlighting the factors that may influence their evolution, the equations describing the processes and the models proposed for their schematization.

In the following pages, the explanation of dissolution and diffusion mechanism is presented first. Then, the theory of mass transfer is discussed through an overview of the models available in literature.

2.1.1 Solubility of gases in water

In several chemical and environmental engineering fields it is quite common to deal with gaseous species dissolved in a liquid environment. In many applications a certain concentration of dissolved gases is needed to maintain the efficiency of the process. In this case, the dissolved gas can be supplied with some aeration device as a bubbly phase inside another fluid phase. But what does it mean dissolved and how can a gas bubble become dissolved?

The answers at these questions need the introduction to some basic chemical notions, concerning with phase equilibrium.

If we observe the dissolved gaseous concentration of a certain species which is present in water also in a bubbly phase, its variation during the observation time will depend on the coexistence of different processes. The gas passes through the bubble surface into the bulk solution, then dissolves, diffuses, disperses and might move inside the liquid volume. The final concentration that can be reached by the dissolving species is related to all these aspects. It is quite well know that there is an upper limit for the amount of gas that can be dissolved into the liquid phase. This limit depends both on the nature of the involved fluid and on the environmental characteristics, such as temperature and salinity.

The concentration limit is determined by Henry's law, which states a linear proportionality between the maximum concentration (saturation concentration, c_{sat} (mg/l)) and the partial pressure of the gas (p_g (Pa)) by means of Henry's constant (k_H (mg/lPa^{-1})):

$$c_{sat} = k_H p_g \tag{2.1.1}$$

The partial pressure is therefore the first factor which can affect the saturation value achieved by the dissolved species. This is the reason why inside every natural water reservoir, for example, the dissolved oxygen concentration cannot overcome a certain value (typically 10 mg/l, more or less), even if the saturation concentration for pure oxygen can lead at a maximum concentration

which can be of almost 5 times greater. Actually, this occurs because the partial pressure of oxygen in atmosphere is around 21% of the atmospheric pressure. This aspect is also quite important in aeration systems. Using pure gas instead of a gas mixture influences greatly the efficiency of the system, especially for certain chemical applications where the concentration of a dissolved species could represent a key factor to ensure some rate of reaction or to achieve the production of a specific compound.

As mentioned above, there are two other factors, apart from pressure, that can affect the value of the Henry's constant: salinity and temperature. For both of them a relation of inverse proportionality subsists between their value and the corresponding Henry's constant value. Hence, an increase of salinity or/and temperature leads to a lower value of the constant. The relation between Henry's constant and temperature is expressed by an Arrhenius-type relation (Sander, 1999):

$$k_H = k_H^* \exp\left(-\frac{\Delta H_{sol}}{R}\left(\frac{1}{T}-\frac{1}{T^*}\right)\right) \tag{2.1.2}$$

where:

ΔH_{sol} is the enthalpy of the solution (J);

R is the gas constant (J/K);

T is the temperature (K).

while the superscript * identifies the standard condition of reference (T^* = 298.15 K). Many authors investigated the appropriate value of the ratio between enthalpy and gas constant associated with the reference value of the Henry's constant as given inside relation (2.1.2) (Loomis, 1928; Carpenter, 1966; Wilhelm et al., 1977; Lide and Frederikse, 1995). An appropriate value of the mentioned ratio for gaseous oxygen seems to be 1700 K, while a value of 0.0013 M/atm is suggested for k^*_H.

So, if we consider a vessel filled with water where an oxygen injection takes place, the saturation concentration of dissolved oxygen in water is usually

defined as the maximum concentration that can be reached by the dissolution of the atmospheric oxygen. However, this is not the maximum value that can be reached at all. If we supply the water with pure oxygen the dissolved oxygen concentration may overcome the saturation concentration referred to the partial pressure of oxygen in water. In this situation the water is called over-saturated (with respect to the saturation concentration calculated considering atmospheric oxygen).

Finally, we can notice that gaseous oxygen doesn't react with water, but it acts like an oxidizer, leading to the oxidation of the organic matter.

2.1.2 Diffusion and mass transfer processes

Diffusion is the process by which the concentration of a certain species into another tends to uniformity, through a flux which occurs from the higher concentration zones to the lower ones, owing to molecular motion. For sake of truth, the just mentioned process must be referred as molecular diffusion process; another kind of diffusion, which leads to the same final result (i.e. the complete mixing of the environment) can occur when the environment is mixed by mechanical devices or by turbulence effects. What distinguishes the former diffusion process from the latter is the characteristic time of the process, i.e. the time needed to achieve the complete mixing. Molecular diffusion processes are very slow if compared with diffusion owed by stirring or turbulence; moreover, the rate of diffusion is strongly related to the state of the matter of the particles we are considering. Molecular diffusion processes are fast for gases if compared with diffusion inside liquids and tremendously fast if compared with diffusion inside solids.

But what we are interested in is how the diffusion processes are mathematically described and how we can define the diffusive mass flux from a zone to another.

The first scientist who studied the diffusion processes was Thomas Graham in the middle of nineteen century, but the most important contribute to the understanding of the diffusion processes must be ascribed to Fick (1855), who

verified his own postulate by means of experiments. He understood that the diffusion processes could be interpreted in a way analogous to heat (Fourier's law) and electrical conduction (Ohm's law). He argued that in steady state conditions the total mass flow rate (J_i) of the species under consideration across the diffusion area (A) depends on the concentration gradient in the transfer directions $(\partial c/\partial s)$ and that this dependence is of direct proportionality by means of a constant (diffusion coefficient, D):

$$J_1 = j_1 A = -AD\frac{\partial c_1}{\partial s} \tag{2.1.3}$$

or in general form, in a cartesian coordinate system:

$$J_1 = j_1 A = -AD\nabla c_1$$
$$\text{where: } \nabla c_1 = \frac{\partial c_1}{\partial x} + \frac{\partial c_1}{\partial y} + \frac{\partial c_1}{\partial z}$$

Equation (2.1.3) is known as the first Fick's law. From a dimensional analysis, if we consider that the concentration is expressed as [M/L³], the area as [L²] and that the total mass flow rate is expressed as [M/T], it can be immediately deduced that the diffusion coefficient has the units of a squared length by time [L²/T].

The first Fick's law can be considered as a simplified format of the second Fick's law, developed for systems in unsteady state conditions as claimed in equation (2.1.4), from which the equation (2.1.3) can be derived when the time derivative is equal to zero:

$$\frac{\partial c_1}{\partial t} = D \cdot \nabla^2 c_1 \tag{2.1.4}$$

$$\text{where: } \nabla^2 c_1 = \frac{\partial^2 c_1}{\partial x^2} + \frac{\partial^2 c_1}{\partial y^2} + \frac{\partial^2 c_1}{\partial z^2}$$

As mentioned above, the diffusion coefficient can be both considered as a molecular diffusion coefficient (D_m) or as the sum of a molecular diffusion and a mechanical/turbulent diffusion coefficient (E_t), depending on the flow patterns characterizing the environment.

Focusing our attention on the molecular diffusion coefficient in a liquid, it can be seen how its value is correlated with the diffusion coefficient derived by the Stokes-Einstein's law:

$$D = \frac{kT}{6\pi\mu r_p} \tag{2.1.5}$$

where:

k = Boltzman's constant ($1.3805 \cdot 10^{-23}$ J/K);

T = temperature (K);

μ = dynamic viscosity of the diffusion medium (Pa·s);

r_p = particle radius (m);

Derived by the Stokes-Einstein's law is the relation proposed by Wilke and Chang (1955), which for the diffusion coefficient of oxygen in water takes the form:

$$D = 7.4\times10^{-8}\,\frac{T(\psi_{H20}M_{H20})^{\frac{1}{2}}}{\mu V_{O2}^{0.6}} \tag{2.1.6}$$

where:

T = absolute temperature (K);

ψ = association parameter for the solvent water = 2.26 (Reid et al., 1977);

M_{H20} = molecular weight of water = 18 g/mole;
μ = dynamic viscosity of water (centiPoise);
V_{O2} = molar volume of oxygen = 25.6 cm³/(g·mole) (Welty et al., 1984).

If we consider the diffusion process across a thin layer of a certain species 1 that diffuses from a well mixed volume to another well mixed volume of the same phase (Figure 2.1) in steady state conditions (i.e. no mass accumulation into the layer subsists) the diffusion flux and the concentration profile into the layer can be predicted, by means of equation (2.1.7) with the proper boundary conditions.

$$j_1 = -D\frac{\Delta c}{\Delta z} \tag{2.1.7}$$

It can be noticed that the diffusive flux depends on the difference between the concentration inside the two environment ($\Delta c = c_{10} - c_{il}$), divided by the thickness of the layer (Δz), and that the concentration profile into the layer is linear in z direction.

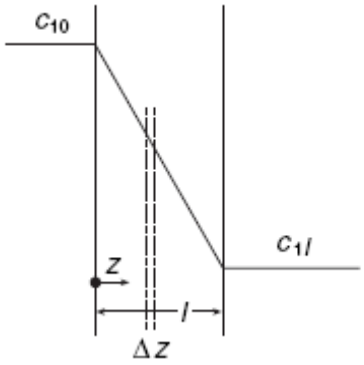

Figure 2.1 Diffusion of the species 1 across a thin layer in steady state conditions

Unfortunately, this type of process does not occur so frequently in practical applications, where the real geometry is generally more complex and therefore analytical solutions are more difficult, and often impossible, to derive. Let us

consider, for example, that the thickness of the diffusing layer is no small and uniform and that the diffusion coefficient is not a constant during the process but is influenced by the change in concentration in the environment we are considering and that the diffusion layer represents an interconnection-discontinuous layer between two different phases (typical of absorption processes of a gaseous species into a liquid).

In this case, an equivalent way to deal with diffusion processes, developed from a more engineering point of view is the mass transfer approach.

In the mass transfer theory the specific diffusive flux of species 1 (j_1) depends only from the difference in concentration (Δc) we are considering by means of a mass transfer coefficient (k):

$$j_1 = k\Delta c \tag{2.1.8}$$

or in terms of total diffusive flow rate (the same as relation (2.1.3)):

$$J_1 = kA\Delta c \tag{2.1.9}$$

The mass transfer coefficient is dimensionally a velocity and for this reason is sometimes referred to the "velocity of diffusion".

What we want to point out here are the main models developed to deal with problems where a mass transfer across a phase boundary occurs. The problems of absorption of gaseous species in a liquid and the gas volatilization or stripping can be ascribed to this case study, for example. For both of these processes, because no material accumulates at the interface, the rate of transfer on each side of the layer must be the same, and so the concentration gradients automatically adjust themselves so that they are proportional to the resistance to transfer in the particular phase. Moreover, it is often possible to consider that the concentrations on each side are related to each other by the phase equilibrium relationship.

The main factors that affect the mass transfer are the physical properties of the involved phases, the concentration difference, the interfacial area (A, inside equation (2.1.9)) and the degree of turbulence.

Several models have been developed to describe the mass transfer phenomena in the region of a phase boundary. They are a good starting point but some difficulties to their application still exists.

2.1.2.1 Two-film theory

The two-film theory suggested by Whitman (1923) supposes that the resistance offered to the mass transfer across the interface is mainly due to the presence of thin layers located at each side of the phase boundary. The fluid inside these regions is considered laminar, even if outside the layers turbulent eddies can accelerate the action of the random movement of molecules and the resistance to mass transfer progressively diminishes. A schematic drawing of the interface layer considered by theory is shown in Figure 2.2.

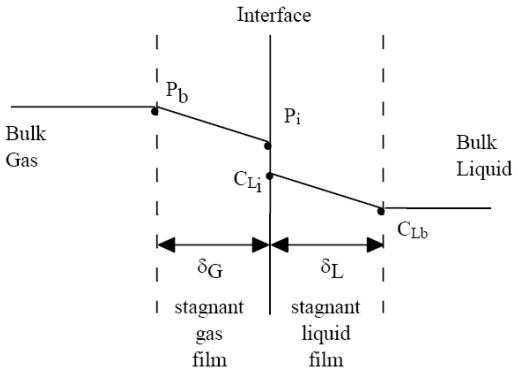

Figure 2.2 Two-film theory scheme

If no accumulation at the interface subsists, the rate of transfer in the gaseous film and in the liquid film must be equal. For this reason we can write:

$$j_1 = k_g(p_b - p_i) = k_L(c_{Li} - c_{Lb}) \tag{2.1.10}$$

where:

j_1 = mass transfer flux of species 1;
p_b = partial pressure of species 1 into the bulk gas;
p_i = partial pressure of species 1 at the interface in equilibrium with the concentration of species 1 into the bulk liquid;
c_{li} = concentration of species 1 at the liquid interface in equilibrium with the partial pressure of species 1 in the gas;
c_{lb} = concentration of species 1 in the bulk liquid;
k_g = mass transfer coefficient through the gaseous film;
k_L = mass transfer coefficient through the liquid film.

The evaluation of the local values of the mass transfer coefficient at the interface is not of easy determination, so it is usually preferred to deal with global mass transfer coefficient (K_G and K_L). For slightly soluble gases (as O_2 or N_2) the mass transfer is controlled by the resistance offered by the liquid film. The reason must be found on the fact that very small concentration differences can be established across the liquid film. The solute diffuses so slowly through the liquid film that only a small concentration difference is therefore required across the gas film. Consequently the liquid at the interface is substantially saturated with solute at the partial pressure of the bulk gas (p_b) and it is pointless to consider the gas film in the calculations. So, we can rewrite equation (2.1.10) in the form:

$$j_1 = K_L(c_{Ls} - c_{Lb}) \tag{2.1.11}$$

where, c_{LS} is the concentration of species 1 into the liquid at the equilibrium with partial pressure of the bulk gas, which can be easily determined applying Henry's law (relation (2.1.1)).

The fact that the rate of diffusion depends mainly on the liquid film highlights the importance of the thickness of the liquid film in the prediction of

diffusive rate as claimed by relation (2.1.7). For this reason, two-film theory is often summarized as:

$$K_L \approx D/l \tag{2.1.12}$$

where D is the diffusion constant and l is the liquid film thickness.

Therefore any operation which can lead to the reduction of the thickness of the layer is well accepted during absorption processes. In particular, the increase of the level of turbulence inside the bulk liquid gives rise to a progressive decrease of the film thickness.

Another interesting point of view is offered by the definition of the volumetric mass transfer rate, which, considering equation (2.1.11) can be expressed as:

$$j_1 \frac{A}{W} = K_L \frac{A}{W}(c_{Ls} - c_{Lb}) = K_L a(c_{Ls} - c_{Lb}) \tag{2.1.13}$$

where A, represents the area through which the mass transfer takes place and W is the liquid volume involved by the increase of concentration; therefore a, is a specific area used to represent the mass transfer process.

The coefficient $K_l a$ is known as the *overall mass transfer coefficient* and is one of the most important parameter in the global evaluation of absorption processes: its measure is used to define the efficiency of absorption devices.

2.1.2.2 Penetration theory

The penetration theory is maybe the most widely applied theory developed for the treatment of problems of mass transfer across a phase boundary. It was developed by Higbie (1935) who suggested that, differently from what supposed in the two-film theory, the transfer process could be mainly due to fresh fluid being brought close to the interface by action of convection

processes (either due to buoyancy or turbulence). At the interface a process of unsteady transfer would then take place for a fixed period at the freshly exposed surface. The theory was developed to describe absorption processes from a pure gas in a liquid and was developed by observing the dissolution processes of a carbon dioxide bubble rising in a tube filled with quiescent water. The exposure time of each element of volume in the liquid to the gas bubble was estimated as the time required to the bubble to pass through the liquid, hence evaluated as the ratio of the bubble diameter to the bubble rise velocity. It was further supposed that during this short period absorption took place as the result of unsteady molecular diffusion into the liquid and, to simplify calculations, the liquid was regarded as infinite in depth because of the short ttime of exposure. A schematic representation of the absorption process in Higbie's theory is given in Figure 2.3.

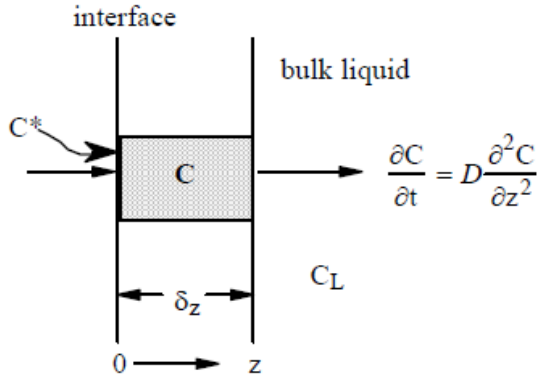

Figure 2.3 Penetration theory scheme

The expression of the mass transfer coefficient in Higbie's theory was derived solving the unsteady diffusion equation (second Fick's law) which can be rewritten as:

$$\frac{\partial c}{\partial t} = D\frac{\partial^2 c}{\partial z^2} \tag{2.1.14}$$

Actually, after imposing the necessary initial and boundary conditions:

$$\begin{aligned} &t=0: \quad 0<z<\delta z \quad && c=c_L \\ &t>0: \quad z=0 && c=c^* \\ &\qquad\; z=\delta z && c=c_L \end{aligned} \tag{2.1.15}$$

the analytical solution of equation (2.1.14) is possible considering that:

$$\frac{\partial c'}{\Delta t} = D\frac{\partial^2 c}{\partial z^2} \tag{2.1.16}$$

where $c' = c - c_L$. Introducing the Laplace transform of the concentration increment c':

$$L\{c'\} = \int_{\infty}^{0} c' e^{-st}\, dt = \overline{c'} \tag{2.1.17}$$

we can rewrite equation (2.1.16) as:

$$s\overline{c'} = D\frac{\partial^2 \overline{c'}}{\partial z^2} \tag{2.1.18}$$

The solution to equation (2.1.18) is:

$$\overline{c'} = B_1 e^{z\sqrt{s/D}} + B_2 e^{-z\sqrt{s/D}} \tag{2.1.19}$$

which, after enforcement of the boundary conditions and after some mathematical manipulations yields the mass transfer flux, j, at any position z at time t:

$$(j)_t = -D\frac{\partial c}{\partial z} = (c^* - c_L)\sqrt{\frac{D}{\pi t}}e^{-z^2/4Dt} \tag{2.1.20}$$

Consequently, the mass flux at $z=0$, is given by:

$$(j)_{t,z=0} = (c^* - c_L)\sqrt{\frac{D}{\pi t}} \tag{2.1.21}$$

where the group $D/\sqrt{\pi t}$ is the local value of the mass transfer coefficient.

If we consider a regular surface renewal (as first supposed by Higbie), i.e. that all the surface elements are exposed for the same time t_e, from equation (2.1.21) we get:

$$j = (c^* - c_L)\sqrt{\frac{D}{\pi t}}\int_0^{t_e}\frac{dt}{\sqrt{t}}$$

$$J = jA = 2\sqrt{\frac{D}{\pi t_e}}A(c^* - c_L) \tag{2.1.22}$$

Therefore, considering equation (2.1.11) we obtain Higbie's expression for the mass transfer coefficient:

$$k_L = 2\sqrt{\frac{D}{\pi t_e}} \tag{2.1.23}$$

Thus, the shorter the exposure time (t_e) the greater the mass flux at a given concentration difference.

2.1.2.3 Surface-renewal theory

Starting from Higbie's considerations Danckwerts (1951) supposed that each element of surface is not exposed for the same time, but that a randomly distributed frequency of exposure exists at the interface. Therefore the process of mass transfer can be schematized as depicted in Figure 2.4. Substantially, while in one interfacial region the mass transfer occurs into liquid elements in accordance with penetration theory, this region is also closer to another zone where well-mixed bulk liquid is present. The elements of liquid are not static but constantly exchanged by means of a random process.

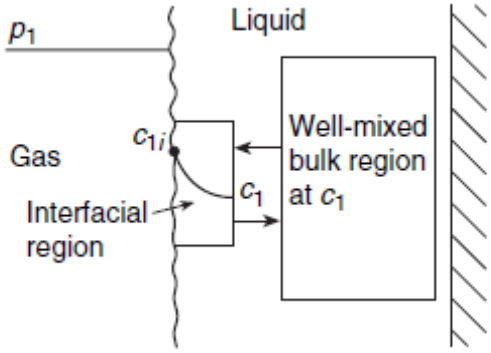

Figure 2.4 Surface-renewal theory scheme

Consequently the mass transfer rate will depend on the probability that a given liquid element will be close to the surface for a certain time *t*. Adopting an approach analogous to the one utilized to derive Higbie's theory, after some mathematical manipulations and simplifications we can write:

$$J = jA = 2\sqrt{Df}\,A(c^* - c_L) \tag{2.1.24}$$

where *f* is the rate of production of fresh surface area (s^{-1}).

The value of the surface-renewal theory is that it describes a more realistic situation with the same mathematical efforts of the penetration theory.

2.1.2.4 Other mass transfer theories and correlations of mass transfer coefficients

Among the previously explained theories for mass transfer, numerous models and relations have been developed to try to correlate the mass transfer coefficient with the properties of the involved fluids and the crucial aspects that can affect the diffusion process. An interesting review of the final results of these theories is summarised in the work of Kulkarni (2007).

The most common theories adopted to model the mechanism of mass transport in the liquid phase deal with the concept of surface renewal. As pointed out by Linek and co-workers (Linek et al., 2005) two important groups of models can be identified for the mass transfer from spherical bubbles.

The first group contains the so called "eddy models" which assume that the fresh liquid at the surface is supplied by the small-scale eddies of the turbulent flow field. Several similar relations were developed to take into account different eddy structures near the bubble vicinity. The most relevant aspect is all these models consider the eddy dimension to be much smaller in scale than the one of gas bubbles. For this reason bubble diameter is not a relevant parameter in the definition of the mass transfer coefficient. This doesn't mean that the bubble diameter is not relevant at all since from its value depends the extension of the surface through which the mass transfer occurs. These models all employ the same expression for the mass transfer coefficient k_L:

$$k_L = cD^{\frac{1}{2}}(\varepsilon\nu^{-1})^{\frac{1}{4}} \tag{2.1.25}$$

where:

D is the molecular diffusivity of the gas in the liquid (m²/s);

ν is the kinematic viscosity of the flow (m²/s);

ε is the turbulent energy dissipation per unit mass (m²/s³);

c is a constant.

Observing equation (2.1.25) it is possible to notice that the product $(\varepsilon\nu^{-1})^{-\frac{1}{2}}$ has the dimension of a time. Different values of the constant c were proposed by different authors, ranging from a maximum value of 1.13 (Kawase et al., 1987) for Newtonian liquids (this situation is equivalent to consider the original Higbie's penetration theory, equation (2.1.23), with the exposure time defined in relation (2.1.25)), to a minimum value of 0.4 (Lamont and Scott, 1970); a value of 0.592 was derived by Prasher and Wills (1973) from experimental data in a stirred tank.

The second group of models are the so called "slip velocity models", in which the fresh liquid close to the surface depend on the relative movement between the bubble and the surrounding fluid. For this kind of models the dependence on the bubble diameter is predominant. The first type of "slip velocity model" is that proposed by Higbie himself who considered, as claimed inside paragraph 2.1.2.2, the exposure time to be the ratio between the bubble diameter and the bubble rise velocity.

Different behaviours and different values of the mass transfer coefficient, k_L, are reported in scientific publications which deal with mass transfer from "small" and "large" bubbles. These ambiguous definitions are not the result of an inaccurate approach, but are rather a proof of the difficulty of determining the threshold between different behaviours, which does not depend solely on the bubble diameter. In fact, it would be more appropriate to distinguish between bubbles with rigid or mobile interface. This classification only shifts the problem to the definition of when and how a bubble behaves like one having a rigid or a mobile surface. Nevertheless, a physical explanation of this limit is much easier to identify. Actually, the mobility of the bubble interface is strongly related with the presence of contaminants or surface active contaminants (the so called surfactants) which tend to move along the bubble surface and accumulate towards the leeward side of the bubble. In regions of low surfactant concentration the interface is mobile. That is, the stress-free condition is approximately obeyed. However, in regions of high surfactant concentration, the interface becomes nearly rigid and is more closely described

by a no-slip condition (Ratulowski and Chang, 1990). This effect (*Marangoni effect*) implies that the surface tension gradients due to a concentration gradient of the surfactants laying on the bubble surface must be balanced by a jump of the shear stress across the interface, as a results, an increase of the drag force acting on the bubble occurs, consequently the bubble rise velocity is modified.

Several studies have been conducted at this regard (Dukhin et al., 1998; Linton and Sutherland, 1957; Frumkin and Levich, 1947). Substantially the accumulation of contaminants on the bubble surface makes the bubble to behave like a rigid sphere, leading to a of reduction of the rise velocity as well as diminishing the internal circulation in the bubble and the coalescence phenomena with other bubbles (Kulkarni and Joshi, 2005). Another relevant consideration, as pointed out by Vasconcelos et al. (2002), is that the surface mobility is related with the bubble diameter, since small bubbles have a greater probability to behave like a rigid sphere because they tend to spend a longer time in the liquid (due to their lower rise velocity) and consequently they are exposed to larger contamination periods. So a small bubble has initially a mobile surface which later becomes rigid.

Consequently two main types of relations have been developed to represent the mass transfer coefficient for a bubble with a rigid surface, and for a bubble with a mobile surface. Unfortunately, the diameter threshold where the transition from rigid to mobile surface occurs is not well known, because, as discussed just above, it depends on the contaminant concentration. Also tap water cannot be considered free from contaminants.

One of the most widely used relations for rigid bubbles was developed by Frossling (1938), who expressed the mass transfer coefficient in terms of Sherwood number, *Sh*, as:

$$Sh = 0.6\,\mathrm{Re}^{\frac{1}{2}}\,Sc^{\frac{1}{3}} \tag{2.1.26}$$

where:

Sh (Sherwood number) = $k_L d/D$;

Re (Reynolds number) = vd/ν;
Sc (Schmidt number) = ν/D;
d = bubble diameter (m);
D= molecular diffusion coefficient (m²/s);
v = bubble rise velocity (m/s);
ν = kinematic viscosity of the fluid (m²/s).

No specific region of validity is defined for Frossling relation, but it is usually applied to predict the mass transfer coefficient of bubbles with a diameter lower than 2 mm. Another similar relation was reported recently by Ahmed and Semmens (2003) and can be used to predict the mass transfer coefficients of bubbles with diameter lower than 2 mm and Re from 0.01 to 100:

$$Sh = 0.4911\,\mathrm{Re}^{0.3824}\,Sc^{0.33} \tag{2.1.27}$$

Other similar formulas have been proposed by Calderbank and Moo-Young (1961) who developed two different relations for the mass transfer coefficient of bubbles with diameter lower than 1 mm or greater than 2.5 mm. For bubbles with a mobile surface, besides the relation proposed by Calderbank and Moo-Young (1961) the traditional model proposed by Higbie seems to remain a valid model for the prediction of mass transfer in several situations (e.g. bubble column systems) as recently confirmed by the work of Vasconcelos et al. (2003).

A comparison between experimental results of several researches and different models proposed in literature, was performed by Motarjemi and Jameson (1978) as shown in Figure 2.5.

Experimental data were obtained considering the mass transfer of oxygen bubbles in tap water. It can be seen that the Higbie's model predicts well the mass transfer coefficient for different experimental observations (especially for $d_e \geq$ 1.5 - 2 mm).

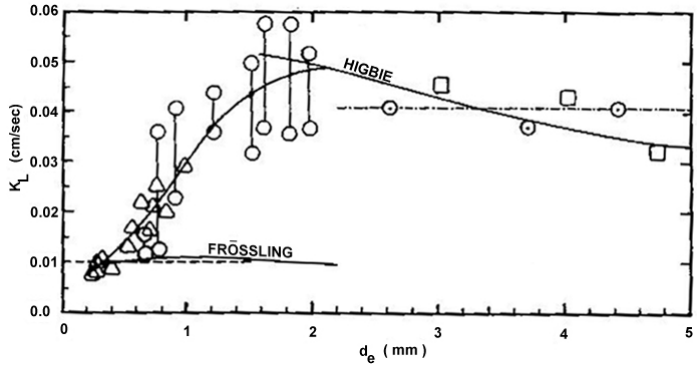

Figure 2.5 Mass transfer coefficient (k_L) versus bubble diameter (d_e), solid line: Higbie and Frossling models as depicted; dashed line: Calderbank and Moo-Young models for small and large bubbles; symbols: experimental data (Motarjemi and Jameson , 1978)

Another interesting work concerning the evaluation of the validity range for the application of mass transfer models based on the classical Higbie's penetration theory in terms of the intensity of the turbulent kinetic energy dissipation has been recently published by Alves et al. (2006).

Within their work, the authors considered bubbles of diameters ranging from 0.5 to 6 mm and concluded that, for the largest of turbulence energy dissipation value established during their experiments (0.04 m^2/s^3), the Higbie's model can still be used to evaluate the mass transfer from the bubbles to the surrounding liquid.

2.2 Interactions between bubbles and liquid

When describing the mass transfer model in paragraph 2.1.2, we considered the bubble rise velocity and briefly mentioned the drag force on the bubble itself. In fact, when a gas bubble or a swarm of gas bubbles is immersed into a liquid, the surrounding fluid exerts a system of forces on it: from the dynamic equilibrium of such forces depends the bubble movement inside the liquid. The

correct modelling of these forces is the first step to calculate the trajectory of the bubble, at least from a statistical point of view.

Moreover, some other phenomena influence the bubble behaviour when interacting with a liquid. In fact, bubbles may interact and collide and phenomena like bubble coalescence, break-up and distortion may take place.

2.2.1 Hydrodynamic force balance

If we consider a bubble the resultant force acting on it can be summarised by the relation:

$$\vec{F} = \vec{G} + \vec{F}_A + \vec{F}_D + \vec{F}_B + \vec{F}_{AM} + \vec{F}_L \tag{2.2.1}$$

where:

F = resultant force (N);
G = weight force (N);
F_A = Archimedes force (N);
F_D = drag force (N);
F_B = Basset force (N);
F_{AM} = virtual mass force (N);
F_L = lift force (N).

Calculating the resultant from Archimedes and weight forces we obtain the expression of the buoyancy force, which can be determined by:

$$\vec{G} + \vec{F}_A = \vec{g} W_b \left(\rho - \rho_g \right) \tag{2.2.2}$$

where:

g = gravitational acceleration (m/s²);
W_b = bubble volume (m³);
ρ = density of the liquid phase (kg/m³);

ρ_g = density of the gas phase (kg/m³).

2.2.1.1 Drag and lift forces

Drag force is the resistance force due to non-uniform distribution of stresses (pressure and viscous stresses) on the bubble surface. Streamlines change their direction when flow past an immersed body, thus velocity changes (and consequently acceleration) arises, leading to the development of a hydrodynamic force which usually has a positive component in the direction of flow motion, i.e. opposite to the direction of bubble motion. The relative contribution of pressure and friction drag depends on the bubble shape. The total drag is expressed by:

$$\overrightarrow{F_D} = \frac{1}{2} C_D \rho A \left(\vec{V} - \vec{U}\right)\left|\vec{V} - \vec{U}\right| \tag{2.2.3}$$

where:

A = cross-section normal to the flow direction (m²);
C_D = drag coefficient;
U = fluid velocity (m/s);
V = particle velocity (m/s).

Hence, the total drag experienced by the bubble is a function of the drag coefficient, C_D, which depends on the Reynolds number of the bubble ($Re = vD/\nu$) and on its shape. Considering a spherical bubble, when Re is much smaller than unit there is no flow separation in the rear of the sphere, the flow is laminar and the drag is essentially due to viscous stresses, so drag coefficient can be evaluated by Stokes's relation:

$$C_D = \frac{24}{\mathrm{Re}} \tag{2.2.4}$$

Stokes's relation fails for greater values of *Re*, when the drag is a combination of pressure (owing to stagnation on the front of the bubble and separation of the flow on the rear) and friction contribution and a progressive drop of the drag coefficient occurs until the value of about 10^3 is reached; for 10^3>Re>10^5 the drag coefficient curve is substantially flat as shown in Figure 2.6.

An approximation of the drag coefficient curve can be evaluated by the expression proposed by Schiller and Naumann (1935):

$$C_D = \begin{cases} \dfrac{24}{\mathrm{Re}}\left(1 + 0.15\,\mathrm{Re}^{0.687}\right) & \text{for } \mathrm{Re} < 1000 \\ 0.44 & \text{for } \mathrm{Re} \geq 1000 \end{cases} \qquad (2.2.5)$$

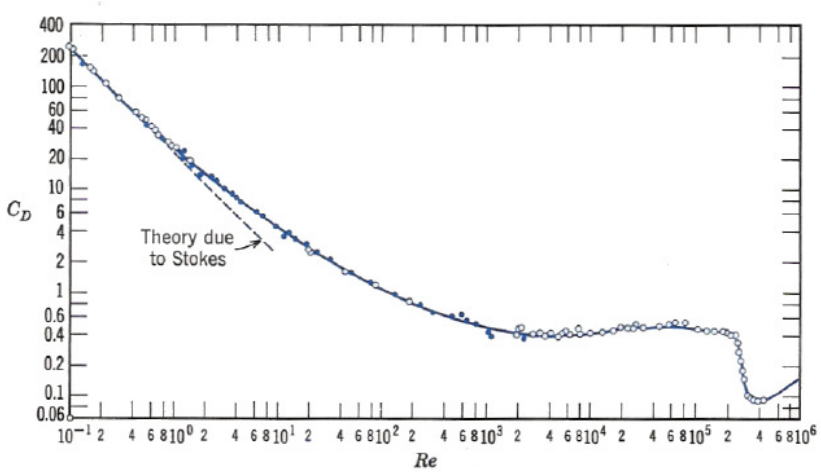

Figure 2.6 Drag coefficient for a rigid sphere

It must be pointed out that equation (2.2.5) is one of the simplest relations developed for a single bubble immersed in a fluid. A more accurate estimation of the drag coefficient of bubbles within aeration systems should take into account the fact that bubbles are not isolated but usually embodied in a swarm

of bubbles where any of them may interact with each other. Moreover some other complications can arise from the presence of contaminants inside water, which produce an increase of the total drag of the bubble (as discussed in paragraph 2.1.2.4) or from the fact that bubble may deform its shape. Relations from various authors have been summarised in the review of Kulkarni and Joshi (2005).

Furthermore, a non-uniform distribution of viscous and pressure stresses on the bubble surface leads to the generation of a non-zero component of the hydrodynamic force in the direction normal to the oncoming flow direction: the lift force. This force can be expressed similarly to the drag in equation (2.2.3) except for the substitution of C_D with the lift coefficient C_L. We can point out that, if the flow has the same direction of the principal chord line of the immersed body, the stress distribution is balanced on the two sides of the bubble and the lift force disappears. Therefore if we consider a symmetrical flow past a sphere, lift force can be neglected. Nevertheless, the lift force should be taken in to account if the bubble is located in a zone of high turbulence where the flow may be non-symmetrical or where the shape of the bubble is deformed. Lift forces may arise also for particle rotation either induced by strong shear flow (velocity gradients may cause high pressure difference between top and bottom of the bubble) or wall contact.

2.2.1.2 Virtual mass and Basset forces

The virtual mass force and Basset force are unsteady forces related to the change of the relative velocity of a body submerged in a fluid.

The virtual mass force (or added mass force) takes into account the effects of the variation of the liquid flow velocity on the bubble dynamics. If the fluid is accelerated also the bubble must be accelerated and vice-versa. The added inertia introduced can be taken into account by considering a bubble which is

heavier than it really is as a consequence of the fluid mass pushed away. Consequently, we can calculate the virtual mass acting on the bubble as:

$$\overrightarrow{F_{AM}} = C_{AM}\rho W_b\left(\frac{d\vec{U}}{dt} - \frac{d\vec{V}}{dt}\right) \tag{2.2.6}$$

where:

C_{AM} = added mass coefficient.

Delnoij et al. (1997) carried out a Euler–Lagrange simulation of a partially aerated bubble column and concluded that added mass force plays an important role in the vicinity of the gas distributor. The determination of C_{AM} is still a subject of research for many investigators, but for a spherical bubble which translates without rotation in an unbounded inviscid fluid the value of 0.5 can be adopted.

The Basset force represents instead the effect due to the fast acceleration of the fluid (or of the particle) which leads to a delay in the development of the boundary layer, with the consequent enhancement of the drag effects. It's also usually referred as history force. A possible expression for the history force term for a spherical bubble, including the effect of an initial relative velocity is given by Crowe et al. (1978):

$$\overrightarrow{F_B} = \frac{6\pi r^2\mu}{\sqrt{\pi\nu}}\left(\int_0^t \frac{d}{d\sigma}\left(\vec{V}-\vec{U}\right)\frac{d\sigma}{\sqrt{t-\sigma}} + \frac{\overrightarrow{U_0}-\overrightarrow{V_0}}{\sqrt{t}}\right) \tag{2.2.7}$$

where:

r = bubble radius (m);

μ = dynamic viscosity of the liquid (Pa·s);

σ = integration variable (s).

2.2.2 Influence of the bubbles on the surrounding fluid

We just mentioned that mutual interactions may take place between bubbles, but it is equally important to consider the influence that bubbles exert on the surrounding fluid. In fact, if the gas volume fraction is large enough the bubbly flow can have a strong interaction with the fluid, modifying the fluid flow with the consequence that the momentum exchange between gas and liquid phase must be taken into account. Therefore, we can distinguish between bubble-driven flow and liquid-driven flow, depending on which is the phase that takes the most significant role in the control of the two phase fluid motion.

An interesting study concerning the effect of the horizontal gas-liquid injection in a water tank has been recently proposed by Lima Neto et al. (2008). In their study they investigated the effect of gas volume fraction on the behaviour of the bubble plume and on the liquid jet. The gas volume fraction is:

$$\varepsilon = \frac{Q_g}{Q_g + Q_w} \tag{2.2.8}$$

where:

ε = gas volume fraction;
Q_g = gas flow rate at the nozzle exit (m³/s);
Q_w = water flow rate at the nozzle exit (m³/s).

Their experiments were carried out at a Reynolds number Re_n at the nozzle, ($Re_n = ud_n/\nu$, where d_n is the nozzle diameter) ranging from 10600 to 24800 and for gas volume fractions between 0.13 and 0.63. They observed the presence of two definite regions: a quasi-horizontal bubbly jet and a quasi-vertical bubble plume, They found that for gas volume fractions smaller than 0.15 the water jet completely separates from the bubble flow while for higher values the water jet initially follows the trajectories of the bubbles in the bubbly jet region and then

separates from the bubble core at some distance from the nozzle exit, becoming a surface water jet.

This study shows therefore that the influence of the bubbly flow on the liquid flow field can be considered small when the gas fraction volume is lower than 0.15.

Similar considerations have been drawn by Rainer et al. (1995) who observed that for the particular jet system examined, "*the structure of the gas liquid jet (created by a hydro-ejector) was shown to be emulsion-like with small bubbles following the jet-liquid path*".

2.3 Numerical computing of two-phase flow systems

During the last twenty years great efforts have been spent into the numerical modelling of multiphase flows, and now we can make use of the computational tools produced in this branch of computational fluid dynamics (CFD).

A preliminary macroscopic distinction among the numerical methods developed for turbulent two phase systems distinguish between Euler-Euler methods (E-E) and Euler-Lagrange methods (E-L) (Gouesbet and Berlemont, 1999, Crowe et al., 1996).

The main difference between the two approaches is the coupling and modelling methods adopted for the continuous and dispersed phase.

Into E-E methods the dynamics of both phases are solved in a Eulerian frame by means of the Navier Stokes (N-S) equation coupled with an equation for the time evolution of the concentration of the dissolved bubbly phase in the liquid one. In practice, not only the continuous phase, but also the dispersed phase is considered as a pseudo-continuous phase.

The E-L methods still solve the continuous phase by means of the Navier-Stokes equations, while the dispersed phase is followed in its motion inside the reactor by solving the balance equation of the hydrodynamic forces acting on each discrete particle. Moreover, different methods can be distinguished on the basis of the complexity level considered for the evaluation of the interaction between the two phases.

The lowest level of complexity includes the so-called "one-way coupling" problems, in which the dispersed phase can be simply considered as carried by the continuous phase and it is assumed that the dispersed phase exerts negligible effects on the carrier fluid. In "two-way coupling" problems it is necessary to take into account the fact that the behaviour of bubbles is influenced by the flow field, and they, in turn, can influence the characteristics of the surrounding flow field. Finally, the most complex problems, in which the effects related to interactions within the dispersed phase, such as the phenomena of coalescence and break-up of the bubbles, are taken into account belong to the "four-way coupling" kind.

Many authors have numerically examined the hydrodynamics of gas-liquid systems, focusing in particular on the aeration columns, for which both the E-L (Lain et al. 2002; Lapin and Lübbert, 1994; Delnoij et al., 1997, Wuest et al., 1992) and E-E methods (Pfleger and Becker, 2001; Sokolichin et al., 2004) were applied.

More rare in the literature are CFD applications to systems where mixing and aeration are obtained by means of turbulent jet. The studies conducted by Patwardhan (Patwardhan , 2002) and Jayanti (Jayanti, 2001) evaluate the mixing efficiency of a jet system, however considering only the liquid phase.

Numerical studies which deal with mass transfer phenomena are available on bubble columns, using both E-E (Wiemann and Mewes, 2003; Mewes and Wiemann, 2005; Lehr et at., 2002) and E-L methods (Gong et al. 2007; Darmana et al. 2005; Krishna and van Baten, 2003, McGinnis and Little, 2002). Recently some applications of CFD focused their attention both on lab-scale models of two-phase systems of wastewater treatment plants (Le Moullec et al., 2008) and on full-scale tanks (Huang et al. 2009; Fayolle et al., 2007).

Finally, the work of Morchain et al. (2000) evaluates the effect of a free-oxygen cross flow on the oxygen transfer of a two-phase jet aerator installed in a large vessel. The authors limited their attention to solve the balance equation of the dissolved oxygen concentration by considering only an overall uniform

mass transfer coefficient ($k_L a$) restricted to the portion of the physical domain where gas bubbles are present; no bubble motion is taken into account.

Chapter 3

Biological treatment of wastewater: processes inside the oxidation tank

3.1 Introduction

Water pollution is one of the most important environmental issues. Natural water reservoirs have their own self-purifying capacity based substantially on the adjustment of the balance between nutrients, biodegradable substrates and biomass, which allows to remove some of the pollutants being discharged into the environment.

However, the self purification capacity and the resilience of natural water bodies are not capable of withstanding the pollutant loads imposed by the presence of human activities (domestic, industrial and agricultural) that characterize almost any human settlement. The dumping of untreated water in water bodies inexorably leads to compromise the delicate balance of ecosystems leading to the onset of very serious environmental problems such as disease outbreaks, eutrophication, vegetal and animal species die-off, transmission of diseases through the chain food, impaired use of water resource for drinking or irrigation purposes, and so on.

The occurrence of these problems can be controlled through preventive treatment of wastewater to ensure adequate concentrations of contaminants into the final effluent that will not endanger human and ecosystem health. The incoming water in a wastewater treatment plant will be treated in order to bring down the content of solids, organic and inorganic matter, nutrients, heavy metals and undesired microorganisms.

What differentiates a natural system from a water treatment plant is the high concentration of pollutants and actors called to its depletion. For this reason, the treatment process requires constant monitoring to ensure optimal conditions for each unit process in order to achieve the goals of treatment for which it has been designed. In particular, biological oxidation tank is the key unit of every activated sludge wastewater treatment plant since aerobic microorganisms are here called to assimilate the organic matter entering the plant and maybe to obtain the nitrification of ammonium ions.

An adequate and uniform supply of oxygen inside the biological tank is essential to provide the complete removal of biodegradable substrate since it is consumed by the heterotrophic biomass which needs dissolved oxygen for its growth. It has been observed that the concentration of dissolved oxygen mustn't decrease under the threshold level of 2 mg/l to avoid microbial stress and the consequent unsatisfactory degradation of organic matter.

Nevertheless, the biological removal of organic matter is not the only fundamental process that usually takes place inside an aeration tank. For example, as mentioned earlier, nitrification process is usually carried out at the same time as the degradation of organic matter, for example. Moreover, several types of microbial population and substrate with different degree of biodegradability are usually present simultaneously. Thus, it appears immediately that the detailed description of the activated sludge behaviour needs to take into account a large number of components and reaction between them.

The detailed description of such phenomena is not the aim of the present dissertation, since what we want have is simply to test the applicability of CFD

tools to the analysis of the multiphase-biologically reacting flows which characterize these processes. In other words, we want to show how the prediction of the hydrodynamics inside the oxygenation tank (equipped with a jet aerator) with the correlated mass transfer from oxygen bubbles allows us to obtain the time evolution of the concentration of dissolved oxygen and of the basic components involved inside the reactor: heterotrophic biomass and readily biodegradable organic matter. Of course, the analysis of more realistic and complex processes is straightforward once this preliminary result is achieved.

For this reason, only the relations describing dissolved oxygen consumption, biomass growth and substrate removal are considered herein.

3.2 Biomass, substrate and dissolved oxygen within a bioreactor

To represent the time behaviour of heterotrophic biomass, substrate and dissolved oxygen we have to describe the main mechanisms involved during the processes that lead, under suitable assumption, to the formulation of the commonly used models.

For this reason biomass, substrate and dissolved oxygen kinetics models are here presented.

3.2.1 Kinetic relations from microbiology

To describe how the depletion of readily biodegradable substrate takes place, we have to consider that each environmental system has its roots in the nutritional requirement of microorganisms, which has to be satisfied to let the biomass grow and hence to keep the system in equilibrium conditions.

The main functions carried out by nutrients are to provide the material required for synthesis of cytoplasmic material of microbial cells, to serve as an energy source for cell growth and biosynthetic reactions and to serve as acceptors for the electrons released in the energy-yielding reactions.

Heterotrophic biomass is composed by such microorganisms (mainly bacteria) that carry out the depletion of relatively complex, reduced organic compounds (such as glucose). They consider the organic carbon as the sole source for energy and synthesis of new cells.

Heterotrophic aerobic biomass needs dissolved oxygen as electron acceptor for the oxygenation of the carbon substrate. A typical reaction is the decomposition of glucose, which can be summarised as follows:

$$C_6H_{12}O_6 + 6O_2 \rightarrow CO_2 + H_2O \tag{3.2.1}$$

The first term on the left hand side of the reaction (3.2.1) is the glucose molecule that works as electron donator for the reaction. The final products are carbon dioxide and water.

The assimilation of organic compounds by microorganisms takes place by means of enzymes that catalyze chemical reactions.

If we consider the growth of bacterial cells placed in a system where substrate is present in a non-limiting concentration the behaviour of cell growth can be divided into six stages (Monod, 1949) as shown in Figure 2.1:

- lag phase: in this phase microorganisms have to adapt to the new environment. The growth rate is null;
- acceleration phase: during this phase an increasing growth rate is established;
- exponential phase: in this phase the time required for generation of new cells is the lowest, whilst the growth rate is maximum and constant;
- declining growth phase: during this stage the time requested by the generation of new cells increases; in the same time a decrease of the specific growth rate due to the gradual depletion in substrate concentration takes place;
- stationary phase: in this stage the exhaustion of nutrients occurs and the balance between growth and death of microbial cells may be reached;

– endogenous phase: during this phase endogenous metabolism (resynthesis of new cells from endogenous carbon source) takes place, the death rate increase and microbial cell lysis occurs.

–

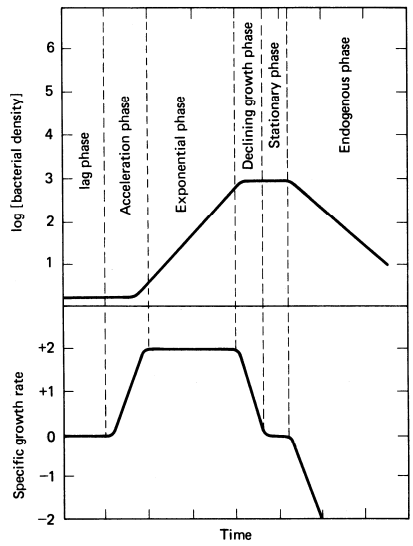

Figure 3.1 Characteristic growth curves of cultures of microorganisms (Benefield and Randall, 1980)

It must be observed that the growth cycle can be controlled by imposing the right environmental conditions in order to maintain the exponential phase for a long period of time. If we consider that all the environmental requirements are satisfied, the growth rate of biomass (Δx) is proportional (through a constant μ) to the biomass concentration (x) :

$$\Delta x = \mu x \Delta t \tag{3.2.2}$$

$$\frac{dx}{dt} = \mu x \tag{3.2.3}$$

Integrating equation (3.2.3) from the initial biomass concentration x_0 to the concentration at time t=0 we obtain:

$$x = x_0 e^{\mu t} \tag{3.2.4}$$

If the biomass growth rate follows equation (3.2.4) the exponential growth phase is established. The parameter μ has the dimensions a frequency and represents the *specific growth rate* (rate of growth per unit amount of biomass).

An extension of this approach that contains both exponential and declining growth phase was proposed by Monod (1949), who argued that the biomass growth depends on substrate availability as expressed by:

$$\frac{(dx/dt)}{x} = \mu = \mu_m \frac{S}{K_S + S} \tag{3.2.5}$$

where:

μ_m = maximum value of the specific growth rate at saturation concentrations of growth-limiting substrate (s^{-1});

K_s = saturation constant, it corresponds to the substrate concentration at which $\mu = \mu_m/2$ (kg/m³);

S = substrate concentration (kg/m³).

Relation (3.2.5) (represented in Figure 3.2) has the same structure of the Michaelis-Menten (1913) equation, developed to describe the saturation effects of an enzyme with its substrate.

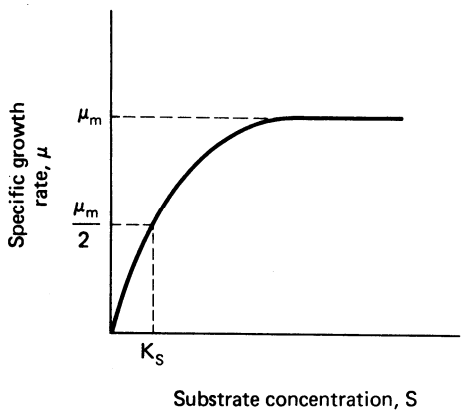

Figure 3.2 Relation between specific growth rate and substrate concentration (Benefield and Randall, 1980)

Depending on the substrate concentration, equation (3.2.5) can be simplified in order to highlight the predominant kinetics order. If the substrate concentration is considerably lower than the saturation constant value ($S<<K_S$), a direct proportionality of the specific growth rate to S is established (first-order kinetics). On the other hand if the substrate concentration is much higher than the saturation constant, the specific growth rate doesn't depend anymore on the substrate concentration and the relation approaches a zero-order kinetics.

It can be noticed that wastewater treatment plants are designed to operate with very high substrate concentration, so in many practical situations a zero order kinetic model can describe with the necessary approximation the biomass growth inside the reactor.

Moreover, we can notice that relation (3.2.5) only considers the assimilative growth of the biomass, while it is known that during assimilative growth, a part of bacteria cells decays as a consequence of endogenous metabolism, death, predation and lysis. For this reason a more complete model must include a relation which describes the endogenous decay; consequently, the net growth rate of biomass can be estimated through:

$$\left(\frac{dx}{dt}\right)_N = \mu_m \frac{S}{K_S + S} x - bx \tag{3.2.6}$$

where b is the coefficient of endogenous decay and the subscript N stands for "net growth rate".

An extension of the Monod model considers the simultaneous presence of a second limiting substrate, often representing dissolved oxygen (this is the choice of the Activated Sludge Models developed by IAWPRC task group, 2000). Considering only the assimilative growth rate, we can define a double Monod kinetic model in the form:

$$\frac{dx}{dt} = \mu_m \frac{S}{K_S + S} \frac{S_1}{K_{S1} + S_1} x \tag{3.2.7}$$

where, S_1 is the second limiting substrate concentration and K_{s1} is its saturation constant.

Substrate depletion kinetics can be described via a Monod type relation, considering that, as the biomass grows, the substrate diminishes with a relation that must involve the yield of conversion of the substrate into new biomass. A widely used relation can be written as follow:

$$\frac{dS}{dt} = -\frac{1}{Y}\frac{dx}{dt} \tag{3.2.8}$$

where Y represents the yield of conversion of the substrate carried out by the biomass.

It has to be observed how, if another limiting substrate is considered in order to better describe the environmental conditions which may affect the bacteria growth, the same conditions have to be taken into account for the substrate

depletion kinetics, considering equation (3.2.7) instead of the most commonly used relation (3.2.5).

As previously mentioned, heterotrophic bacteria need for their growth and maintenance a certain amount of dissolved oxygen, which has to pass through the bacterial cells in order to be available for the oxidation-reduction reactions necessary to recover energy. In particular, inside a wastewater oxidation tank oxygen requirements derive from carbonaceous and nitrogenous biochemical oxygen demand and from inorganic chemical oxygen demand.

This relation is well known and widely used, since biochemical oxygen demand (BOD) is one of the first parameter used to characterize the biodegradability features of the broth entering the treatment. Actually, if the organic content of water is low, then the oxygen requirement of the bacteria will be low; on the other hand, if the organic content is high, the oxygen requirement of the bacteria will also be high.

If we don't consider the presence of nitrogenous substances in the water, dissolved oxygen consumption due to bacteria activity can be expressed with a law which takes the Monod form:

$$\frac{dS_{DO}}{dt} = -\frac{1}{Y'}\left(\mu_m \frac{S}{K_S + S} x - bx\right) \tag{3.2.9}$$

where *Y'* represents a yield coefficient for the dissolved oxygen consumption by biomass.
Similarly, we can describe the requested BOD (S_{BOD}) by:

$$\frac{dS_{BOD}}{dt} = -\frac{dS_{DO}}{dt} \tag{3.2.10}$$

In conclusion, we want mention that recently another model has proved to be successful in practice, due to its showed ability to fit experimental data and it

has been widely used in describing the growth of microorganisms: the logistic model. The logistic model is a sigmoidal shaped model and, as claimed by Koku et al. (2003), it appears to be able to describe a great part of the growth curve, starting from the lag phase (if present) to the stationary phase. Considering a first order kinetic to describe the biomass growth, logistic equations permit to obtain an explicit relation to evaluate at any time *t*, the biomass, substrate and oxygen concentrations knowing the initial concentration values.

3.2.2 Pure oxygen aeration: critical review

Many authors spent their efforts to compare advantages and disadvantages of pure oxygen aeration systems compared with traditional air systems. For Kalinske (1976) the improvements claimed by proponents of pure oxygen systems are not so evident if compared with the behaviour of a traditional aeration system, since it seems to be necessary only to preserve a dissolved oxygen concentration inside the reactor at levels above 2 mg/l to obtain the same results. Another disadvantage claimed is that excessive levels of dissolved oxygen can be toxic to nitrifying bacteria and lead to the production of filamentous bacteria (increasing danger of bulking).

However Kalinske's work has been harshly criticized by Chapman et al. (Chapman et al., 1976).

Anyway, pure oxygen systems are still widely used especially for their flexibility and for the demonstrated capability to follow peak loads and hence peak oxygen requests during the transition that inevitably occurs during operation conditions. Moreover, inside Benefield and Randall work (1980) some advantages related to pure oxygen systems are highlighted over an air aeration system:

- Greater oxygen requests are more easily satisfied;
- higher concentration of Mixed Liquor Volatile Suspended Solids (MLVSS) can be maintained inside aeration tank and

thus the same treatment can be done in a smaller-volume reactor;

- sludge settleability and thickening are increased;
- production of sludge diminishes per unit BOD removed;
- more efficient oxygen transfer to liquid per unit power consumed;
- improvement of the stability of the treatment.

Chapter 4

Eulerian –Lagrangian model for the simulation of the time evolution of dissolved oxygen, biomass and substrate in a confined environment

4.1 Structure of the numerical model: modelling approach

Within paragraph 2.3, we have observed that, for the numerical modelling of two-phase flows, different approaches can be adopted. This chapter describes the structure of the model used to simulate the time evolution of the concentration of dissolved oxygen originally transferred to the flow from the bubbles of oxygen injected through a turbulent jet. Moreover, the extension of the model to compute the time evolution of the concentration of other species (i.e. heterotrophic biomass and biodegradable organic substrate) will also be taken into account.

A first aspect that needs to be highlighted is the scale at which we want to describe the phenomenon, which determines the choice of some assumptions underlying the model. The increasing availability of computing resources characterized by higher performance has led in recent years to model fluid flow phenomena with extreme accuracy. The precise representation of the interactions that occur between bubbles in motion within the flow field and the surrounding fluid, of how the bubbles are able to change the hydrodynamic characteristics of the carrier fluid and how, consequently, these interactions act on the bubble trajectory, on their shape and their behaviour in relation to other physical phenomena involved, is beyond the scope of this research work even though it can be a topic of great interest from some other scientific points of view. In fact, the work carried out has been aimed to an engineering approach to the key aspects of oxygen dissolution in wastewater treatment plants.

The choice of the analyzed operational conditions has been driven by the need to keep close to what occurs in real plants or, at least, in lab-scale models of the involved processes. In particular, the gas flow rate injected into the system was maintained (during both experimental and numerical activities) at low values of gas volume fraction such that the observations of Lima Neto et al. (2008) could justify the approach adopted.

In particular, a "one-way coupling" model was adopted, in which the effects of interactions between bubbles and fluid, and consequently the exchange of momentum between the phases, could be neglected. It was then assumed that the bubbles are transported by the fluid without any noticeable change in the flow field induced by the carried bubbles. This assumption has enabled us to evaluate separately the fluid flow field and the evolution of the bubbly gas phase convected by the fluid flow.

The first step involved the determination of the fluid flow field under steady-state conditions. A finite volume method (FV) was then adopted to obtain the solution of Reynolds Averaged Navier-Stokes equations (RANS). The code

allows the calculation of the characteristic quantities of the flow field on a cartesian grid (Eulerian approach).

The second step represents the central part of the developed model: the fluid flow field, determined as described above, is used (together with the measurement of the bubble size distribution representative of the gas flow) to evaluate convection and turbulent dispersion of the injected gas bubbles within the environment. Each bubble moves as a result of the convection of the fluid, of the dynamic actions acting on it and of the dispersive effect of the turbulent flow field, represented trough a random walk contribution (Lagrangian approach).

The third step is the solution of a balance equation for the dissolved oxygen concentration and of a balance equation for the concentration of any other dissolved species for which the determination of the evolution in time within the domain of calculation is needed. Here we return again to an Eulerian approach, determining the evolution of the concentration due to diffusive and convective phenomena (related to the flow field) and to the effect of production and sink terms of this species over time. Especially with regard to oxygen, this corresponds to the modelling of mass transfer between gas and liquid phase (and vice versa) that will depend on the position reached by the bubbles.

Within this chapter we focus our attention on the description of the second and third step of the model, i.e.. the steps which estimate the evolution of oxygen concentration starting from the modelling of the bubble movement. We will here assume to have already available the main inputs of the model: the detailed knowledge of the liquid velocity field and the bubble size distribution. The methodology that allows us to obtain these two quantities will be described in more detail inside Chapter 5.

4.2 Modelling of the bubble dynamics

4.2.1 Bubble injection

The first issue regards the way in which injection of bubbles inside the system is represented in order to meet the defined gas flow rate.

To simulate the injection of bubbles by a circular jet, several injection points were distributed at the nozzle exit (bubble inflow boundary conditions) within its circular cross section. This choice yields a bubble distribution that is more widespread than the one of the two-phase jet at the nozzle exit, since the injection does not take place only at the nozzle centre but is distributed in the whole nozzle exit section.

Once the injection points have been defined the bubble size distribution (BSD) is considered. For each dimensional class, the bubble diameter (d_i) and the correspondent volume percentage (p_i) needs to be specified. The total number of bubbles (which influences the RAM memory needed by computer runs) that will be present in the system results from:

$$n_{\max} = n_{in}\left(\frac{t_p}{\Delta t_p}+1\right)n_d \tag{4.2.1}$$

where:

n_{max} = maximum number of bubbles;
n_{in} = number of injection positions;
t_p = overall duration of bubble injection;
Δt_p = injection time step;
n_d = number of dimensional class included in the BSD.

The time step Δt_p adopted for the bubble injection is now calculated on the basis of the time step Δt (see paragraph 4.3.2.5) necessary to compute the

trajectory of particles and to update the concentration of the dissolved species, represented by the symbol Δt.

The total number of bubbles that will be inserted at each inflow position, n_{in}, is calculated with respect to the imposed gas flow rate Q_g, in order to impose implicitly the mass balance for the gas phase:

$$n_i = \frac{p_i Q_g \Delta t_p}{W_i n_{in}} \tag{4.2.2}$$

where:

n_i = number of inserted bubbles with diameter equal to d_i;

W_i = bubble volume with diameter equal to d_i;

p_i = volume fraction of the bubble with diameter equal to d_i.

So, at each injection time step the total number of bubbles entering the computational domain and respecting the initial BSD is the result of the summation of n_i over the number of injection positions. It has to be highlighted that what is in fact inserted at each step and insertion point is not a real bubble but rather what could be defined as a "computational bubble". Actually, even if the n_i bubbles injected inside the system at a given position are considered as single bubbles in order to evaluate the mass transfer, the simulation of their movement is obtained by considering the n_i bubbles at each injection as a "cluster" of bubbles, which moves rigidly since all the bubbles belonging to it have the same geometrical characteristics and since they are inserted at the same moment.

The insertion of new bubbles takes place at fixed time steps within the total inflow time. The interval between these time steps is calculated on the basis of the previously mentioned computation of $\Delta t_{p.}$

4.2.2 Bubble movement

Now we have to consider how the bubble injected inside the system moves. We've already mentioned, within paragraph 4.1, that the bubble velocity is the result of three independent contributions.

We will analyse each of them inside the following paragraphs.

4.2.2.1 Bubble velocity due to the liquid flow field

When a "bubble" (or, better, a "computational bubble" representative of n_i bubbles of the same diameter d_i) moves in the computational domain its position is defined, since the position of its centre (coordinates x,y and z) becomes one of the parameter associated to each bubble. From the bubble position, it is immediate to get the cell occupied by the bubble.

For each vertex of each grid cell, the liquid flow field properties are defined: velocity, turbulent kinetic energy and turbulent kinetic energy dissipation. The correspondent value of these properties in the position of each bubble is then calculated by interpolation with respect to the position of the bubble inside the cell, by means of a weighted method where the weight-coefficients are determined evaluating the distance of the particle from each vertex.

In particular, taking as example the scheme shown within Figure 4.1, defining x_i, y_i and z_i the components of the relative position vector of the bubble i from vertex V, we can define the quantities α,β,γ as:

$$\begin{aligned} \alpha &= -1 + 2(x_i - x_v)/\Delta x \\ \beta &= -1 + 2(y_i - y_v)/\Delta y \\ \gamma &= -1 + 2(z_i - z_v)/\Delta z \end{aligned} \qquad (4.2.3)$$

where:

x_v, y_v, z_v, are the coordinates of the vertex V;

Δx, Δy, Δz, are the lengths of the cell edge along x,y and z direction respectively;

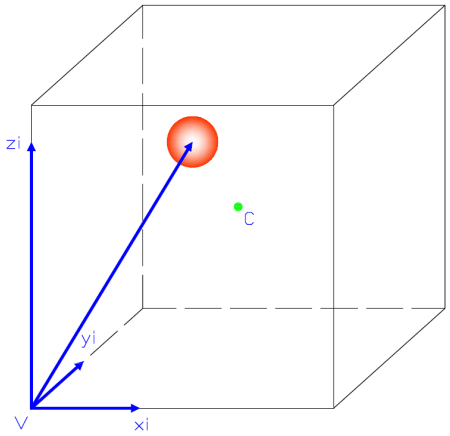

Figure 4.1 Interpolation of the bubble properties inside a computational cell

The weight coefficients, for each vertex n of the cell, f_n are then calculated considering the eight combinations deriving from:

$$f_n = 0.125(1 \pm \alpha)(1 \pm \beta)(1 \pm \gamma) \tag{4.2.4}$$

Finally, we the interpolated bubble velocity V_{fi} related to the liquid flow field, the turbulent kinetic energy k_i and the turbulent kinetic energy dissipation ε_i are obtained by interpolation on the values in the eight vertices as:

$$\overrightarrow{V_{fi}} = \sum_{n=1}^{8} f_n \cdot \overrightarrow{U_n} \tag{4.2.5}$$

$$k_i = \sum_{n=1}^{8} f_n k_n$$

$$\varepsilon_i = \sum_{n=1}^{8} f_n \varepsilon_n$$

Inside equation (4.2.5) the variables defined for each single vertex are indicated with the subscript *n*, while the subscript *i* indicates that the property under consideration is a characteristic value for the *i*-th bubble. The *U* symbol stands for the fluid flow velocity, while the *V* indicates the bubble velocity.

Hence, considering equation (4.2.5) the first relation represents the first contribution to the final bubble velocity due to flow convection.

4.2.2.2 Bubble velocity due to hydrodynamic force balance

Inside Chapter 2, all of the forces that act on a bubble immersed into a fluid were considered.

For the calculation of the hydrodynamic balance of the forces acting on a bubble inside the computational domain, some basic assumptions have been made. In particular some of the terms highlighted in paragraph 2.2 have been considered negligible in the definition of the trajectory followed by each bubble. Above all, the time needed by the bubble to reach the stationary conditions was considered short enough to neglect the relative acceleration between bubbles and fluid. So the terms related with transition phenomena such as the Basset force and the virtual mass force have been neglected inside the calculation.

In particular, the decision to neglect the added mass force term has been supported by the comparison of the effects related to its consideration inside the calculation with respect to the "uncertainty" of the final results related to the consideration of the turbulence effects on the trajectory followed by the bubble (see paragraph 4.2.3.1).

Another term that it has been not considered is the lift force. This simplification finds its theoretical justification if the bubble shape is considered to be spherical independently from the bubble diameter; moreover it has been considered that the bubble shape doesn't change during its motion. So, if we admit that the fluid flow past the bubble is always symmetrical and no bubble rotation arises, for the reason explained inside paragraph 2.2.1.1 the lift force can be neglected.

So, starting from equation (2.2.1) we can write the equation of bubble motion as:

$$\rho_g \frac{\pi d_i^3}{6}\frac{dV_i}{dt} = \frac{\pi d_i^3}{6}\rho_g g - \frac{\pi d_i^3}{6}\rho g + \\ -\frac{\pi d_i^2}{8}\rho C_D (V_i - U)|V_i - U| \tag{4.2.6}$$

where the left hand side term represents the resultant force acting on the bubble (its mass multiplied by its acceleration), while the right hand side terms are the weight force, the Archimedes force and the drag force respectively. The symbol U stands for the liquid flow velocity, ρ is the liquid density, ρ_g is the oxygen density and d_i is the diameter of the *i-th* bubble.

Finally, we have to consider that quasi-steady conditions are assumed during each time step of integration and that the bubble is considered to adapt instantly to changes in flow velocity (i.e. the transient during with drag arises owing to a difference between fluid and bubble velocities other than the one due to rise velocity is short). Then, the hydrodynamic force balance reduces to the equilibrium between buoyancy and drag force, as follows:

$$\overrightarrow{F_D} + \vec{B} = 0 \tag{4.2.7}$$

where *B* represents the buoyancy force. Developing equation (4.2.7) leads to:

$$\frac{\pi d_i^2}{8}\rho C_D (V_{li})^2 = \frac{\pi d_i^3}{6} g(\rho - \rho_g) \tag{4.2.8}$$

Inside equation (4.2.8) the velocity component V_{il} represents the "limit velocity" or final rise velocity of each single bubble, and can be calculated by means of:

$$V_{li} = \sqrt{\frac{4gd_i\left(\rho - \rho_g\right)}{3C_D\rho}} \tag{4.2.9}$$

It must be noticed that equation (4.2.9) is implicit in the quantity V_{il}, since it is involved in the calculation of the drag coefficient which, as noted inside the paragraph 2.2.1.1, depends on the shape of the object under consideration and on its Reynolds number (the bubbles are considered to be spherical). Thus, the determination of bubble rise velocity occurs iteratively, using as a first velocity attempt the expression derived from the assumption that, at first approximation, the drag coefficient can be expressed by means of the Stokes relation (equation (2.2.4)), resulting in:

$$V_{li} = \frac{gd_i^2\left(\rho - \rho_g\right)}{18\mu} \tag{4.2.10}$$

where μ, represent the dynamic viscosity of the liquid phase.

Then, the calculation is repeated until the convergence criterion is satisfied, considering for the calculation of the drag coefficient the relation given in (2.2.5).

Hence, the relative velocity between the bubble and the fluid due to buoyancy effects has been determined. It has to be noticed that this velocity component acts only along the vertical (z) direction.

4.2.2.3 Bubble velocity due to turbulent random effects

The last contribution to the bubble velocity has been conceived in order to consider a potential deviation of the bubble from its trajectory owed to the turbulent features of the liquid flow field. For this reason a probabilistic (or "random walk") approach has been adopted.

The following procedure of calculation is implemented:

– the probability to have a turbulent fluctuation (p_{turb}) is calculated considering:

$$p_{turb} = \min\left(\frac{\Delta t}{\tau_t};1\right) \tag{4.2.11}$$

where τ_t represents the Kolmogorov time scale related to the macroscale of turbulence (hence the implicit assumption of isotropic turbulence is adopted). The value of τ_t is calculated on the basis of the turbulent characteristics of the flow field at the particle position, by means of the relation:

$$\tau_t = \frac{l}{\sqrt{k_i}} \tag{4.2.12}$$

where l represents the turbulent macroscale length and k_i is the turbulent kinetic energy of the particle calculated as described within paragraph 4.2.2.1.

The probability that an eddy causes a departure of the particle velocity from the mean flow convection velocity is then equal to 1 if Δt is higher than τ_t, otherwise, it is equal to $p_{turb} < 1$; in the numerical procedure, occurrence of the turbulence effect is considered if a number obtained from a uniform random distribution R_1 is less than p_{turb} ;

– if the above condition is satisfied another uniformly distributed random number between 0 and 1, R_2, is generated. This last is then used to obtain the velocity value, estimated as the correspondent value on the cumulative function calculated considering turbulent velocity fluctuations to be defined by a Gaussian distribution with standard deviation equal to $\sqrt{2/3k_i}$. In particular, the three components of the fluctuating velocity

are calculated by means of three different random samplings from the probability distribution. Finally, the turbulent fluctuation of the particle velocity V_{ti} is assigned as a property of each bubble.

- if R_1 is greater than the probability to have a turbulent fluctuation, the time scale of turbulence (just calculated) is used to compute the path of the bubble inside the turbulent eddy as the product of τ_t times the turbulent fluctuation velocity held by the bubble. If the product is greater than 1 V_{ti} is set to zero (until it reaches another position where turbulence fluctuations may occurs) otherwise it is maintained unchanged as that calculated at the previous step of the calculation.

4.2.3 Bubble trajectory

Once the velocity of each bubble has been calculated, the bubble position is determined using a predictor-corrector method (McCormack method) in order to calculate the displacement of the bubble.

In particular, the first rough estimate of the position of the bubble is calculated by applying an explicit method (predictor step), as follows:

$$\overline{r_i^{t+1}} = r_i^t + \Delta t V_i^t \tag{4.2.13}$$

where the continuous line above the position vector of the *i-th* bubble r_i indicates the first estimate; superscripts t and $t+1$ refer to the time discretization. The velocity used to provide this calculation doesn't take into account the random-walk velocity term V_{ti}, but it is simply the sum of the velocity owned by the bubble as a consequence of its position inside the computational domain (V_{fi}) and of its vertical velocity component derived from the hydrodynamic force balance (V_{li}).

The second step uses the position just calculated to evaluate the velocity $\overline{V_i^{t+1}}$ of the bubble in this new position. Also the other fluid properties (turbulent kinetic energy and turbulent kinetic energy dissipation) are evaluated at the new position following the relation (4.2.5).

Now the mean value of the two velocities is considered in order to evaluate the final position of the particle and the random walk contribution V_{ti} is added to the mean value. So the final position of the particle is considered to be the result of:

$$r_i^{t+1} = r_i^t + \Delta t\left(0.5\left(V_i^t + \overline{V_i^{t+1}}\right) + V_{ti}^t\right) \tag{4.2.14}$$

4.2.3.1 Evaluation of the effects related to the added mass force term

The trajectory followed by a spherical particle has been evaluated in order to assess the error introduced by neglecting the added mass force contribution. With this aim, the trajectory of a bubble having a fixed velocity component along x direction and a z velocity component dependent on the hydrodynamic force balance derived from equation (4.2.8) but including the added mass force contribution (equation (2.2.6)) has been evaluated, obtaining the following equation:

$$\frac{\pi d_i^2}{8}\rho C_D\left(V_{iz}\right)^2 = \frac{\pi d_i^3}{6}g\left(\rho - \rho_g\right) + C_{AM}\frac{\pi d_i^3}{6}\rho a' \tag{4.2.15}$$

where V_{iz} represents the rise velocity of the bubble and a' is the velocity of the bubble related to the added mass force. Rewriting equation (4.2.15) in terms of the overall bubble acceleration, one obtains:

$$\frac{\pi d_i^2}{8}\rho C_D\left(V_{iz}\right)^2 = (m_B + m_{AM})a \tag{4.2.16}$$

where m_B is the mass of the bubble associated with the buoyancy force, m_{AM} is the virtual mass of the bubble and a is its overall acceleration.

An initial horizontal velocity has been assigned to a bubble of mean diameter equal to 0.002 m, in order to mimic the situation encountered when it is injected inside the system. The value of the x component of velocity V_{ix} has been set equal to 5 m/s which is lower than the real velocity considered during the simulation, in order to evaluate a more critical situation.

The overall acceleration of the bubble was obtained from equation (4.2.16) and, assigning an adequate discretization time step Δt, the rise velocity of the bubble along z direction at time t was incremented according to the equation:

$$V_{iz}^{t+1} = V_{iz}^{t} + \Delta t a \tag{4.2.17}$$

where the apex t denotes the reference time. Then the position reached by the bubble was calculated trough:

$$\begin{aligned} x^{t+1} &= x^t + \Delta t V_{ix} \\ z^{t+1} &= z^t + 0.5\left(V_{iz}^{t+1} + V_{iz}^{t}\right) \end{aligned} \tag{4.2.18}$$

To evaluate the error due to neglecting the added mass term, the position taken by the bubble, obtained following the abovementioned procedure, was compared: 1) with the trajectory obtained by considering only the bubble limit rise velocity calculated through equation (4.2.9), and 2) with the limit trajectories that can be followed by a bubble whose velocity experiences turbulent fluctuations, equal to the 2% of the initial bubble velocity. The results are shown in Figure 4.2.

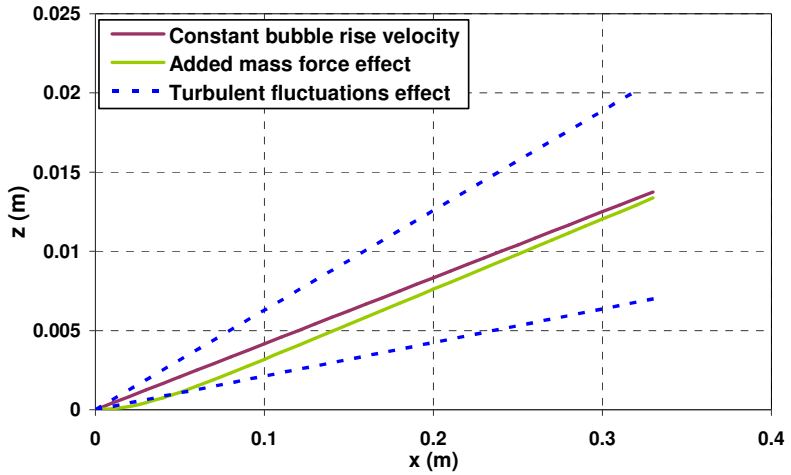

Figure 4.2 Evaluation of the added mass term effect on the bubble trajectory

It can be noticed that the limit trajectories that can be followed by the bubble when turbulent fluctuations are present envelope the trajectory followed by the bubble either considering or neglecting the added mass term. This means that the uncertainty introduced by the turbulent fluctuations of the velocity overcomes largely the possible inaccuracy that derives from neglecting the added mass term in the hydrodynamic force balance equation. Moreover, it can be noted that the bubble trajectory obtained considering a constant bubble rise velocity and the bubble trajectory calculated introducing the added mass term are very close to each other.
For this reason, the accuracy of the method implemented to calculate the bubble trajectory has been considered satisfactory for the proposed purposes.

4.2.4 Boundary conditions

Another aspect that has to be considered is that the bubble can move freely inside the computational domain except when its position reaches the

boundaries that limit the computational grid. Three types of situation can happen:

- the bubble reaches the free surface;
- the bubble reaches the outlet section;
- the bubble impacts with a solid boundary (i.e. the walls of the tank).

The outflow section of the model is considered to be the same as the liquid flow outflow section (as defined during the finite volume simulation of the liquid flow).

The first two boundary conditions are responsible for limiting the maximum number of bubbles contained within the domain of calculation. In fact, when a bubble reaches the free surface or the outlet section is "immobilized", thus, it is no more considered as an active particle in the system, and then it can no more affect the changes of the dissolved oxygen concentration. The last condition implies that a bubble cannot overcome the solid wall of the tank (bottom and side walls). So when the threshold identifying the boundary is crossed the position of the bubble is corrected and brought back to a position calculated with the hypothesis of perfectly elastic reflection.

This condition is applied also when a partitioning wall is placed inside the computational domain.

4.3 Modelling the evolution of the concentration of a dissolved species

4.3.1 Balance equation of a dissolved species

The evolution of the concentration of a dissolved species has been evaluated considering the following balance equation:

$$\frac{\partial c}{\partial t} + V_f \cdot \nabla c = \nabla \cdot (\nu_t + D_m)\nabla c + S \tag{4.3.1}$$

Considering equation (4.3.1) the first term on the left hand side represents the local time derivative of the concentration of the generic dissolved species c, while the second is the convective term (V_f is the fluid velocity). Considering the right hand side, the first term represents the diffusive term where the diffusion coefficient ($\nu_t + D_m$) is the result of the sum of the turbulent kinetic viscosity of the liquid phase, ν_t, and of the molecular diffusion coefficient of the species c into the liquid, D_m. The turbulent kinetic viscosity has been assumed to coincide with the turbulent diffusion coefficient $D_{TM} = \nu_t/Sc_t$, i.e. the turbulent Schmidt number Sc_t, for the turbulent diffusion of the species has been assumed equal to 1.The last term on the right hand side of the equation, S, is the concentration source (or sink) that occurs as a result of mass transfer (e.g. when the oxygen inside bubbles passes from gaseous to dissolved oxygen into the liquid phase and / or vice versa) or of consumption or growth kinetics when different species are involved (e.g. for heterotrophic biomass and substrate).

4.3.2 Numerical solution of the mass balance equation

A discrete formulation of the partial differential equation (4.3.1) has to be considered to evaluate the concentration changes within each cell of the computational grid.

When a time discretization is adopted, equation (4.3.1) can be rewritten as:

$$\Delta c = \Delta t(-C + D + S) \tag{4.3.2}$$

where Δc is the discrete variation of the dissolved species concentration occurred during the time step Δt as a consequence of the contribution of the convective (C), diffusive term (D) and source terms (S) which derive from the discretization of the corresponding terms of equation (4.3.1).

Within the next paragraphs the methodology used to discretize the flow field and to model each of these terms will be analysed.

4.3.2.1 Space discretization

Numerical solution of equation (4.3.1) needs first the definition of a computational grid has been defined for the calculation of the concentrations of the dissolved species. Owing to the geometrical simplicity of the studied cases, a cartesian staggered grid has been defined, where the scalar quantities are defined at the cell centre (concentration, turbulent kinetic energy, dissipation of the turbulent kinetic energy) while the components of the vector variable (velocity) are defined at the middle of the cell face whose normal is aligned with the component itself.

The grid for the computation of concentration can be defined arbitrarily and its dimension may not coincide with the dimension of the grid used for the calculation of the position (and velocity) of the bubbles.

The procedure to interpolate flow values on this second computational grid is analogous to the one described in paragraph 4.2.2.1. Once the position of the centre of the cell is defined for each computational cell of the grid, the corresponding position with respect to the cartesian grid derived from the finite volume simulation of the liquid flow is calculated. Then, a weighted mean is considered in order to interpolate the scalar and vector quantities starting from the known vertex values of the cartesian grid used for the bubbles.

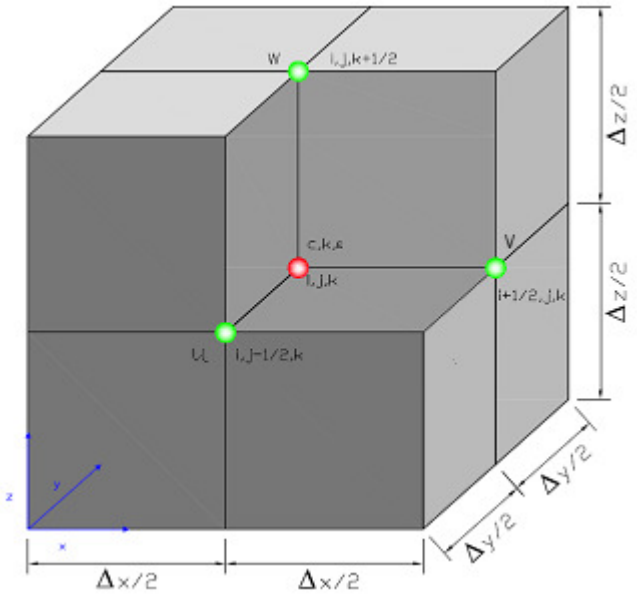

Figure 4.3 Staggered grid for the computation of the concentrations (red point = cell centre; green point = middle point of the face of the cell)

4.3.2.2 Discretization of the convective term

The convective term in equation (4.3.1) is the scalar product of the velocity times the concentration gradient, where the concentration gradient is defined as:

$$\nabla c = \frac{\partial c}{\partial x} + \frac{\partial c}{\partial y} + \frac{\partial c}{\partial z} \tag{4.3.3}$$

The discretization of the convective term has been carried out by means of a second-order upwind finite difference scheme.

In particular, for each velocity component the *i*-cell value is calculated as an average of the values at *i-1/2* and *i+1/2* cell faces to asses flow direction. Then a one-sided 2^{nd} order difference is applied to concentration derivatives,

depending on the sign of the mean value of the velocity. The method applied for the *x* component leads to the following formulation:

$$u_i = 0.5\left(u_{i-\frac{1}{2}} + u_{i+\frac{1}{2}} \right)$$

$$C_{xi} = u_{i-\frac{1}{2}} \left(\frac{3c_i - 4c_{i-1} + c_{i-2}}{2\Delta x} \right) \text{ if } u_i \geq 0 \tag{4.3.4}$$

$$C_{xi} = u_{i+\frac{1}{2}} \left(\frac{-3c_i + 4c_{i+1} + c_{i+2}}{2\Delta x} \right) \text{ if } u_i < 0 \tag{4.3.5}$$

The convective term for each computation cell C_i is then calculated as the sum of the contributions calculated for each direction as:

$$C_i = C_{xi} + C_{yi} + C_{zi} \tag{4.3.6}$$

4.3.2.3 Discretization of the diffusive term

The diffusive term in equation (4.3.1) is the divergence of the product of the global coefficient times the gradient of the concentration.

The global diffusion coefficient is intended as the sum of the molecular and the turbulent diffusivity

The discretization of the diffusive term is carried out by means of a central difference. Considering the *x* contribution we get:

$$D_{xi} = \frac{\left(2D_m + \nu_{t_i} + \nu_{t_{i+1}}\right)\left(c_{i+1} - c_i\right) - \left(2D_m + \nu_{t_i} + \nu_{t_{i-1}}\right)\left(c_i - c_{i-1}\right)}{2\Delta x^2} \tag{4.3.7}$$

with:

$$\nu_{t_i} = c_\mu \frac{k_i^2}{\varepsilon_i} \tag{4.3.8}$$

where:

$c_\mu = 0.09$;

k_i is the turbulent kinetic energy of the *i-th* cell;

ε_i is the turbulence dissipation rate of the *i-th* cell;

D_{xi} is the contribution to the diffusive term along *x* direction of the *i-th* cell;

D_m is the molecular diffusion coefficient.

The diffusive term for each computation cell is then calculated as the sum of the diffusive term calculated for each direction as:

$$D_i = D_{xi} + D_{yi} + D_{zi} \tag{4.3.9}$$

4.3.2.4 Source term calculation

The source term is representative of the changes of the concentration field due to mass transfer phenomena for oxygen and of the changes owed to the production/consumption kinetics for dissolved oxygen, heterotrophic biomass and substrate.

4.3.2.4.1 Mass transfer from the gas bubbles to the liquid volume

The mass transfer phenomena are evaluated by means of a relation based on equation (2.1.3). In particular, the concentration flow rate transferred between the two phases is estimated by considering the concentration gradient of the two involved phases ($c_g - c_l$), multiplied by the specific area a and by the mass transfer coefficient k_l. The specific area is evaluated as the ratio between the area of the surface across which mass transfer takes place, A_g, and the exchange

volume that has been considered to be equal to the liquid phase contained inside each computational cell ($W - W_g$). The relation for each computational cell is:

$$S_i = \frac{1}{(W_i - W_{gj})} \sum_{j=1}^{N} k_l A_{gj} \left(c_{g_{ij}} - c_{l\,i} \right) \tag{4.3.10}$$

where:

S_i is the source term due to the mass transfer from bubble j to cell i (kg/(m³ s));

W_i is the volume of the computational cell (m³);

W_{gj} is the volume of gas contained inside the computational cell (m³), computed from the number of estimated bubbles inside the cell;

N is the total number of bubble inside the computational cell;

c_{gij} is the concentration of the gaseous phase (oxygen) considered in equilibrium condition with the partial pressure of gas (kg/m³);

c_{li} is the concentration of the dissolved oxygen into the liquid within the computational cell i (kg/m³);

A_{gj} is the total exchange area associated with the computational bubble j inside cell i.

Moreover:

$$W_{gj} = \sum_{j=1}^{N} n_j \frac{\pi d_j^3}{6} \text{ and } A_{gj} = n_j \pi d_j^2 \tag{4.3.11}$$

where n_j is the number of the real injected bubbles of diameter d_j associated with the computational bubble j.

It seems necessary to highlight the fact that the mass transfer models adopted are formally different depending on whether the transfer is considered from the bubble to the liquid phase or the exchange that takes place through the free

surface between the atmosphere and the liquid volume. In the former case the source term can be considered effectively as such, since the exchange allows for an increase of concentration of dissolved oxygen content in the tank. In the second case it would be more appropriate to deal with a sink, since the exchange through the surface involves a supersaturated fluid volume. The exchange of mass due to the oxygen transfer from the bubble to the liquid has been calculated for each time step of calculation once the final position taken by the bubbles has been determined (as described in the paragraph 4.2.3).

The reference concentration c_{gij}, which determines the mass transfer from the bubble *j* contained in cell *i* to the liquid, is:

$$c_{gij} = k_H \left(p_i + p_j \right) \tag{4.3.12}$$

where:

k_H = Henry's coefficient (g/(l·Pa)) as defined inside equation (2.1.1);

p_{ps} = hydrostatic pressure in cell *i* (Pa);

p_j= internal pressure of the bubble *j* (Pa).

In equation (4.3.12) the hydrostatic pressure is evaluated by adding to the atmospheric pressure the product of the drought (evaluated considering the bubble position) for the specific weight of the liquid phase, whereas the internal pressure is evaluated considering the surface tension of the bubble by means of relation:

$$p_j = \frac{4\tau}{d_j} \tag{4.3.13}$$

where τ is the surface tension of the bubble.

Another condition that has been considered is the decrease of the bubble diameter due to the oxygen transfer to water. So, for each computational bubble the diameter of each bubble is determined through the relation:

$$d'_j = \left[\frac{6}{\pi} \left(\frac{\pi}{6} d_j^3 - \frac{q_j \Delta t}{\rho_g n_j} \right) \right]^{1/3} \tag{4.3.14}$$

where:

d'_j is the new bubble diameter (m);

q_j is the mass flow rate transferred from the set of bubble of the considered dimensional class (m³/s);

n_j is the number of bubbles of the considered dimensional class.

After the new diameter has been calculated properties such as superficial area and internal pressure are updated for each bubble.

The mass transfer coefficient from the gas bubble to the liquid phase has been evaluated by different models, on the basis of theories explained in Chapter 2 and a sensitivity analysis on these models has been conducted (see Chapter 7).

4.3.2.4.2 Mass transfer from the liquid volume to the surrounding atmosphere

Finally, the mass transfer at the free surface c_{gs} is calculated by taking into account the saturation concentration of the gaseous phase at atmospheric conditions:

$$c_{gs} = k_H p_{atm} P_{O_2} \tag{4.3.15}$$

where P_{O2} indicates the volume percentage of oxygen in atmosphere.

The modelling of the mass transfer coefficient at the surface is instead based on the two-film theory: a global mass transfer coefficient $k_l a$ has been evaluated experimentally during deoxygenation tests. In fact, for the desorption of a gaseous species from a liquid phase, the equation (2.1.13) can be rewritten as:

$$\frac{dc_l}{dt} = -k_L a(c_{lt} - c_{gs}) \tag{4.3.16}$$

where c_l is the concentration of the dissolved species inside the liquid volume.

In order to evaluate the overall mass transfer coefficient $k_l a$, the equation (4.3.15) can be integrated from the initial reference time $t=0$ (when the desorption is considered to start) to a generic time instant t, leading to:

$$k_l a = -\ln\left(\frac{c_{lt} - c_{gs}}{c_{lo} - c_{gs}}\right) \tag{4.3.17}$$

Using equation (4.3.17), the $k_l a$ values have been determined for each instant of the deoxigention test at the monitoring locations inside the liquid volume. The final unique $k_l a$ value has then been calculated averaging on time and on space. Finally, the mass transfer coefficient k_l has been calculated by considering the specific surface a as the ratio of the free surface area exposed to the transfer to the total volume of the compartment.

The mass transfer coefficient thus calculated has been used exclusively to model the concentration changes that involve the top layer of the cells of the mesh for concentrations. Accordingly to equation (4.3.10) the source term for each cell in the top layer involving dissolved oxygen is thus evaluated as:

$$S_i = \frac{1}{(W_i - W_{gj})} k_l \Delta x \Delta y (c_{gs} - c_{li}) \tag{4.3.18}$$

4.3.2.4.3 Biomass, substrate and dissolved oxygen kinetics

Concerning the evolution of the concentrations of dissolved oxygen, heterotrophic biomass and readily biodegradable substrate due to the biological

kinetics, the respective source terms are modelled by means of the kinetics relations previously described inside Chapter 3.

In particular, a double Monod kinetic model has been implemented taking into account the correction factor described in equation (3.2.7), leading to the source term equations for each computational cell *i*:

$$S_{xi} = K_m \frac{c_{Si}}{K_S + c_{Si}} \frac{c_{DOi}}{K_{DO} + c_{DOi}} c_{xi} \tag{4.3.19}$$

$$S_{Si} = \alpha K_m \frac{c_{Si}}{K_S + c_{Si}} \frac{c_{DOi}}{K_{DO} + c_{DOi}} c_{xi} \tag{4.3.20}$$

$$S_{DOi} = -\beta K_m \frac{c_{Si}}{K_S + c_{Si}} \frac{c_{DOi}}{K_{DO} + c_{DOi}} c_{xi} \tag{4.3.21}$$

where the subscripts x, S and DO stand for biomass, substrate and dissolved oxygen respectively and α, β, K_m, K_s and K_{DO} are the parameters of the model determined as described in paragraph 6.3.

4.3.2.5 Time step calculation

The integration of the mass balance equation of the dissolved species needs the calculation of the maximum time step that fulfils stability conditions.

Actually, equation (4.3.1) is of hyperbolic-parabolic type and its hyperbolic part., coincident with its convective term, needs a stability condition if an explicit numerical scheme is adopted to solve the equation. This means that the numerical time step cannot be independent from the space discretization to ensure the numerical stability. This condition is the Courant condition and is imposed by considering an appropriate CFL number (Courant- Frederick-Levy):

$$CFL = \frac{|V|\Delta t}{\Delta s} \tag{4.3.22}$$

To ensure stability, the CFL number must be everywhere less than 1. The calculation of the time step is made by considering the different velocity values of the computational domain. Once the maximum length of the edge of the computational cell of the concentration grid is determined Δs, the calculation of the velocity module for the whole domain of computation is considered by taking the average value of each velocity component for each cell (velocities for a staggered grid are defined at the middle point of the faces of the cell). Consequently, imposing an appropriate CFL number the related time step derives from equation (4.3.22) by considering the maximum module of velocity calculated as just described.

Similarly a stability condition exists also for the diffusive term:

$$\frac{\nu_t \Delta t}{\Delta s^2} < 1 \tag{4.3.23}$$

Finally, the definitive time step can be calculated as:

$$\Delta t = \min\left(\frac{\Delta s CFL}{|V|}; \frac{\Delta s^2 C}{\nu_t}; \Delta t_{\max} \right) \tag{4.3.24}$$

where Δt_{max} is the initial time step imposed as a requested parameter and C is the number considered in order to ensure the stability of the diffusive term.

The possibility to consider two different time steps for different portions of the computational domain is taken into account. This possibility has been considered in order to avoid that a too small time step could affect the integration time of the whole computational domain.

4.3.3 Initial and boundary conditions for concentrations

The initial conditions represent a crucial point for the evolution of the phenomena (e.g. they a strategic role for the determination of the driving force for the mass transfer) so, initial value has to be assigned to the computational grid for each dissolved species. In particular, the initial condition of saturation concentration at the atmospheric pressure (equation (4.3.15)) can be used for dissolved oxygen.

Moreover, different initial values of concentration can be set for the calculation. This condition is modelled by imposing a mean value for concentration within a confidence interval and calculating for each cell a uniformly distributed random value around the mean value.

The numerical method applied requires the assignment of boundary conditions for the computational domain. In particular, since the convective term of the balance equation (4.3.1) is discretized using a second order upwind method, it is necessary to assign values to concentrations beyond the domain for an additional two layer of cells on each boundary of the computational domain. On each wall of the domain Von Neumann conditions have been imposed (zero concentration gradient): the same concentration of the extreme cells of the computation domain has been imposed to the cells beyond the boundaries.

At the inflow boundary a concentration needs to be assigned as a Dirichlet condition. In order to allow for the recirculation of the fluid volume that is performed by the system adopted, a mean value of the concentration at the outlet has been calculated and assigned at the inlet.

Chapter 5

Inputs data for the Eulerian–Lagrangian model: liquid flow field and BSD determination

In Chapter 4 the numerical approach and the structure of the numerical model for the prediction of the evolution of species concentration was presented. It was highlighted how the basic inputs of the model (in addition to the necessary physical parameters) are the liquid velocity flow and the size distribution (BSD) of the bubbles injected in the system.

Inside this chapter the numerical and the experimental techniques used to obtain these data are briefly outlined.

5.1 Finite-volume flow simulations

The liquid velocity flow was determined considering the flow to be steady and incompressible. Under these assumptions, the velocity field simulation was obtained with the CFD code CD-Adapco STAR-CD v3.26, which uses the finite-volume (FV) method to solve the RANS (Reynolds Averaged Navier-Stokes) equations. The SIMPLE (Semi Implicit method for Pressure Linked

Equations) solution procedure was adopted, together with an LUD (Linear Upwind Difference) 2nd-order differentiation scheme for convective terms.

RANS equations are analogous to the N-S equations except for the fact that they introduce an apparent stress term, which derives from the averaging operation on the main flow variables, velocity *u* and pressure *p*. In particular, starting from the tensorial formulation of the N-S equations:

$$\frac{\partial u_i}{\partial t} + u_j \frac{\partial u_i}{\partial x_j} = -\frac{1}{\rho}\frac{\partial p}{\partial x_i} + \frac{\partial}{\partial x_j} + \left[\nu \left(\frac{\partial u_i}{\partial x_j} + \frac{\partial u_j}{\partial x_i} \right) \right] \tag{5.1.1}$$

and introducing the relation:

$$\begin{aligned} u_i(x_k,t) &= U_i(x_k) + u_i'(x_k,t) \\ p(x_k,t) &= P(x_k) + p'(x_k,t) \end{aligned} \tag{5.1.2}$$

considering that:

$$\begin{aligned} U_i(x_k) &= \lim_{T\to\infty} \frac{1}{T} \int_0^T u_i(x_k,t) = \overline{u_i(x_k,t)} \\ P(x_k) &= \lim_{T\to\infty} \frac{1}{T} \int_0^T p(x_k,t) = \overline{p(x_k,t)} \end{aligned} \tag{5.1.3}$$

substituting equation (5.1.2) inside equation (5.1.1) and time-averaging, the final RANS equations assume the form:

$$\frac{\partial U_i}{\partial t} + U_j \frac{\partial U_i}{\partial x_j} = -\frac{1}{\rho}\frac{\partial P}{\partial x_i} + \frac{\partial}{\partial x_j}\left[\nu\left(\frac{\partial U_i}{\partial x_j} + \frac{\partial U_j}{\partial x_i}\right)\right] + \\ -\frac{\partial}{\partial x_j}\overline{u_i' u_j'} \tag{5.1.4}$$

where the last right hand side term of equation (5.1.4) is the spatial derivative of the above-quoted apparent stress term, which takes into account the turbulent effects.

Introducing the Boussinesq hypothesis, which relates the turbulent stresses with the rate of strain tensor S_{ij}, through the eddy viscosity ν_t:

$$\overline{-u_i' u_j'} = 2\nu_T S_{ij} \quad \text{where } S_{ij} = \frac{1}{2}\left(\frac{\partial U_i}{\partial x_j} + \frac{\partial U_j}{\partial x_i}\right) \tag{5.1.5}$$

substituting inside equation (5.1.4) the RANS equations are finally:

$$\frac{\partial U_i}{\partial t} + U_j \frac{\partial U_i}{\partial x_j} = -\frac{1}{\rho}\frac{\partial P}{\partial x_i} + \frac{\partial}{\partial x_j}\left[(\nu + \nu_T)\left(\frac{\partial U_i}{\partial x_j} + \frac{\partial U_j}{\partial x_i}\right)\right] \tag{5.1.6}$$

Several models have been proposed to represent and relate the eddy viscosity term to the fluid patterns and properties (e.g. algebraic model, one equation model, two-equation model, etc.).

The determination of the liquid velocity field as input for the E-L numerical model has been carried out by testing two types of two-equations turbulence models: the standard k-ε and the k-ε RNG (ReNormalization Group) turbulence model.

In paragraph 6.2 the efficiency of the eulerian part of the E-L model has been tested by evaluating the capacity to simulate the concentration field of a

passive scalar transported by a turbulent jet discharging in a co-flow stream. In that section a sensitivity analysis has been conducted on the parameters of the *k-ε* standard model. For this reason the complete description of the equations that lead to the modelling of the turbulent effect inside RANS equations is proposed only for the standard *k-ε* turbulence model.

The *k-ε* RNG turbulence model demonstrated instead the best agreement with laboratory experimental data considered in Chapter 7, confirming the results of Jayanti (2001) on the hydrodynamics of jet mixing in vessels.

5.1.1 Standard *k-ε* model equations

Like every two-equation turbulence models, the standard *k-ε* model (Launder and Spalding, 1984) assumes two independent relations to represent the velocity and the length scales from which the eddy viscosity is considered to depend. Consequently, the modelling of the eddy viscosity is proposed as:

$$\nu_T = c_\mu \frac{k^2}{\varepsilon} \tag{5.1.7}$$

In particular, the turbulent kinetic energy k is considered as the turbulence intensity marker of the velocity field and it is defined by:

$$k = \frac{1}{2} \overline{u_i' \, u_i'} \tag{5.1.8}$$

while, the turbulence dissipation rate ε is assumed as:

$$\varepsilon = \nu \overline{\left(\frac{\partial u_i'}{\partial x_j} \right)^2} \tag{5.1.9}$$

and c_μ is a constant of the model (see Table 5.1).

The equation for the kinetic energy is directly derived from the manipulation of the RANS and N-S equations, which leads to the relation for k:

$$\frac{\partial k}{\partial t} + U_j \frac{\partial k}{\partial x_j} = -\overline{u_i' u_j'} \frac{\partial U_i}{\partial xj} - \frac{\partial}{\partial x_j}\left(\frac{\overline{u_i' p'}}{\rho} \delta_{ij} + \frac{1}{2} \overline{u_i'^2 u_j'} \right) + \\ + \frac{\partial}{\partial x_j} \nu \frac{\partial k}{\partial x_j} - \varepsilon \tag{5.1.10}$$

where:

- the first term of the right hand side of equation (5.1.10) represent the turbulent kinetic energy *production* due to the effects of the Reynolds stresses on the velocity gradient of the time-averaged flow motion. The Boussinesq hypothesis is introduced to solve it;
- the second term of the right hand side of equation (5.1.10) takes into account the transport of the turbulent kinetic energy due to the turbulent fluctuations (*turbulent diffusion*) similarly modelled considering Boussinesq hypothesis;
- the third term of the right hand side of equation (5.1.10) represents the *viscous diffusion*.

The turbulent diffusion is modelled by means of an equation which takes the same formal expression of the viscous diffusion by introducing the turbulent Prandtl number σ_k. Rewriting, the equation (5.1.10) becomes:

$$\frac{\partial k}{\partial t} + U_j \frac{\partial k}{\partial x_j} = \nu_T \frac{\partial U_i}{\partial xj}\left(\frac{\partial U_i}{\partial x_j} + \frac{\partial Uj}{\partial x_i} \right) + \frac{\partial}{\partial x_j}\left[\left(\nu + \frac{\nu_t}{\sigma_k} \right) \frac{\partial k}{\partial x_j} \right] - \varepsilon \tag{5.1.11}$$

The ε equation can be obtained from the N-S equations but it contains several undetermined quantities; it is therefore derived "mimicking" the *k* equation, as:

$$\frac{\partial \varepsilon}{\partial t} + U_j \frac{\partial \varepsilon}{\partial x_j} = c_{\varepsilon 1} \nu_T \frac{\varepsilon}{k} \frac{\partial U_i}{\partial xj} \left(\frac{\partial U_i}{\partial x_j} + \frac{\partial Uj}{\partial x_i} \right) + \\ + \frac{\partial}{\partial x_j} \left[\left(\nu + \frac{\nu_t}{\sigma_\varepsilon} \right) \frac{\partial \varepsilon}{\partial x_j} \right] - c_{\varepsilon 2} \frac{\varepsilon^2}{k} \tag{5.1.12}$$

where, similarly, the first term on the right hand side represents the *production* of the turbulence dissipation rate, the second term takes into account the *viscous and turbulent diffusion* of ε, while the last term represents a *sink* term of the turbulence dissipation rate which must tend to infinity when k tends to zero.
Three other constants (i.e. σ_ε, $c_{\varepsilon 1}$ and $c_{\varepsilon 2}$) are introduced by the ε equation.
The values of the five main constants of the standard k-ε model are listed in Table 5.1.

c_μ	σ_k	σ_ε	$c_{\varepsilon 1}$	$c_{\varepsilon 2}$	κ^*
0.09	1.0	1.22	1.44	1.92	0.419

Table 5.1 Values of the constants of the standard k-ε turbulence model (k^* = von Kàrman constant)

5.2 Experimental velocity measurements

The numerical results were validated by means of experimental measurements of the velocity field, obtained through a 3D Acoustic Doppler Velocimeter (ADV - Nortek 10 MHz Velocimeter), which measures simultaneously the three velocity components.

The work principle of ADV probe exploits the frequency shift between the transmit pulse and the received echo. The frequency of the reflected signal is modified by the presence of impurities and scatters within the sampling volume (and carried by the flow) so the difference between the emitted and received frequency is proportional to the liquid velocity. The device samples the

reflected signal at a frequency of 25Hz, within a sampling volume (having a height varying from 3 to 9 mm) located about 5 cm below the emitting probe, as depicted in Figure 5.1.

The main outputs of the ADV measurement device are the velocity components, the Sound to Noise Ratio (SNR) and the Correlation data. The raw data have been considered to evaluate the signal quality, to calculate the mean value of the velocity and to estimate the turbulent kinetic energy of the flow at the measurement positions.

The SNR parameter is a measure of the signal strength, which has to be high enough to limit the noise effects. For this reason the value is considered as a quality indicator of the measured data, and the measures are considered reliable if the SNR value is above 10-15 dB.

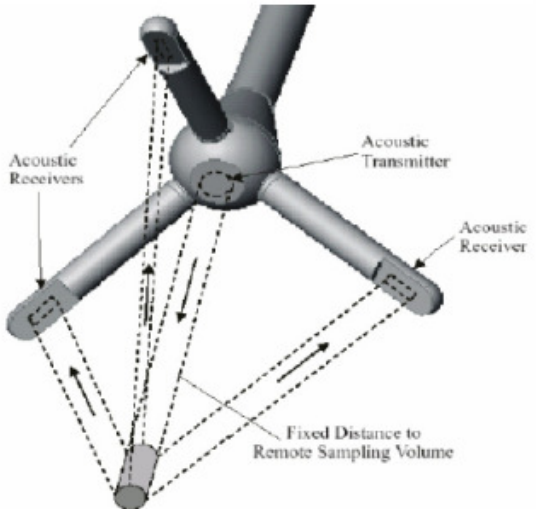

Figure 5.1 ADV measurement probe: localisation of the sampling volume

The correlation is also considered a quality indicator of the signal as it provides the estimation of the auto-variation of the signal received by each

beam. The producer recommended value that has to be respected is of 70%, if the value is lower the velocity measure may be affected by errors.

The quality of the signal can be improved by increasing the strength of the received signal by adding a seeding material (fine scatters) which increases the amount of micro-particles contained within the sampling volume. By doing so, only the SNR parameter is improved but no other operational solution can be adopted for the correction of poor correlation values. Moreover, low correlation values can be induced by high fluctuations of the velocity field, so it can be difficult to separate the turbulence effects from signal disturbances which can affect the correlation value.

5.3 Signal processing of ADV data

The reliability of the mean velocity measured by ADV has been proved by many researchers, but its precision in making measurements of turbulence quantities has been often questioned. Voulgaris and Trowbridge (1998) highlighted three main sources of errors:

- sampling errors due to the analogical/digital signal conversion unit, related to the velocity range imposed but independent from the actual flow velocities;
- Doppler noise related to the backscatter system, which is related to the turbulence and particle scattering, to beam divergence and to the finite residence time of the particles in the sampling volume;
- errors due to abrupt velocity gradients (especially where a boundary layer is established). These problems suggested that the ADV velocity measurements should not be used without an adequate post-processing of data.

In particular, Nikora and Goring (1998) presented a post-processing method built to isolate and to correct the outlier values of a sample (despiking filter) which acts to reduce the Doppler noise that has been identified by Lohrmann et

al. (1994) as the first error source in turbulence measurements by ADV. Nikora and Goring's approach has been discussed by other authors, because the relation with the flow mean velocity hasn't been highlighted inside their work. Anyway, although the efforts spent to find the relation between Doppler noise and mean flow velocity, this link is not yet clear as pointed out by Khorsandi et al. (2009).

Nevertheless, the post-processing of ADV measurements seems a necessary step at least to eliminate the communication errors or the low quality data. For these reasons, the ADV velocity measurements have been post-processed by means of two different methods which will be presented herein.

5.3.1 Threshold filtering technique (filtering method A)

The first filtering technique implemented for the ADV velocity data has been performed by means of an algorithm implemented in Matlab® home-made program.

The filtering process is subdivided into three main steps:

- velocity signal check, where measurements characterized by SNR values lower than 15 dB and correlations under 70 percent are rejected;
- small disturbance removal, where local velocity values are removed considering a threshold method based on the comparison between the local velocity deviation and the standard deviation of the sample of the velocity measurements;
- low pass filtering, where a Butterworth low-pass filter is applied in order to remove high frequency effects (if there are any) and to avoid aliasing phenomena in signal reconstruction due to inobservance of the Niquist-Shannon theorem.

This technique has been developed along the lines of the method proposed by Chanson et al. (2008) even though his work regarded field velocity measurements. For this reason an adjustment to the laboratory environment has been assessed.

After each step, the mean velocity value and an estimation of the turbulent kinetic energy (evaluated by means of equation (5.3.1)) has been performed.

$$k = \frac{1}{2}\left(\sigma_x^2 + \sigma_y^2 + \sigma_z^2\right) \tag{5.3.1}$$

where, σ_x, σ_y and σ_z are the standard deviations of the x,y, and z velocity components of the measurement sample, while k is the corresponding turbulent kinetic energy .

The low-pass Butterworth filter passes the low frequency components of the signal but stops those higher than the cutoff frequency imposed. In particular, the filter is designed to provide a smooth cut of the signal, since it does not completely pass the frequency components lower than the cutoff frequency, nor completely stops those higher than the threshold. This effect can be appreciated looking at the frequency response function of the filter:

$$\left|H\left(i\Omega\right)\right|^2 = \frac{1}{1+\left(i\Omega/\Omega_c\right)^{2N}} \tag{5.3.2}$$

where:

H = frequency response function of the Butterworth filter;

Ω = signal frequency (rad/s);

Ω_c = cutoff frequency (rad/s);

N = filter order;

i = imaginary unit.

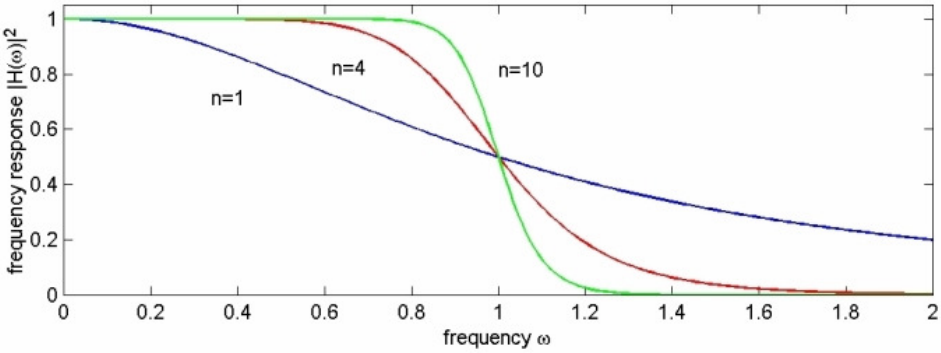

Figure 5.2 Effect of the increase of the filter order

The cutoff frequency separates the pass band and the stop band. An exemple of the effect of the filter order is shown inside Figure 5.2, where can be noticed how increasing the filter order the frequency response function becomes steeper and consequently also the transition from the pass band to the stop band becomes steeper too.

5.3.2 Goring and Nikora (2002) despiking method (filtering method B)

For the second post-processing method WinADV® v2.028 free software has been used, where the Goring and Nikora (2002) phase space threshold method is implemented. The method provides the detection of outlier values of each measurement sample (spikes) by means of a technique that doesn't require any user-defined parameter (universal threshold) but the estimation of the threshold necessary to the detection of nasty values is provided by the estimation of statistical parameter of the sample. Their method is based on the concept of the three-dimensional phase space plot where the variable (each velocity component) and its derivatives are plotted against each other. The evaluated threshold is then used to define the minor and the major axis of an ellipsoid outside of which lie the spikes (Figure 5.3).

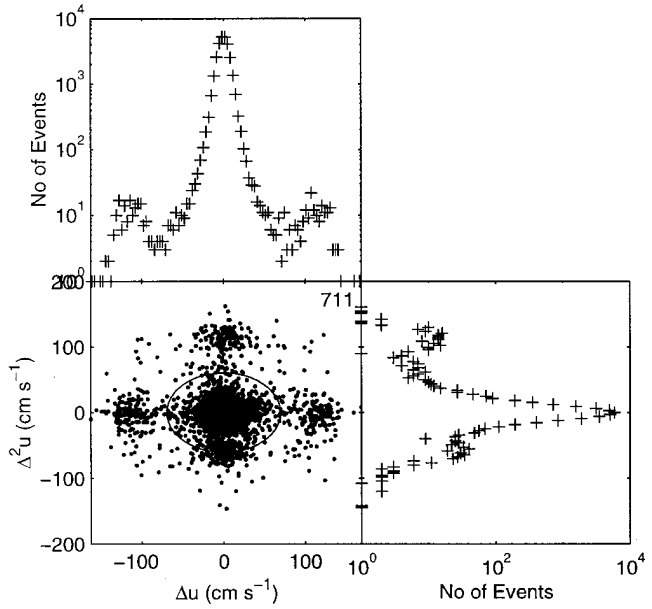

Figure 5.3 Spike detection by phase space threshold method (adapted from Goring and Nikora, 2002)

The derivatives are calculated by means of a central finite difference scheme, and the detection of spikes continues until a stationary condition is reached (zero spikes detected). After the spike is detected its value can be replaced by another value estimated by means of several techniques (extrapolation by the preceding data point or the two preceding points, overall mean of the signal, smoothed estimate, interpolation between the ends of the spike). Goring and Nikora carried out a replacement method based on the construction of a third order polynomial (built considering twelve points on each side of the detected spike) in order to perform the estimation of the missing value.

It must be highlighted as WinADV® software only detects the spikes but doesn't substitute them.

In a second phase, the method included the application of the despiking filter together with the analysis and elimination of the elements of the sample that didn't respect the quality level on SNR and correlation values (15 dB and 70% respectively).

5.4 BSD determination

The last input that has to be determined is the dimensional distribution of the bubbles that enter the system (BSD).

Within the scientific literature several methods and instruments are presented for measuring the bubble flow characteristic (BSD and bubble velocity).

A review of some of these methods is given by Billet (1985): nuclear (gamma ray, neutrons), electrical (Coulter counter), acoustical (attenuation, Doppler), optical (light scattering, photography, holography, phase detection) to whom we can add some other instruments of recent ideation (e.g. phase-detection conductivity probe, capillary suction probe).

For the present research activity an optical method has been adopted (Chigier, 1991; Laakkonen et al., 2007). In particular, the BSD near the nozzle has been obtained by using high resolution digital images (10 Mpixel) of the bubble field, by means of a Nikon D80 digital camera equipped with a Nikkor 18-135 mm objective. Two different methods have been then applied to the estimation of the final bubble size distribution.

5.4.1 Circular Hough transform for BSD determination

An image post-processing semi-automatic procedure has been implemented using the Image Toolbox included in Matlab® v7.1. Each channel of the uncompressed RGB (Red Green and Blue) images acquired were analysed in order to evaluate if one channel prevailed over another in terms of image quality, but no such difference was highlighted. Consequently the pictures were converted into grey scale images. Observing the images of he bubbly cloud it can be noticed the difficulty to distinguish between the in focus bubbles and the

background, between in focus and out of focus bubbles and between bubbles and impurities within the water. The necessity to simultaneously reduce the background noise effect and to mark the bubble edge made unsuccessful the application of several kinds of filter. For this reason a manual correction of the image contrast was performed by tuning a set of parameters for the image series. This operation put forward the best condition to the next application of the Canny's algorithm (Gonzalez et al. (2004)) for the edge detection of the bubble contours. Another observed condition was that Canny's algorithm seemed to produce better results with inverted images, so this operation was done.

Several steps are nested inside the Canny's algorithm: the application of a smoothing Gaussian filter, which acts to further reduce the image noise; the computing of the gradient magnitude of the luminance of pixels along several directions; the edge detection by means of suppression of pixels for which the calculated gradient is not maximum and through a double threshold method. After the Canny's algorithm application, the images are turned into binary images where the detected edges are cluster of white pixels. Most of the bubbles into the pictures have a circular shape, for this reason, the circular Hough transform (as described by Gonzalez et al., 2004 and Tang, 2008) was then applied to recognize the radius and the centre position of circumferences and arcs detected by Canny edge detector algorithm.

The Hough transform performs the localisation of circular shape objects by means of calculation of the probability that a certain pixel of the detected edge may lie on the chord of a circumference with a defined radius (for further explanations about the post-processing method implemented the reader is recommended to refer to Raboni (2010)). The Hough transform was implemented for the detection of circumferences with radius varying from 5 to 160 pixels with a step equal to 5 pixels.

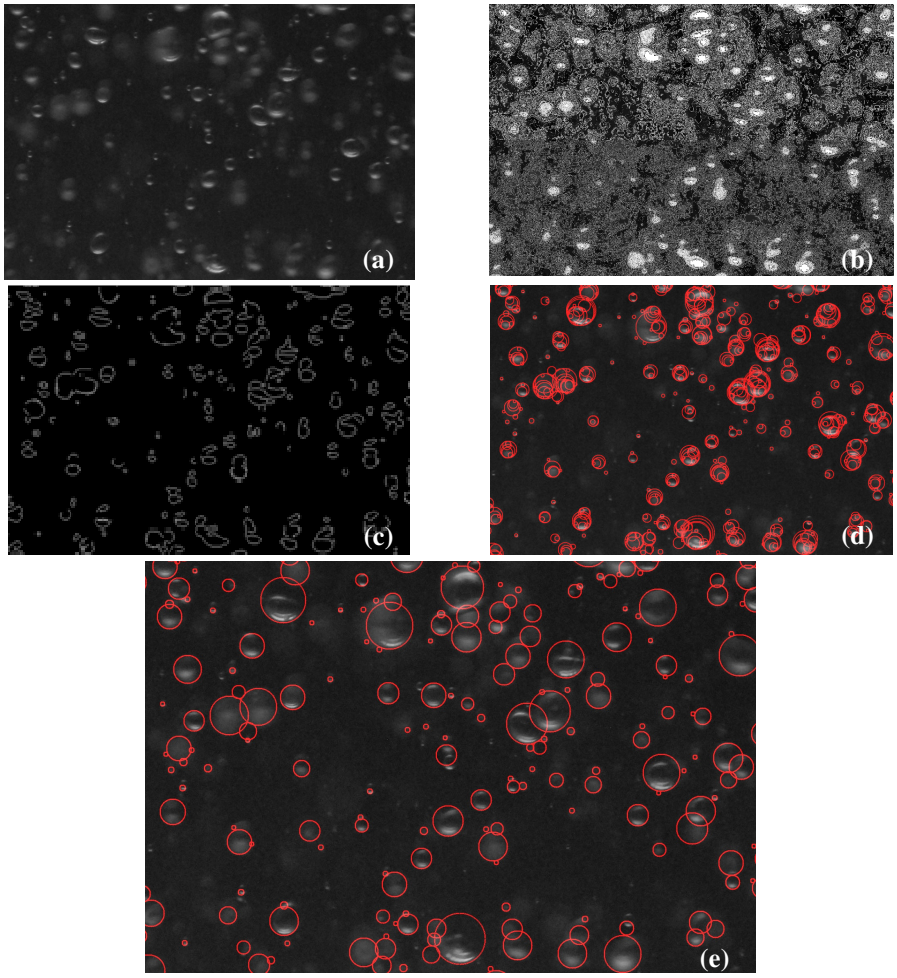

Figure 5.4 Detail of one of the images used to develop BSD: original (a), after enhancement of image contrast (b), after application of Canny's algorithm (c), after application of circular Hough transform (d) and after manual check (e). Red circles above the images show bubbles circumferences.

Looking at the output of the Hough transform and considering the original pictures, it was noticed how in most cases the real bubble was surrounded by others circumferences while some bubble weren't recognized.

The last step was a refinement of the final result working on the original image, where the bubbles in focus have the characteristic light reflection on both the upper and lower part of it. An automatic algorithm, which eliminates the internal circles, was implemented and a manual addition of undetected bubbles was done.

An example of application of the implemented image post-processing method is shown in Figure 5.1.

The determination of the final BSD is then obtained by evaluation of a scaling factor calculated by measuring the correspondent length in pixels of a reference length in meters. This operation was done for each series of pictures and an average value of the scaling factor was then calculated.

5.4.2 Manual detection of BSD

The validity of the semi-automatic detection method was checked against a size distribution of the bubbly flow obtained through a manual detection method. The same original images processed with the just described semi-automatic method were used to detect the in focus circumferences of the bubbles which were directly drawn on the pictures obtaining the position of the bubbles and their radius (this method has been developed by means of Matlab® v7.1 software too).

This choice was driven by the fact that no other methods to evaluate the bubble size distribution were available to validate the results of the circular Hough transform.

The manual determination of the BSD was also performed to verify the incidence of effects due to optical aberrations and reflections on the bubble surface on the final diameter recognized. To perform this validation, transparent crystal glass spheres of different known diameters were used and, once the scaling factor were determined, the correspondent diameter was calculated.

The crystal glass spheres were chosen in order to make the comparison with the most similar material with respect to a gas bubble. In particular, the presence of the characteristic reflection on the bubble surface observed for the

gas bubbles in focus was researched, in order to evaluate its effect on the estimation of the bubble diameter. In fact, the presence of the reflection on the bubble surface is the most important aspect that leads to the bubble detection. In this way, an assessment of the error due to the manual BSD determination was obtained.

Chapter 6

Comparison between numerical results and literature test cases

6.1 Introduction

The evaluation of the numerical model described in Chapter 4 has been performed by comparison with two literature test cases.

The first test case regards the prediction of the steady concentration field of a passive scalar injected into a system. This test checks only the Eulerian part of the model, because the passive scalar is considered as a dissolved species. No source term is involved and the time evolution of concentration until a stationary condition is reached depends only on the convective and diffusive terms of equation (4.3.1). More precisely, the concentration field depends both on the steady flow field calculated by the FV simulation and on the integration of the concentration equation. To perform this evaluation, the literature case of Antoine et al. (2001) has been chosen, in order to collect the necessary experimental data for the analysis of the model behaviour.

The second comparison with experimental data from literature has been carried out in order to set the values of parameters of the Monod type kinetic

model for heterotrophic biomass, readily biodegradable organic substrate and dissolved oxygen. This operation allowed simultaneously the validation of the source terms modelled in the complete model (E-L model with several dissolved species).

6.2 Turbulent transport of a passive scalar

To validate the model behaviour for the transport of a passive scalar the work of Antoine et al. (2001) has been considered. Inside their work, the authors investigated experimentally the mass transport within a round turbulent jet of water discharging into a low velocity co-flowing water stream.

The velocity field and the concentration field of an organic dye (rhodamine B) were measured. They chose this tracer because it is very soluble in water and its fluorescence can be easily induced by the green beam of the laser Doppler velocimeter, which they used to evaluate the concentration field through the transparent wall of the channel.

The experimental apparatus consisted in a square channel, inside of which, at the centre of the reference initial section, a circular jet was placed. A low concentration of rhodamine B was initially fed inside the system and then recirculated by means of a pump, which simultaneously kept the co-flow constant.

A scheme of the experimental set-up is shown inside Figure 6.1 while the main characteristics of the experimental geometry, the boundary conditions values of the flow and of the rhodamine B concentration are listed in Table 6.1.

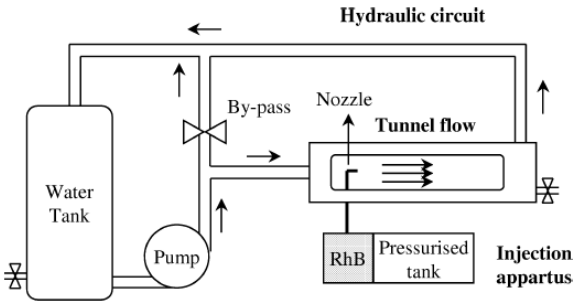

Figure 6.1 Scheme of the experimental apparatus (Antoine et al. (2001))

Parameter	**Value**
l, length of the side of the square channel	63 mm
L, length of the channel	1.5 m
U_1, velocity of the co-flowing stream	0.5 m/s
d, jet exit diameter	1 mm
U_0, initial jet velocity	10 m/s
C, initial concentration of rhodamine B	$5 \cdot 10^{-6}$ mol/l
measurement region (x direction)	x/d = 50 to 140

Table 6.1 Geometry and boundary conditions of experiments

6.2.1 Liquid flow simulation

From the point of view of the numerical model, the first step was the validation of the velocity field simulated by means of the FV CFD code (see paragraph 5.1) by comparison with the experimental data measured by the authors. Even if the problem is evidently axisymmetrical, the entire cross section of the channel has been represented in the mesh to allow the computation of the flow field. Nevertheless, to limit the computational efforts, the length of the model has been limited to the final section located at x/d = 180.

The inlet boundary conditions of the model has been imposed in accordance with the velocity data of Table 6.1 and a pressure condition has been assigned to

the entire end section located at x/d = 180. A slip condition has been imposed at the channel walls, because they are far enough not to influence the velocity field development (as the authors noticed); for the same reason a coarse grid near the walls has been maintained. The computing grid has been created starting from cells of size 0.002 m x 0.002 m x 0.002 m later refined at the inflow position and within the area of interest for comparison with experimental data. The total number of cell in set was 715860.

The computational grid is reported inside Figure 6.2 together with a snapshot of the adopted jet exit geometry.

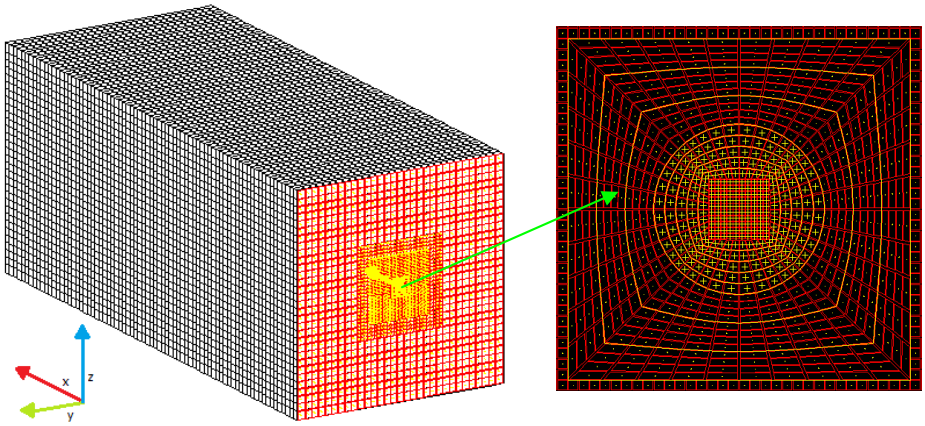

Figure 6.2 Geometry of the computational grid and particular of the jet exit modelling

The interpolated value of the velocity components at the centre of each computational cell were considered in order to perform the comparison with the experimental data. Scaled velocity profiles were considered, with respect to both the length scale (x axis) and the velocity scale (y axis of the plot), where U_m indicates the local centreline longitudinal excess velocity (with respect of the co-flowing external stream velocity) and r is the radial distance from the jet centre.

6.2.1.1 Sensitivity analysis on turbulence model

In order to evaluate the most suitable turbulence model to represent the physical situation., the comparison between the velocity profiles, at several *x/d* locations downstream the jet exit, has been performed considering either the *k-ε* RNG turbulence model and the *k-ε* standard turbulence model. The radial distribution of the normalized longitudinal velocity at *x/d* = 50 and *x/d* = 80 of the two abovementioned turbulence models is shown in Figure 6.3.

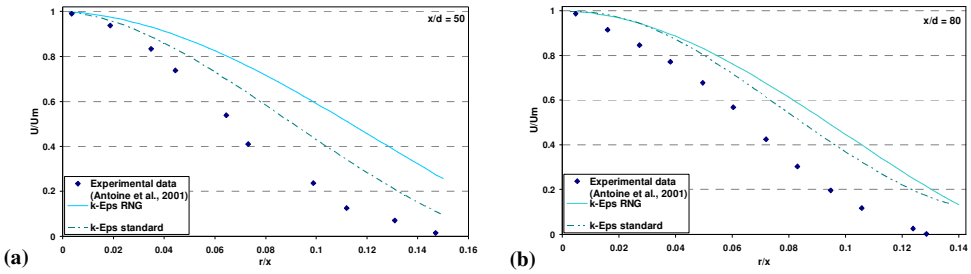

Figure 6.3 Radial distribution of the longitudinal velocity at *x/d* = 50 (a) and *x/d* = 80 (b) for the *k-ε* RNG and the standard *k-ε* turbulence models compared with the experimental data of Antoine et al. (2001)

The considerable gap provided by the application of the *k-ε* RNG turbulence model compared to the experimental data has led to exclude its use focusing instead on the *k-ε* standard model, which shows a closer agreement (though not optimal) with the experimental values of Antoine et al. (2001).

In order to reproduce as closely as possible the performance of the experimental data, a sensitivity analysis was conducted on the coefficients required by the *k-ε* standard turbulence model, with particular attention to the coefficients $c_{\varepsilon 1}$ and $c_{\varepsilon 2}$ of the turbulence dissipation rate balance equation (relation (5.1.12)).

To this end, both the radial distribution of the mean longitudinal velocity and the streamwise variation of the centreline mean longitudinal velocity were

considered to finally detect the most suitable values of the constants needed for the simulation of the literature experiment.

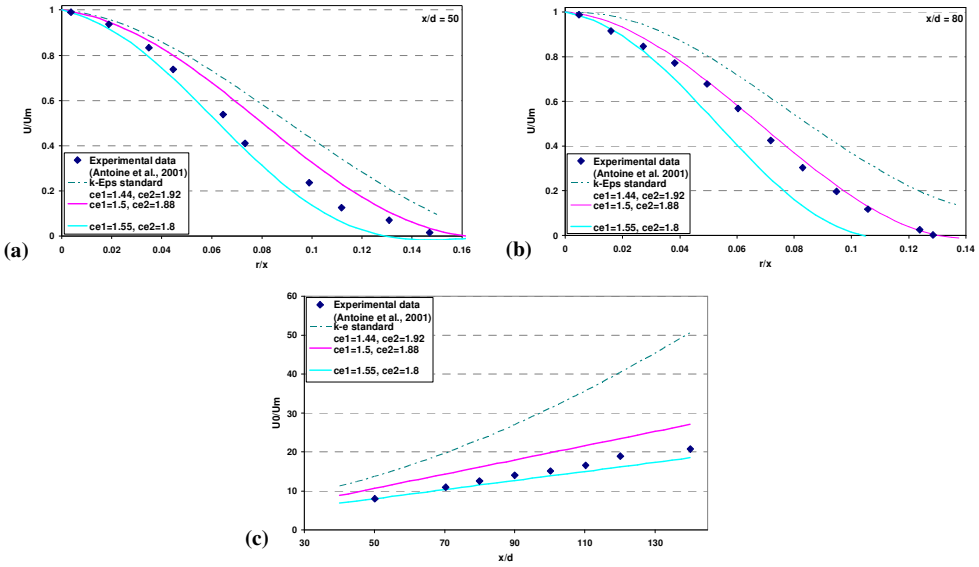

Figure 6.4 Radial distribution of the longitudinal velocity at *x/d* = 50 (a) and *x/d* = 80 (b) and streamwise distribution of the centreline longitudinal velocity (c) for the extreme values of variation of the constants *cε1* and *cε2* of the standard k-ε turbulence model

The comparison between the standard k-ε turbulence model with unmodified values of constants $c_{\varepsilon 1}$ and $c_{\varepsilon 2}$ (equal to 1.44 and 1.92 respectively) and the results obtained with the limits of variation of these constants considered during the parameters analysis is proposed in Figure 6.4. It can be noticed that, moving downstream, the simulation with parameters $c_{\varepsilon 1}$ = 1.5 and $c_{\varepsilon 2}$ = 1.88 ensures a most closer description of the radial distribution of the mean longitudinal velocity, even if the spreading rate along the x direction of the mean longitudinal velocity seems to be lower than the experimental evidence. Several simulations were carried out in order to assess the best parameters choice,

considering different combinations of values inside the limits of variation highlighted in Figure 6.5.

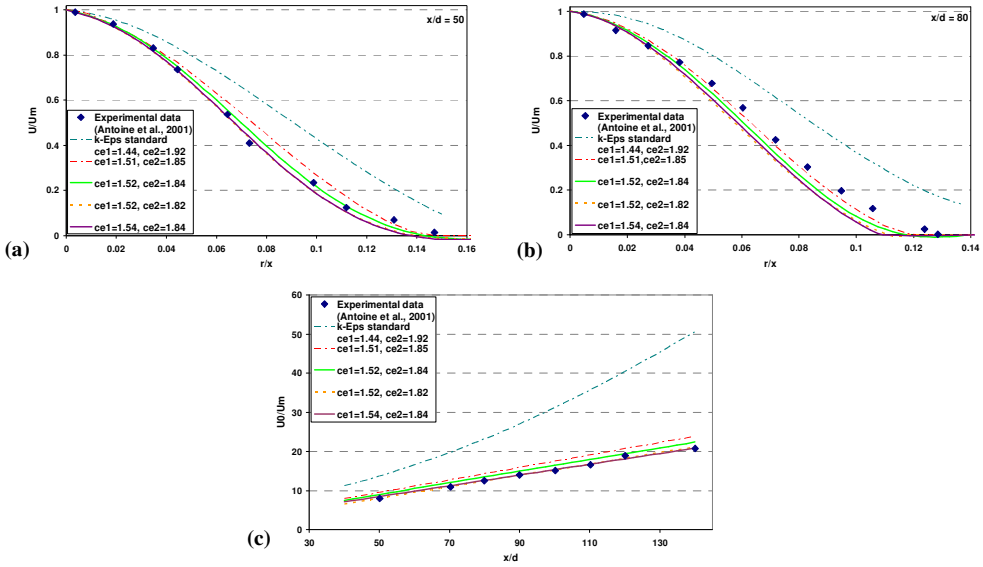

Figure 6.5 Radial distribution of the longitudinal velocity at *x/d* = 50 (a) and *x/d* = 80 (b) and streamwise distribution of the centreline longitudinal velocity (c) for several values of variation of the constants $c_{\varepsilon 1}$ and $c_{\varepsilon 2}$ of the standard k-ε turbulence model

The numerical simulation results considering the variation of the constant $c_{\varepsilon 1}$ from a minimum value of 1.52 to a maximum value of 1.54, and of the constant $c_{\varepsilon 2}$ from a minimum value of 1.82 to a maximum value of 1.85 are shown in Figure 6.5. Analysing the velocity distributions it can be noticed that the simulation characterized by $c_{\varepsilon 1}$ and $c_{\varepsilon 2}$ values of 1.52 and 1.82 respectively and the simulation characterized by $c_{\varepsilon 1}$ = 1.54 and $c_{\varepsilon 2}$ = 1.84 behave in a very similar way both for the radial and for the streamwise distribution of velocity. In particular, it can be seen that the prediction of the spreading rate along the longitudinal coordinate is very close with the experimental data. Nevertheless,

the radial profiles seem to move away from the data of Antoine et al. (2001) when the location *x/d* moves downstream the jet exit.

In order to establish a trade-off between the optimal reproduction of the radial velocity distribution and of the streamwise centreline longitudinal velocity distribution, the best couple of values for constants $c_{\varepsilon 1}$ and $c_{\varepsilon 2}$ has been considered to be 1.51 and 1.85 respectively. The results concerning the simulation with the considered values for the model parameters are shown in Figure 6.8.

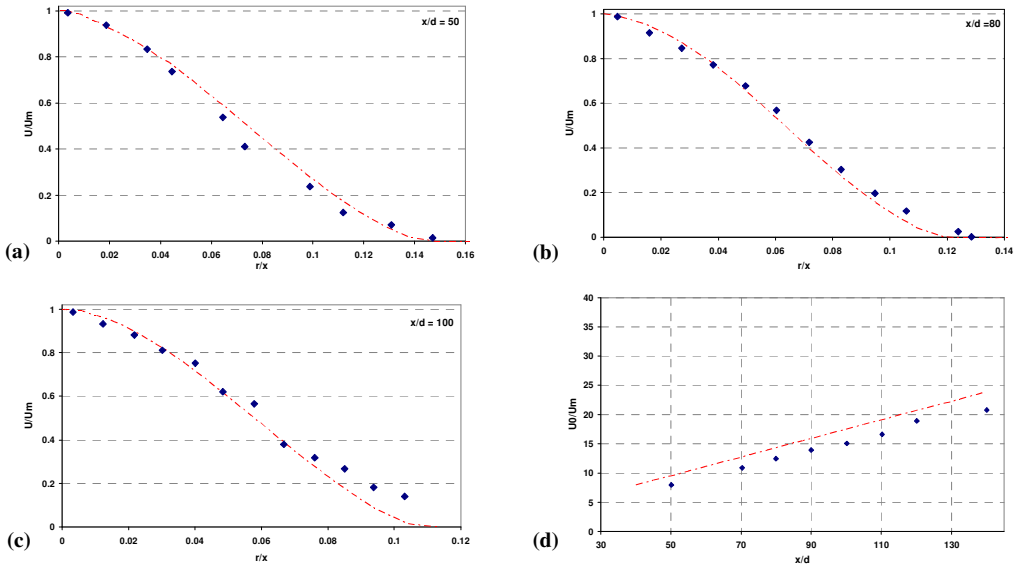

Figure 6.6 Radial distribution of the longitudinal velocity (x/d = 50 (a); x/d = 80 (b); x/d = 100 (c)) and streamwise distribution of the centreline longitudinal velocity (d) of the definitive simulation; dashed line = numerical results, symbols = experimental data (Antoine et al. (2001))

A good agreement of the numerical results with the experimental data can be noticed regarding the radial distribution of the mean longitudinal velocity. Almost the same diffusion rate along the longitudinal direction either for the

numerical results and the experiments is observed, even though a constant overestimation of the U_0/U_m ratio is established. The most probable reason of the discrepancy between the numerical and the experimental data can be attributed to a slight shift of the virtual origin of the numerical jet with respect to the experimental data. Anyway, this difference does not influence the global behaviour since the numerical and experimental results show the same diffusivity rate of the jet along *x* direction.

6.2.2 Simulation of the concentrations field

After the adequacy of the simulated liquid velocity field has been confirmed the procedure described in paragraph 4.3 has been applied and the interpolated values of velocity, turbulent kinetic energy and turbulence dissipation rate at the vertexes of a cartesian grid with cell dimensions of (0.001 m x 0.0005 m x 0.0005 m) have been calculated.

To simulate the test case, the interpolated velocity field is the only necessary input of the numerical model developed. The calculation of the concentration, until steady state condition was reached, was carried out following the procedure described in paragraph 4.3 after imposing the appropriate boundary conditions. The experimental concentration of dye was imposed at the entrance of the jet in the system. The initial concentration in the tank has been set equal to 0 and the calculation has been stopped when the passive scalar concentration field reached steady-state conditions.

The radial distribution of the normalised concentration (with respect to the maximum concentration at the reference position, C_m) is shown in Figure 6.7. The numerical concentration profile is compared with the experimental data at x/d = 50 and x/d =100. A slight departure of the numerical results from the experimental can be noticed, especially for higher value of x/d. In particular, the diffusion rate along radial direction seems to be higher for the experimental jet than for the numerical one. It can be seen that the numerical results reach the zero value at the boundary while the experimental data do not. However, if the same experimental ratio C/C_m at the last r/x position is considered to update the

calculated numerical concentration (by multiplying for the maximum centreline concentration) the expected agreement between the two series of data is found, as the behaviour of the green dashed curves in Figure 6.8 confirms.

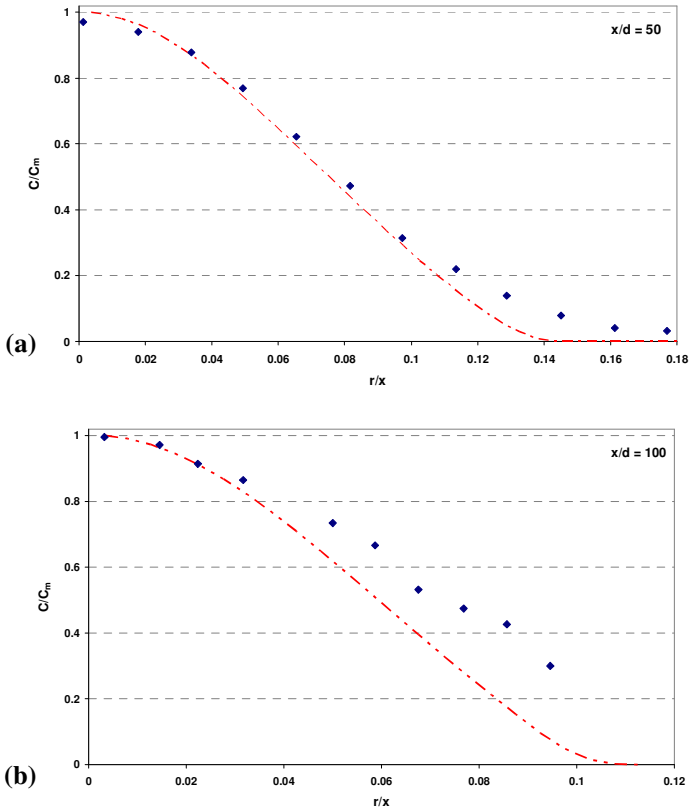

Figure 6.7 Radial distribution of the concentration at x/d = 50 (a) and x/d = 100 (b); dashed line = numerical data, symbol = experimental data (Antoine et al. 2001)

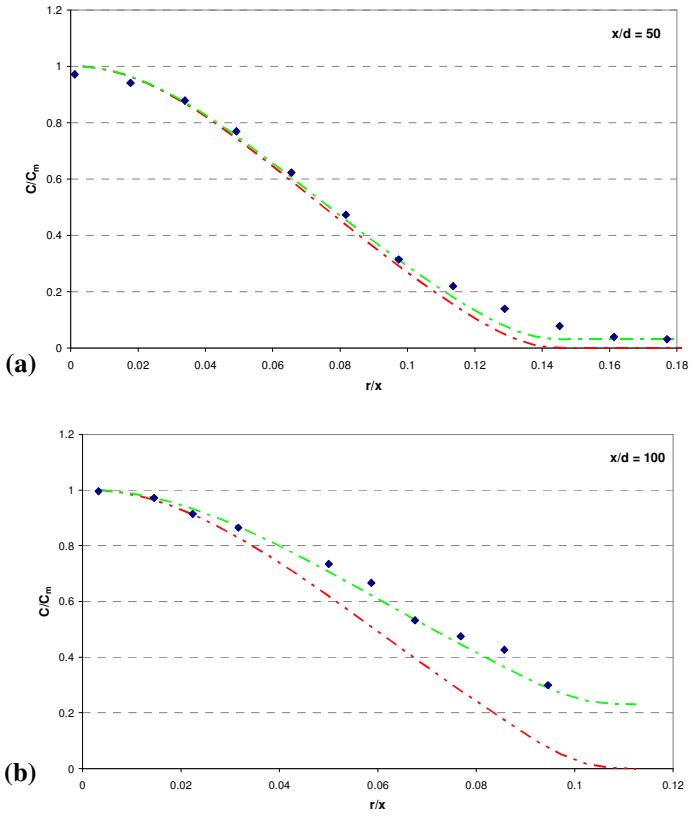

Figure 6.8 Radial distribution of the concentration at x/d = 50 (a), and x/d = 100 (b); dashed line = numerical data (red = original results, green = scaled results); symbol =experimental data (Antoine et al., 2001)

The comparison between the numerical longitudinal profile of the maximum concentration at the jet centreline normalised by means of the initial concentration C_0 and the correspondent experimental one is shown in Figure 6.9. Differently from the numerical results of the velocity field, a slightly higher diffusive rate can be observed in the numerical results.

This departure of numerical results from experiments is, however, of little magnitude and can be justified by the downstream propagation of a little diffusive numerical contribution.

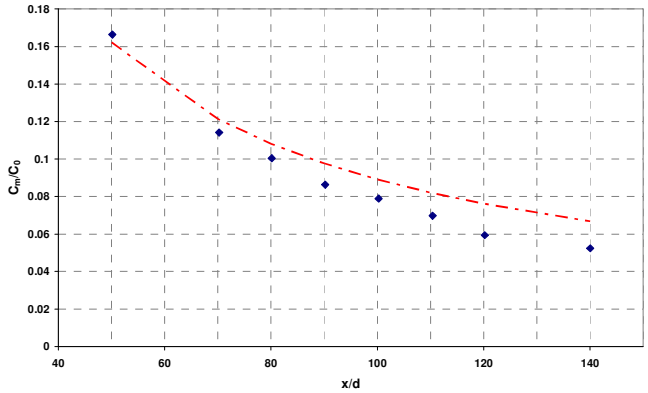

Figure 6.9 Streamwise distribution of the centreline longitudinal concentration; dashed line = numerical data, symbol =experimental data (Antoine et al., 2001)

Anyway, the global behaviour of the experimental results is well reproduced by the numerical procedure (liquid velocity field and numerical model for the resolution of the concentration field).

In conclusion, the results of the methodology applied for predicting the concentration field of a passive scalar can be considered satisfactory in relation with the purposes of the research activity.

6.3 Modelling the kinetics of biomass growth, substrate removal and DO demand

The second situation that has been evaluated with respect to experimental data from literature is the capability of the model to reproduce, with the explicit method adopted for the time integration of concentration, the evolution of the concentration of several species. This represents the first step toward the modelling of a multispecies two-phase E-L model.

The structure of the computational model has been therefore modified in order to take into account the presence of several dissolved species. It must be

observed that if the assumption to consider the species as dissolved is absolutely appropriated for dissolved oxygen and organic substrate, while it is not definitely true for the biomass. In fact, inside of the bioreactor bacteria grow and cluster together and with insoluble solids and eventually they form flocs even if the dimension of the individual bacterial cell is only of few microns.

Despite of this, to consider the biomass as flocs (and consequently to regard it as a new population of particles inside the model) has been believed beyond the aim and the structure of the developed numerical model. So, also the biomass has been considered as a dissolved species.

However, it has been decided not to give up to model a real situation, even if the parameters commonly provided in the literature and valid for a real system, where, as explained in Chapter 3, there are numerous processes and species involved, were not taken into account. For this reason, we preferred to consider experimental data in literature related to a simple preliminary approach, where, basically, the processes involved deal with the evolution of a single species of aerobic microorganisms and the simultaneous degradation of simple organic substrates.

In this regard, the work of Martìn et al. (2009) has been considered as a suitable starting point. Inside their work, the authors used “synthetic water” to model the progress curves of cell growth, organic matter consumption and oxygen demand. Several species of microorganism were considered (Bacillus Subtilis, Escherichia Coli and Pseudomonas Putida) by using glutamic acid and glucose as organic matter.

They fitted the experimental curves using both logistic and Monod models (see Chapter 3), even though only the parameters of the logistic model were determined.

Among the various tests reported in their work, the test performed with Pseudomonas Putida and glucose has been selected for the evaluation of the coefficients of the Monod model, which is indicated by the authors as the most suitable for the interpretation of experimental data. Endogenous decay was not considered to model the new components of the source terms of equation (4.3.1)

and (4.3.2). In particular, the relations that have been implemented in the model are:

$$\frac{dx}{dt} = K_m \frac{S}{K_S + S} x \tag{6.3.1}$$

$$\frac{dS}{dt} = \alpha K_m \frac{S}{K_S + S} x \tag{6.3.2}$$

$$\frac{dS_{BOD}}{dt} = \beta K_m \frac{S}{K_S + S} x \tag{6.3.3}$$

where:

x = biomass concentration (kg/m³);

K_m = maximum value of the specific growth rate at saturation concentrations of growth-limiting substrate (s^{-1});

K_s = saturation constant, it corresponds to the substrate concentration at which the growth rate is equal to $K_m/2$ (kg/m³);

S = glucose concentration (kg/m³);

S_{BOD} = BOD concentration (evaluated as the difference between initial DO and residual at time t) (kg/m³);

α = unit of substrate consumed to produce one unit of bacterial growth;

β = unit of DO demanded to produce one unit of bacterial growth.

A regression analysis has been done to evaluate the parameters of equations (6.3.1) to (6.3.3) starting from initial concentration values of biomass and substrate (x_0 and S_0) respectively equal to 0.75 mg/l and 8.75 mg/l.

Two different sets of parameters seem to fit the experimental data with the same accuracy, even though the second one gives rise to a behaviour more

similar to that reported by the authors. The value of each parameter is reported in Table 6.2.

Parameter	**Value - test case *A***	**Value - test case *B***
α	1.8	1.8
β	1.15	1.15
K_m	0.000025 s^{-1}	0.000015 s^{-1}
K_S	2.75 mg/l	0.00001 mg/l

Table 6.2 Value of the Monod kinetics parameters

The values of the coefficients α and β was unchanged for the two set of parameters, however an appreciable difference regards the value attributed to K_s. The value found for the test case *A* seems more reasonable with respect to its physical meaning (substrate concentration at which the biomass growth rate reaches the half of its maximum value) and the resulting curves present a smoothed transition to the limit condition (stop of the biomass growth due to the compete depletion of substrate) as can be noticed in Figure 6.10, while, once the substrate is completely assimilated by the biomass, an abrupt variation of the trend of the curves happens for the test case *B*.

As mentioned inside Chapter 3, BOD growth and dissolved oxygen consumption are obviously related each other. The dissolved oxygen sink term can be deduced from equation (6.3.3) by placing a minus sign to the right hand side term.

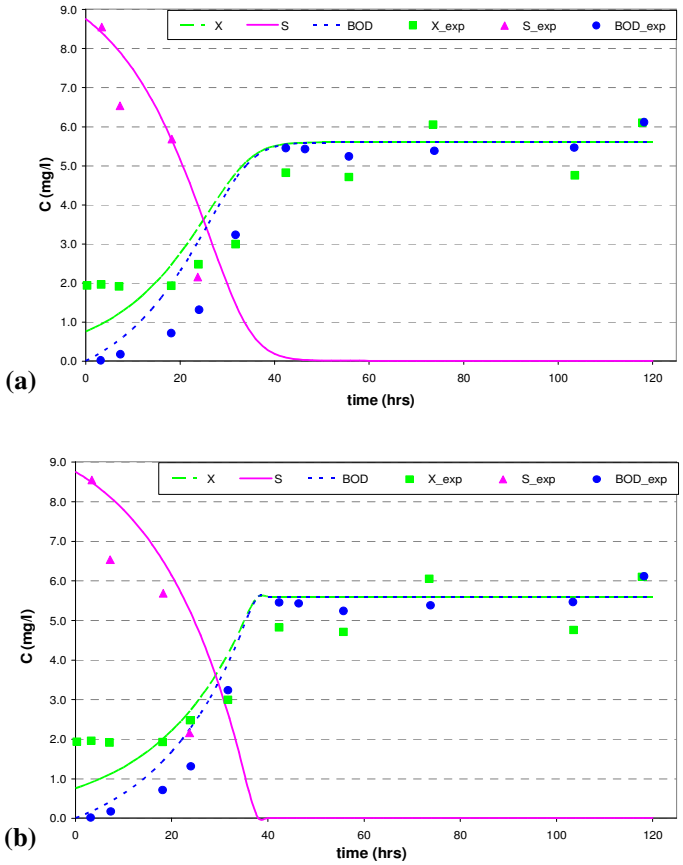

Figure 6.10 Progress curves for bacterial, substrate and BOD concentrations, (a) test case *A*, (b) test case *B* (line = numerical results; symbols = experimental data from Martìn et al., 2009 green = biomass, red = substrate, blue = BOD)

Finally, it must be considered that in the evaluated experimental situation the dissolved oxygen concentration did not fall below the residual threshold of 2 mg/l. For this reason, the additional term considered in order to take into account the limiting effects due to the achievement of low dissolved oxygen concentration has not been considered during the parameters evaluation. In fact,

no limit conditions were reached since the final dissolved oxygen concentration was of 2.4 mg/l.

Nevertheless, the possibility that dissolved oxygen can become a limiting factor for the biomass growth has been considered within the modelling of the source terms involving the kinetics of biomass, substrate and dissolved oxygen inside the E-L model, as reported in equations (4.3.19) (4.3.20) and (4.3.21).

The suggested value for the saturation constant K_{DO} for heterotrophic bacteria can be assumed to be equal to 0.2 mg/l (ASME model (2000)).

Chapter 7

Application of the E-L model to laboratory test cases

7.1 Introduction

The proposed methodology to the simulation of the evolution over time of the dissolved oxygen concentration transferred from a two-phase jet of gaseous oxygen and water, has been tested by comparison with laboratory test cases.

Within this chapter, the experimental set-up adopted, the strategy followed for the experimental and numerical determination of the necessary inputs of the model and the comparison with experimental measurements of dissolved oxygen concentrations during oxygenation test is presented.

A sensitivity analysis on the key parameters of the numerical model, with particular regard to the calculated bubble size distribution and to the adopted mass transfer models for modelling the transfer of oxygen from the oxygen bubbles to the liquid phase has also been performed.

7.2 Experimental set-up

The experimental test were carried out at the laboratory of Hydraulic and Environmental Engineering of University of Pavia.

The laboratory set up consists of a plexiglas rectangular tank which represents a scaled model of an oxygenation tank of a wastewater treatment plant. The tank is 0.8 m wide (*W*), 1.8 m long (*L*) and 0.9 m high (*H*) and filled with tap water.

The operations of mixing and oxygenation are performed by means of a jet system, which recirculates the liquid flow rate sucked in by the pump and injected inside the system by means of a feeding duct which ends with a circular nozzle. Indeed, three nozzles are placed on the feeding duct, but only one nozzle at work has been considered during the research activity. The water height *(h)* inside the tank was maintained to a level of 0.6 m in order to keep the jet steady. In fact, Sibilla and Raboni (2008) demonstrated that an exponential relation between the water level and the oscillatory response of the liquid flow is established. In particular for a ratio *W/L* = 0.44 the jet can be considered steady for a *h/W* value greater than 0.5.

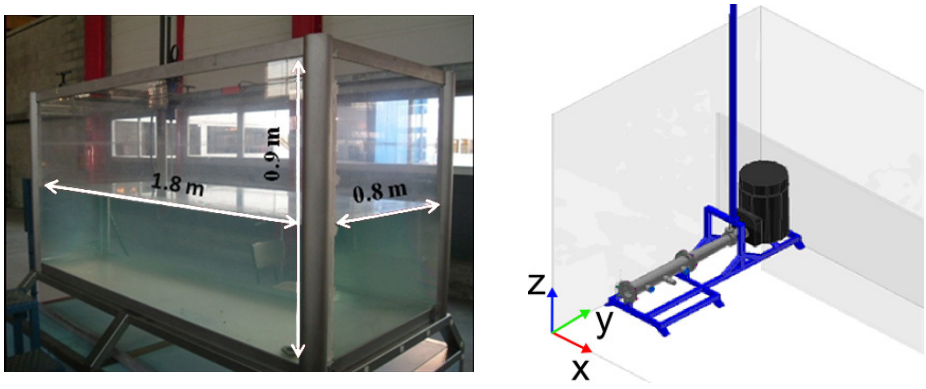

Figure 7.1 Scheme of the laboratory experimental apparatus

Moreover, to limit the unwanted disturbance induced by the pump suction on the fluid flow, a longitudinal plexiglas partitioning wall 1.48 m long has been placed inside the tank and the original width has been reduced to 0.6 m. A scheme of the experimental apparatus is shown in Figure 7.1 and the main properties of the system are summarised inside Table 7.1.

Parameter	**Value**
D, jet exit diameter	0.0085 m
U_0, initial jet velocity	9.42 m/s
x_0, x coordinate of the centre of the nozzle	0.14 m
y_0, y coordinate of the centre of the nozzle	0.30 m
z_0, z coordinate of the centre of the nozzle	0.086 m
Q_g, gas flow rate	$2.4 \cdot 10^{-5}$ m^3/s

Table 7.1 Geometry and boundary conditions of experiments

The mean velocity of the jet has been determined through an energy balance performed between the upstream section and the nozzle exit section. The total head owned by the upstream current has been determined by pressure measurements using a pressure transducer connected to the pressure plug placed at the outer section of the feeding duct. The average measurement error of the liquid flow rate has been estimated to 1% (Raboni (2010)).

The oxygen injection takes place just downstream of the nozzle by means of a small plastic needle placed below the jet exit, which release the mean oxygen flow rate. At this position liquid and bubbly flow mix together to form a two-phase flow and a partial breakup of the bubble flow is established. The calculated gas volume fraction of the system (equation (2.2.8)) is then equal to 0.04.

The same environmental conditions (liquid and gas flow rate, water and external temperature) have been maintained during the whole experimental test including the bubble detection, the measurement of the dissolved oxygen concentration and the velocity measurements.

7.3 Determination of the inputs of the E-L model

7.3.1 Liquid flow field determination (case study 1)

The first configuration examined was the lab-tank model described inside paragraph 7.2.

Following the procedure described in Chapter 5, the liquid velocity field was determined.

The computational mesh developed was constituted of 959440 hexahedrical cells of dimensions of 0.01 m x 0.01 m x 0.01 m in the outer region and more refined near the jet exit and the boundaries. The inlet velocity was assumed to be constant and uniform. A slip wall condition was used on the free surface, while a standard log law for smooth walls was imposed to the velocity at solid boundaries; a zero pressure condition was imposed at the outlet.

The computational mesh with the highlighted boundary conditions is shown in Figure 7.2.

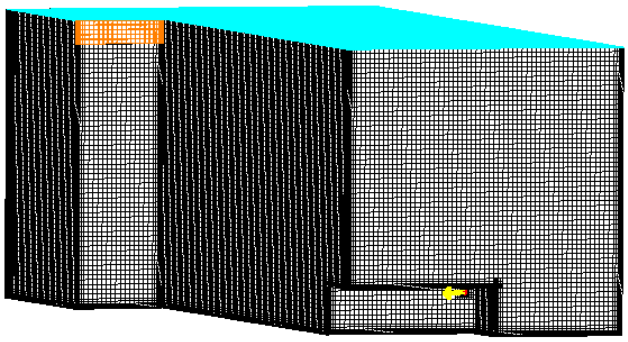

Figure 7.2 Computational grid with boundary conditions (yellow vector = jet velocity; orange = zero pressure condition; light blue = slip condition at the free surface)

The portion of the tank occupied by the pump-nozzle system was simplified as a rectangular parallelepiped of length 0.14 m, width 0.32 m and height 0.1 m, which was removed from the bottom of the computational grid. Due to the low velocities observed in the feeding channel of the pump, the computational mesh has been truncated to the coordinate x = 1.3 m.

Several simulations were conducted in order to set the parameters of the model and the location of the outlet conditions the closest to the operational conditions observed.

One of the problems involved the imposition of the correct velocity value at the nozzle exit section. Unfortunately, the high velocity at the jet exit did not allow the use of the ADV to measure the velocity components at the exit but only an estimate of the average velocity were carried out (as just mentioned inside paragraph 7.2). This fact did not allow to take into account the slight misalignment of the jet axis with the x direction. This discrepancy was compensated "a posteriori" by adopting as inlet velocity, the vector value which gave the best fit in terms of position of the point of maximum velocity in the plane jet. In particular, for the final configuration adopted, the following values were imposed to the velocity at the inlet: V_x = 9.32 m/s, V_y = 0.19 m/s and V_z = -0.63 m/s, which means that the jet axis forms with the x axis an angle of 1°10' in the horizontal plane and of 3°50' in the vertical one.

7.3.1.1 Characterization of the jet behaviour

In order to characterize the jet behaviour, the comparison of the numerical velocity field with the experimental data of a circular wall jet with an offset from a solid boundary (Davis and Winarto, 1980) has been carried out.

The comparison of the dimensionless profile of the longitudinal velocity in the direction perpendicular to the wall is shown in Figure 6.8 (a) where three different x/D position are evaluated (x/D = 20, 30 and 50).

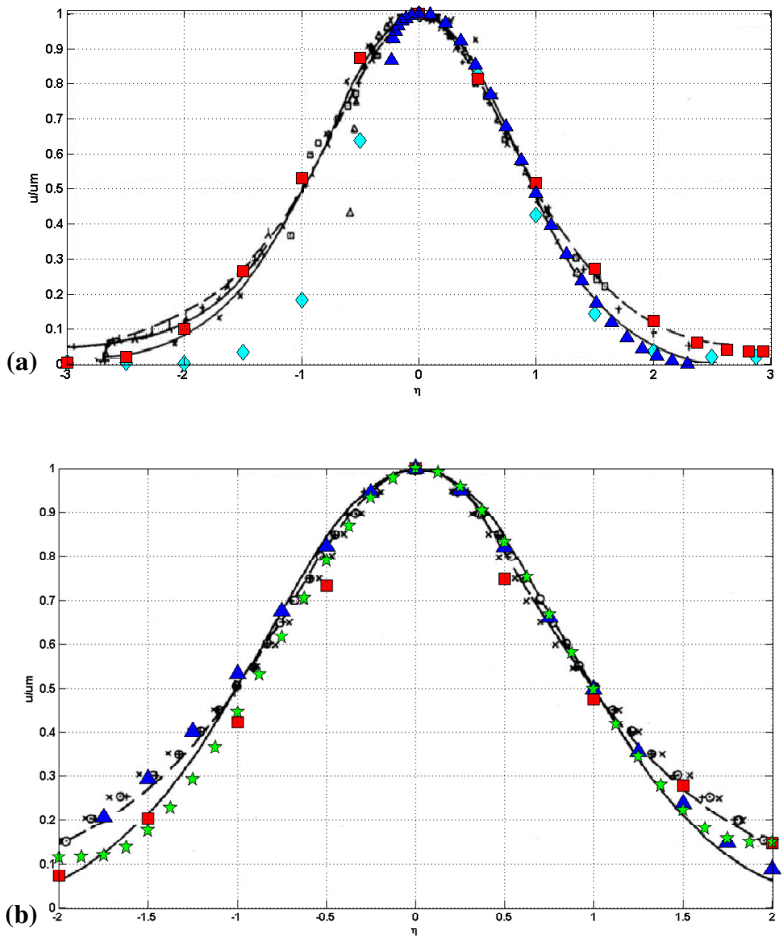

Figure 7.3 (a) Dimensionless velocity profile perpendicular to the wall, (b) parallel to the wall. Numerical results at x/D=20 (ciano diamond marker), x/D = 30 (red square marker), x/D = 50 (blue triangular marker) and x/D = 70 (green star marker); lines: circular turbulent free jet solutions; experiments (black symbols): (a) ×, *x/D* =4.5;+, *x/D* =8;λ, *x/D* =16;□, *x/D* = 32;○, *x/D* =48; Δ, *x/D* =64 (b) +, *h/D* =4; ○, *h/D* =1; ×, *h/D* =0.5

It can be noticed that for the downstream position nearest to the jet exit the velocity profile just above the wall ($\eta < 0$) underestimates the experimental data

of Davis and Winarto (1980) and also the analytical solution of a free circular jet (continuous and dashed lines).

This behaviour may be due to the presence of the vertical wall placed behind the jet exit which interferes with the development of the jet. For x/D = 30 the behaviour of the jet is very similar to the experimental and analytical results even if an asymmetry of the profile can be observed, while for the greatest value of x/D a decrease of the maximum velocity can be noticed for the smallest values of η since the impact with the solid wall is near to occur. At this position, the dimensionless velocity profile lays below the one of the free jet for the highest values of η.

In Figure 6.8 (b) the comparison of the dimensionless profiles of the longitudinal component of velocity parallel to the plane wall is shown at x/D = 30, 50 and 70. It can be noticed that the behaviour of the jet is quite close to the one of the free jet even if a slight decrease of the transversal diffusion rate can be observed since the results, especially for $\eta > 0$, lie behind the experimental and analytical data.

The position y_m of maximum longitudinal velocity above the solid wall has been calculated for different velocity profiles lying on the vertical that plane passes through the nozzle exit and then compared with the experimental values already reported in Figure 1.8.

The clearance value for the laboratory model is h/D = 10.1176. For this reason the numerical results are initially placed above the experimental data which consider a maximum h/D ratio of 4 (where h is the offset from the solid wall) as shown by Figure 7.4.

The initial position of the point of maximum velocity is maintained for a length of ten diameters downstream the nozzle exit, after which a steep decrease occurs until the lower part of the jet impacts with the solid boundary layer at x/D = 80. The maximum velocity position above the solid wall increase slowly owing to the thickening of the boundary layer.

A more clear representation of the diminishing of the jet centreline velocity moving downstream of the nozzle exit can be appreciated looking at Figure 7.5, where the vector velocity plot of the horizontal plane at the nozzle elevation is shown. The presence of a recicirculation zone with vertical axis between the right side of the jet core and the side wall can be noticed. Moreover, it can be seen the impingement of the jet against the frontal wall.

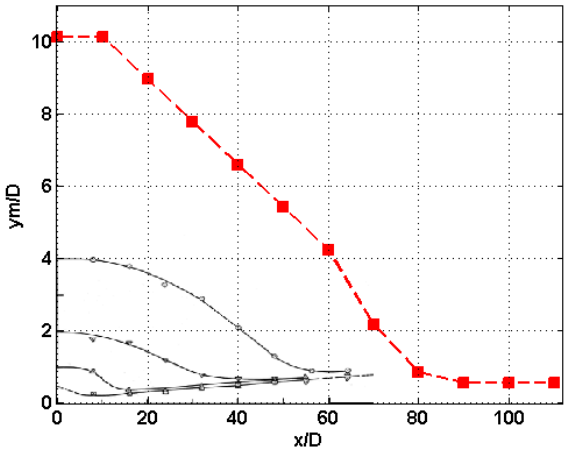

Figure 7.4 Location of the maximum velocity position above the solid wall; experimental data (Davis and Winarto, 1980) = black markers and lines (□, h/*D* = 0.5; Δ, h/*D* =1; ▽, h/D= 2; ○, *h/D* =4); numerical results = red dashed line and red square markers

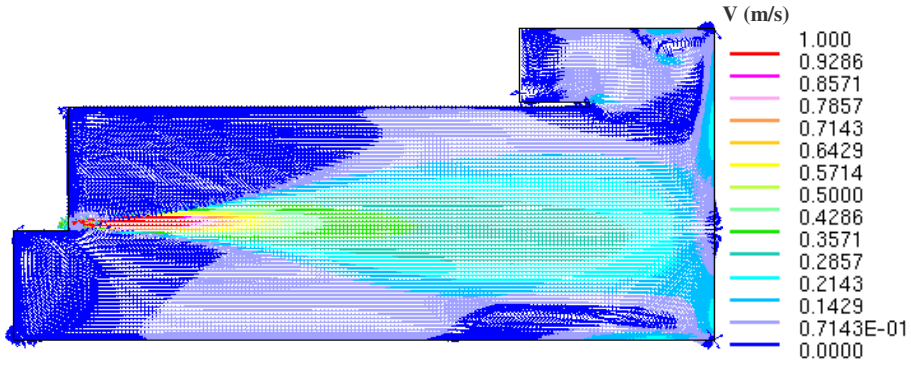

Figure 7.5 Case study 1: vector velocity plot (u_x and u_y) at z = 0.086 m

7.3.1.2 Validation of the numerical velocity field through experimental velocity measurements

The validation of the numerical simulations has been made by comparison with experimental velocity measurements carried out using an ADV velocimeter (as described in paragraph 5.2).

The instrument was moved by means of a manual handling system, designed during the research activity, which performs the translation of ADV along *x,y* and *z* directions (Figure 7.6).

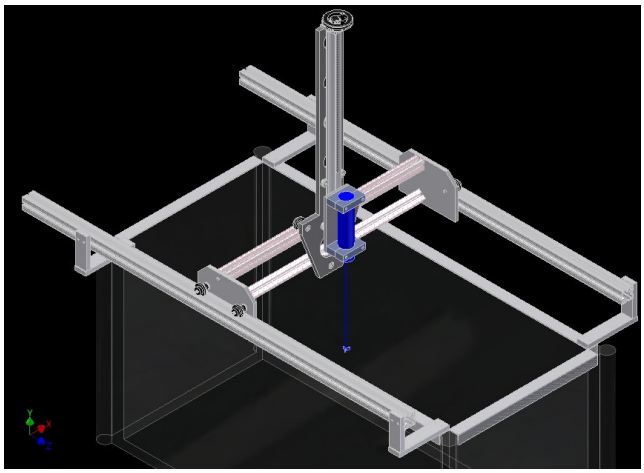

Figure 7.6 Scheme of the ADV handling system

Considering the reference system shown in Figure 7.1, two velocity profiles have been investigated: an horizontal velocity profile located at x = 0.97 m (half of the longitudinal length of the tank starting from the jet position) at the same elevation of the nozzle (z = 0.086 m) and a vertical velocity profile located at x = 0.97 m and aligned with the nozzle center (y = 0.30 m).

For each measure the sampling volume adopted was the largest one (9 mm) which should ensure the maximum measurement reliability. During the measurement operations, a decrease of the signal quality has been observed

when a velocity range different from 100 cm/s was considered. For this reason this range has been imposed to every measure, even when the related measurement error was equal to 1% of the velocity range for every points. The sampling frequency was 25 Hz and the acquisition was performed during a period of 10 minutes (15000 measures for each sample at each measurement position).

During the measurements, particular attention has been paid to the SNR signal, which has been checked to be higher than the threshold limit of 10-15 dB. The average correlation of the signal has been monitored too, even if no particular precautions are applicable to its control. Very good correlation values were found for the greatest part of the measurement points (higher than 90%) although the mean correlation fell just below the 70% closest to the jet axes.

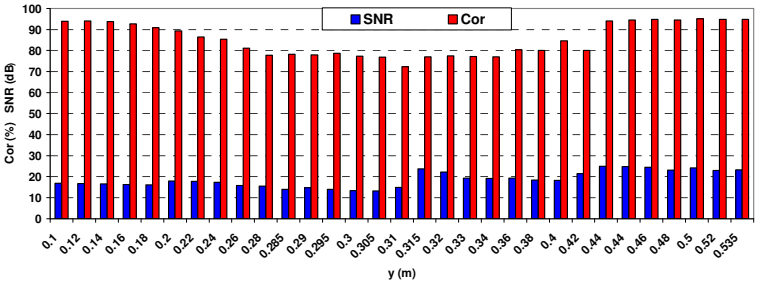

(a)

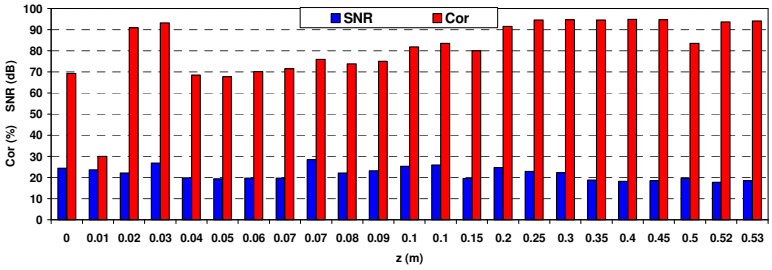

(b)

Figure 7.7 SNR and correlation values for the ADV measurements (a) horizontal profile (x = 0.97 m, z =0.086 m), (b) vertical profile (x = 0.97 m, y = 0.30 m)

SNR and correlation time-averaged values of each measurement are shown in Figure 7.7

The experimental results are compared to the numerical ones for the longitudinal component of velocity and for the turbulent kinetic energy at each measurement position (Figure 7.8).

Figure 7.8 shows that the numerical results agree quite well with the experimental ones. A slight overestimation of the experimental velocity at the jet centreline can be observed, even if it has to be considered that the measurement position is characterized by high velocity gradients along the vertical direction and, consequently, the disagreement of the numerical results has been considered not to affect the reliability of the numerical simulation, especially if one pays attention to the uncertainty associated with the resolution of the sampling volume.

Moreover, the asymmetry of the jet behaviour near the lateral walls is rather well represented since the left side of the numerical profile (holding the jet direction as reference) is shifted backwards with respect to the right one as the experimental measurements confirm.

The turbulent kinetic energy $k = \frac{1}{2}\left(\sigma_x^2 + \sigma_y^2 + \sigma_z^2\right)$ at each measurement position has been calculated through the evaluation of the RMS (Root Mean Square) deviation of the three measured velocity components (σ_x, σ_y and σ_z).

The comparison between the experimental turbulent kinetic energy and the numerical one reveals that the global behaviour is well represented even if the numerical values are quite higher than the experimental, especially at the jet centreline where the difference between them reaches the 20%.

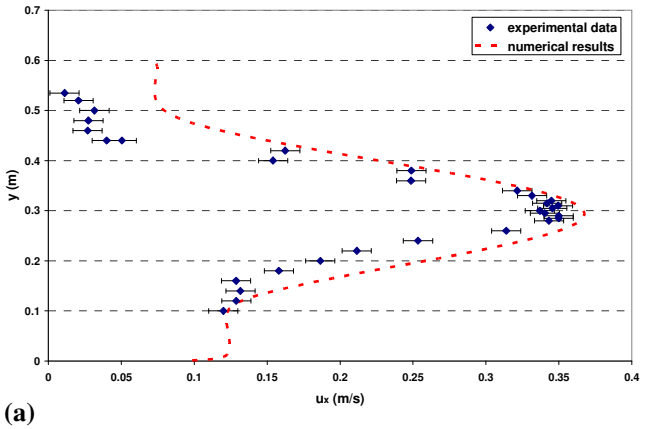

(a)

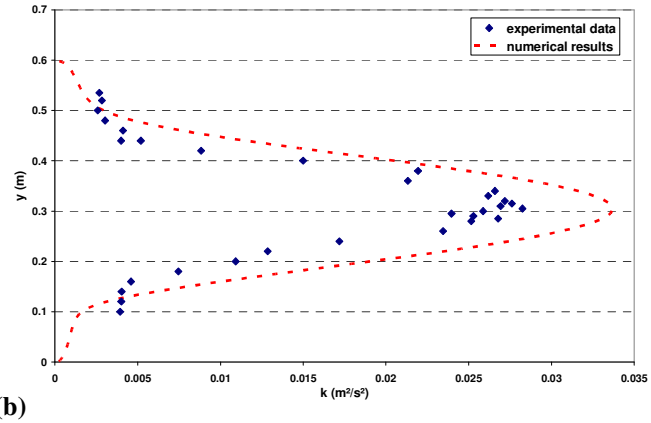

(b)

Figure 7.8 Profile parallel to the wall (x = 0.97 m, z = 0.086 m); (a) longitudinal velocity, (b) turbulent kinetic energy

This discrepancy could be associated with the fact that, at the centreline, the turbulent fluctuations can occur with a frequency higher than the sampling frequency of the instruments and, maybe, this can lead to an underestimation of the real turbulent kinetic energy of the jet. Actually, the frequency magnitude of the largest eddies may be evaluated by the ratio u_m/δ where δ is the jet half-width. At the considered axial position, where δ= 0.1 m and u_m = 0.35 m/s the eddy frequency can be estimated to be of order of 3-5 Hz. Although most of the turbulence eddy content can be related to these eddies, a small percentage of the

velocity fluctuations may be due to smaller eddies with characteristic frequency higher than 25 Hz, which are not detected by the ADV system.

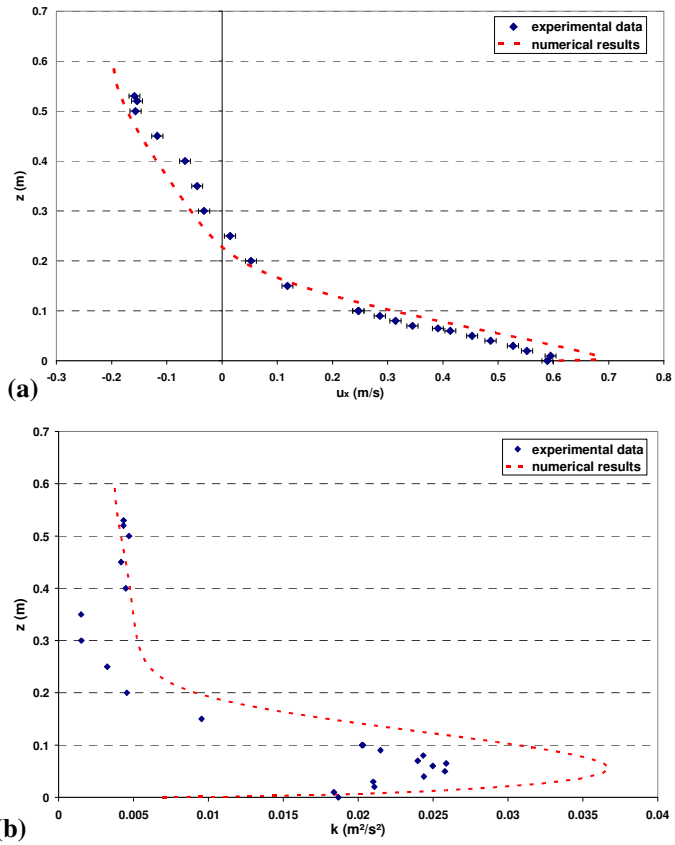

Figure 7.9 Profile perpendicular to the wall (x = 0.97 m, z = 0.30 m); (a) longitudinal velocity, (b) turbulent kinetic energy

The comparison between experimental measurements and numerical results of the longitudinal velocity profile and the correspondent kinetic energy along z direction is shown inside Figure 7.9.

A good agreement between measurements and corresponding numerical results can be seen, although a weak overestimation of the maximum velocity is

present in this case too. The large flow recirculation in the upper part of the tank, which is evidenced by the negative velocity values at $z > 0.22$ m, is well reproduced; the profile of turbulent kinetic energy reproduces qualitatively well the experimental one, although the predicted values are generally lower than the measured ones owing to the previously discussed reasons.

7.3.2 Liquid flow field determination (case study 2)

Starting from the experimental configuration of case study 1, a second configuration has been created with the aim of reproducing fluid recirculations and low velocity zones, in order to evaluate these effects on the dissolved concentration field of oxygen and other species. To obtain this goal, an additional partitioning plexiglas wall was positioned transversely, normal to the jet axis (Figure 7.10 (a)). The simulations of the fluid flow have been validated by experimental velocity measurements in which the signal analysis procedure highlighted in section 5.3 was performed.

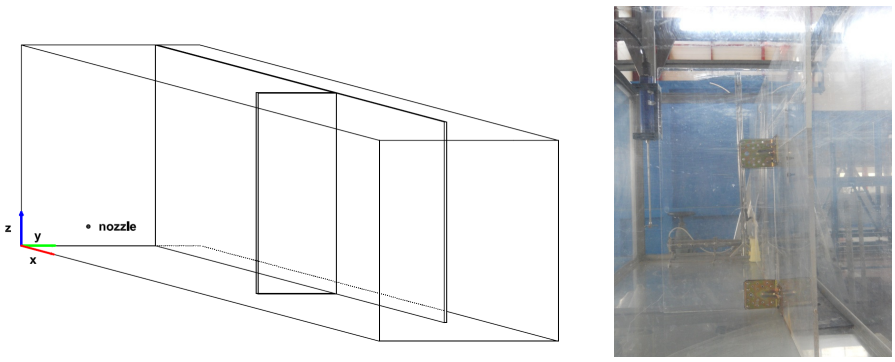

Figure 7.10 Case study 2: scheme of the laboratory experimental apparatus

The transversal partitioning wall was a Plexiglas vertical plane 0.01 m thick, 0.35 m wide and 0.8 m high, placed at x = 0.97 m. A scheme of the lab-model is presented inside Figure 7.10.

The computational mesh was composed by 979570 hexahedrical cells and the same boundary conditions considered for case study 1 have been imposed.

An example of the resulting velocity field (vector velocity plane at the nozzle elevation) is shown inside Figure 7.11. The impact of the jet against the transversal partitioning wall and the consequent strong deviation of the jet against the lateral side walls can be noticed. The presence of a low velocity zone downstream of the transversal wall is evident. Recirculation zones are present both upstream of the transversal wall at lateral position with respect to the jet development and downstream of the transversal wall (near the right lateral wall).

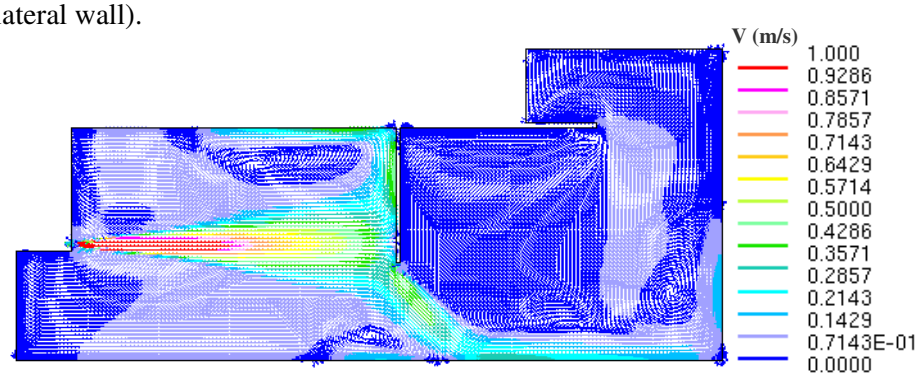

Figure 7.11 Case study 2: vector velocity plot (u_x and u_y) at z = 0.086 m

7.3.2.1 Validation of the numerical velocity field through experimental velocity measurements

The validation of the CFD simulation of the liquid flow has been performed by means of the comparison between the numerical velocity profiles and ADV velocity measurements.

The comparison between experimental measurement and numerical results concerning an horizontal (x=0.89 m, z=0.086 m) and a vertical (x=0.89 m, y=0.30 m) velocity profile of the mean longitudinal velocity are shown inside Figure 7.12 and Figure 7.13 respectively, together with the horizontal and vertical profile of the turbulent kinetic energy.

It can be seen that the experimental longitudinal velocity profiles along the horizontal and vertical directions are well reproduced by the numerical profiles, even if an underestimation of the velocity values closest to the jet axes is present for both of them.

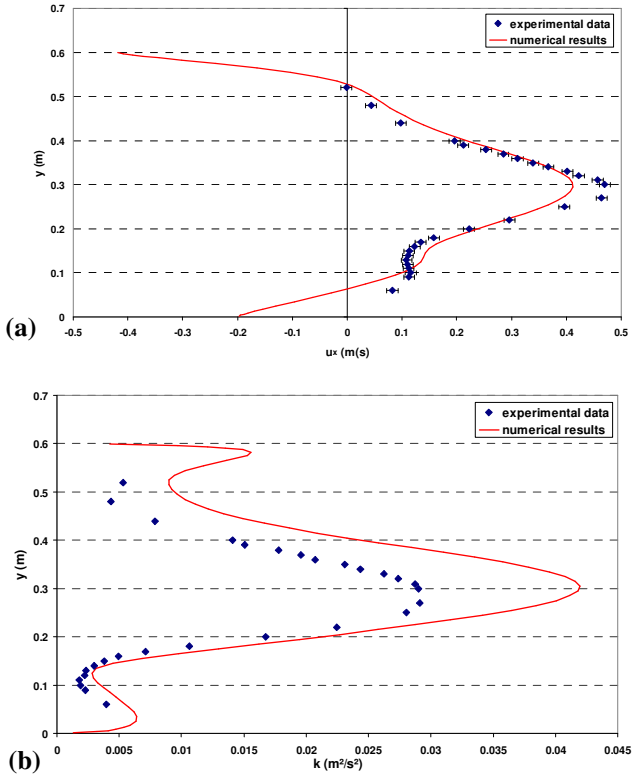

Figure 7.12 Horizontal profile (x = 0.89 m, z = 0.086 m); (a) longitudinal velocity, (b) turbulent kinetic energy

Nevertheless the global behaviour seems to be well reproduced. In particular, the presence of the bend on the right end side of the horizontal velocity profile is well predicted from the numerical simulation, as well as the decrease of the velocity near the side walls which preannounce the presence of the recirculation zones already highlighted in Figure 7.11.

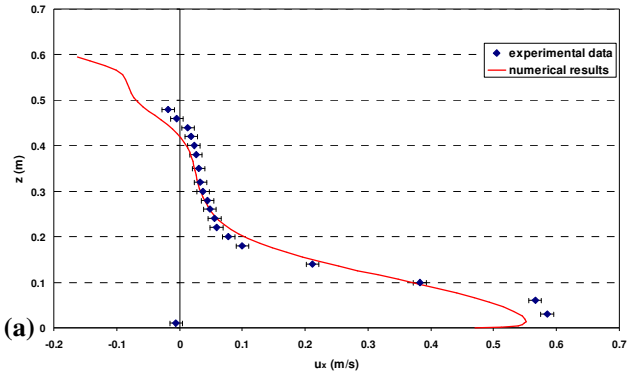

(a)

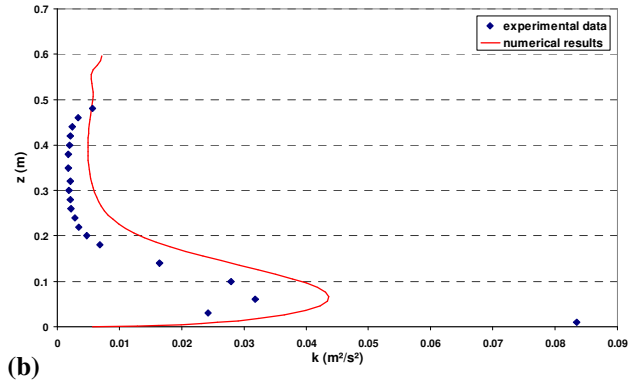

(b)

Figure 7.13 Vertical profile (x = 0.89 m, y = 0.30 m); (a) longitudinal velocity, (b) turbulent kinetic energy

The upper part of the vertical profile is very close to the experimental data and the presence of the superficial recirculation is detected both from measurements and from simulation (negative velocity at z = 0.48 m). An outlier experimental data is present at z coordinate equal to 0.01 m, since both the velocity and the turbulent kinetic energy values are very different from the contiguous ones.

Similarly to what observed for the turbulent kinetic energy profiles investigated in the case study 1, also the turbulent kinetic energy profiles at the measurement locations considered in Figure 7.12 and in Figure 7.13 reveal that

the profiles obtained from the experimental velocity measurements are considerably lower than those resulting from the numerical simulation. The probable explanation of this mismatch will be presented during the analysis of the effects produced by the velocity ADV signal processing.

7.3.2.2 Signal processing of ADV velocity data

The signal processing methods described in section 5.3, have been adopted to evaluate the effect of low SNR and correlation values on the measured velocity and on the corresponding kinetic energy, calculated by means of equation (5.3.1). In particular, the results regarding the horizontal longitudinal velocity profile at x = 0.89 m, z = 0.086 m and the vertical velocity profile at x = 0.89 m, y = 0.30 m are considered.

When evaluating the signal quality of the two series of experimental data, not only the mean representative value of SNR and correlation of the sample has been considered but also the local value associated with every sampling at 25 Hz.

Actually, the global behaviour of the measured data respects the threshold limits on SNR (15 dB) and on correlation (70%) almost everywhere (a mean correlation value equal to 69.5 % has been observed at the position closest with the jet axis) but this is not always true when the value of each measured data is considered.

The comparison among numerical results, original measured data and post-processed data, considering the filtering method A (corresponding to the procedure delineated in section 5.3.1) and the filtering method B (corresponding to the procedure delineated in section 5.3.2) for the horizontal and vertical longitudinal reference profiles are shown in Figure 7.14 and Figure 7.15.

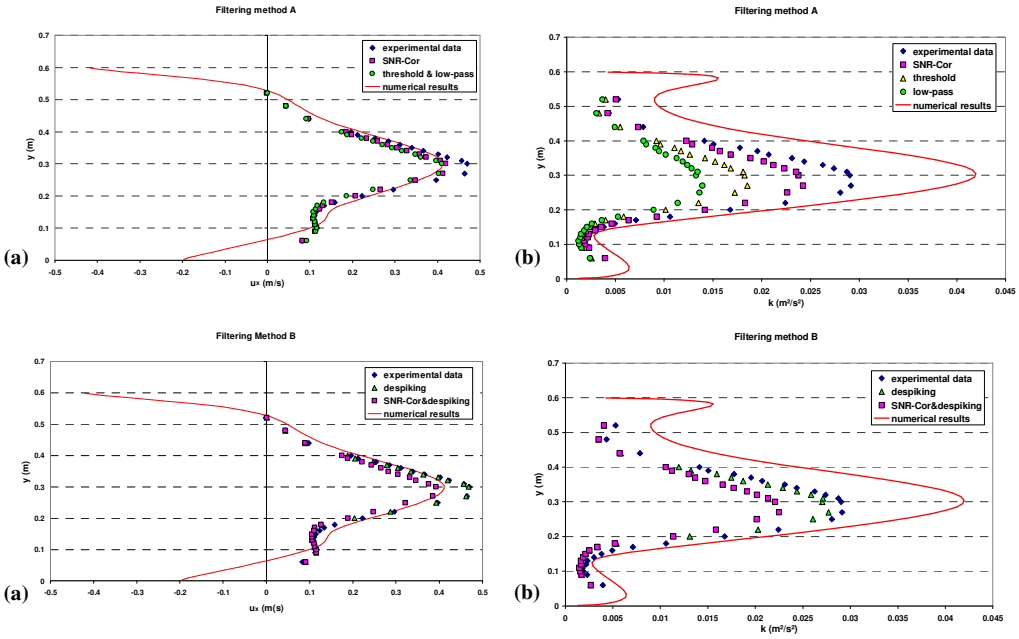

Figure 7.14 Signal filtering methods applied to the horizontal profile (x = 0.89 m, z = 0.086 m); (a) longitudinal velocity, (b) turbulent kinetic energy

Considering the results of the applied filtering methods, it can be noticed that, for both the filtering methods A and B, the elimination of under-quality velocity values due to low SNR and correlation (*SNR-Cor filter*), determines the decrease of the greatest velocity values.

About filtering method A, one can also note that a further slight reduction of the velocity mean values is due to the application of the filter based on the threshold method while the low-pass filter provides coincident results with the previous filtering step.

However, the outcome of the signal filtering methods is certainly more severe if one examines the turbulent kinetic energy profile where it can be seen that the numerical profile already overestimates the unfiltered one and that the

subsequent filtering steps, both for method A and B, lead to a greater reduction in the calculated values.

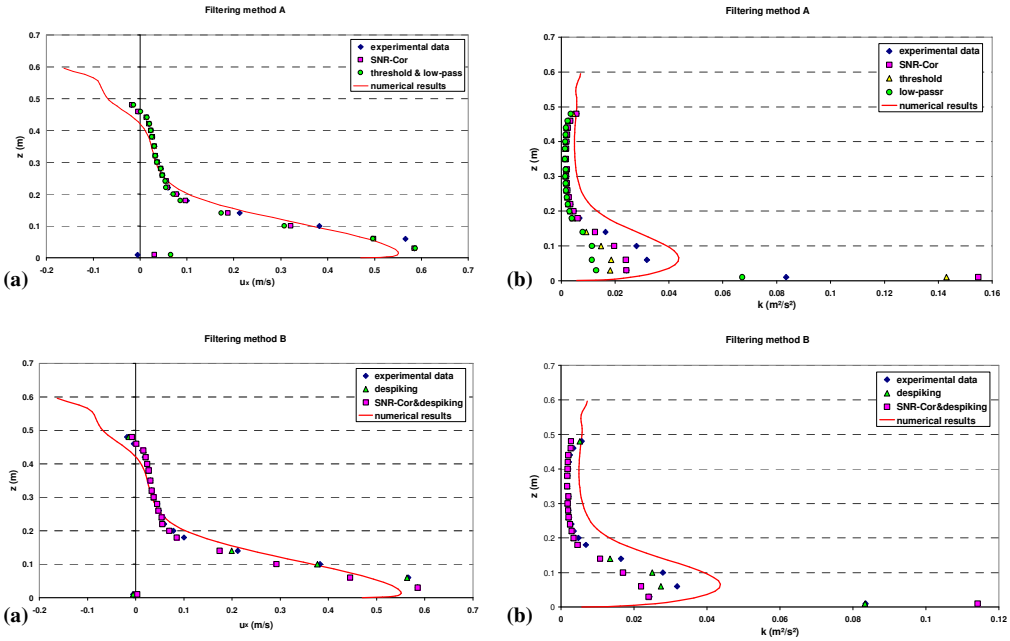

Figure 7.15 Signal filtering methods applied to the vertical profile (x = 0.89 m, y = 0.30 m); (a) longitudinal velocity, (b) turbulent kinetic energy

In particular, it can be noticed that the low-pass filter (in filtering method A) causes a remarkable reduction of the values of turbulent kinetic energy.

This result probably goes in the direction of the assumptions previously set out in commenting on the comparisons between experimental and numerical profiles of turbulent kinetic energy for case study 1. In fact, some doubts still arise about the adequacy of the ADV measurement frequency to assess the intensity of the local turbulence of the flow. The fact that the low-pass filter causes an important reduction in the significant value of the corresponding turbulent kinetic energy highlights the probable inadequacy of the sampling

frequency of the instrument for the reconstruction of the intensity of turbulent fluctuations that take place at the higher velocities, for which the major fluctuations in the correlation values are also recorded. This fact seems to find a confirmation when examining the results of the application of the low pass filter with a cutoff frequency equal to the half of the velocimeter sampling frequency (i.e 12.5 Hz) directly on the original experimental data. The horizontal kinetic energy profile at x=0.89 m and z=0.086 m showing the comparison between the values calculated from the raw signal and the calculated values after the filtering is given in Figure 7.16.

Even when considering the low-pass filter alone, a considerable decrease of the turbulent kinetic energy can be noticed, especially for the measurement points closest to the jet axis.

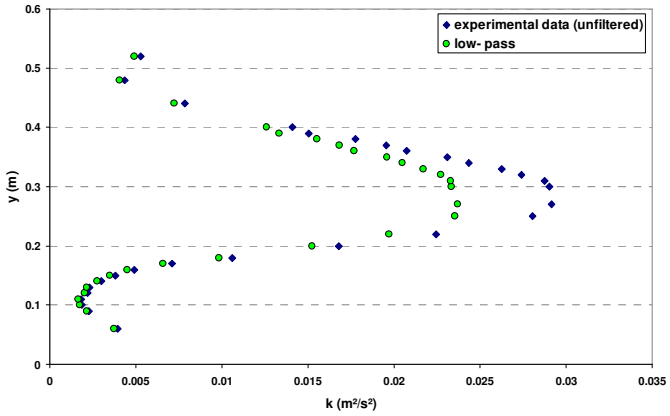

Figure 7.16 Turbulent kinetic energy horizontal profile(x=0.89 m, z=0.086 m) of unfiltered and low-pass filtered experimental data

In conclusion, it is not straightforward to determine what is the most suitable method for the signal processing and whether filtering out the SNR and correlation nasty values can be the best choice for the laboratory conditions here investigated. However, the obtained longitudinal mean velocity profiles show that the application of strict filters (SNR, correlation, threshold filter) does not result in an excessive variation of the average velocity. Consequently the

measuring instrument can be considered adequate for the estimation of the average velocity.

The comparison with velocity measurements at higher sampling frequency (e.g. 100 Hz) would be useful to draw more convincing conclusion about the behaviour of ADV in the determination of turbulent kinetic energy profiles.

Therefore, the numerical results were considered satisfactory compared with the experimental measurements, and the CFD velocity field was considered suitable to be used as input for the E-L model applied to the case study 2.

7.3.3 BSD determination

As mentioned in paragraph 5.4, an optical method was adopted to reconstruct the bubble size distribution.

The experimental set-up built to achieve the best operational conditions was determined after some preliminary tests. In order to achieve the best lighting conditions necessary to improve the image quality, 4 cold lights (500 W) placed above the tank and 2 neon lamps placed below the transparent bottom of the tank were used, ensuring a uniform light field and the best contrast level between the bubble contours and the background.

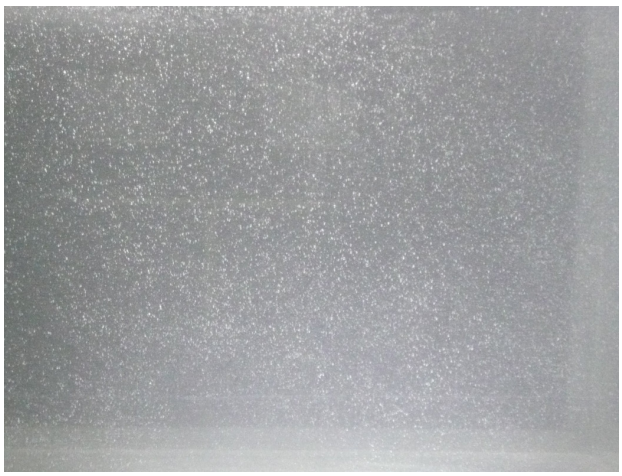

Figure 7.17 Lighting condition of the experimental setup for BSD determination

This arrangement was different from the procedure identified by other authors (Chigier, 1991; Honkanen, 2003) who consider the backlighting as the most proper illumination set-up. Unfortunately this configuration was shown to be unsatisfactory for the present experimental operational arrangement because raising of optical disturbance due to the light reflection on the wall of the tank occurred.

Bubble images were obtained by placing the digital camera at position x/D = 80, where the bubbly flow is well established and the velocity of the flow is just low enough to allow one to obtain clear snapshot of the bubbles motion. Eighteen images were taken at three different *xz* vertical planes: one passing through the axis of the turbulent jet (y=0.300 m) and other two at y=0.280 m and y=0.260 m.. These pictures, of mean size equal to 142x95 mm, illustrate only one half of the injected bubble flow but, assuming the bubble flow to be symmetric with respect to the *xz* plane passing through the axis of the turbulent jet, they are sufficient to describe the BSD of the entire bubble field. Moreover, varying the aperture values a Depth of Field (DOF) equal to 0.02 m was ensured. Exposure time between 1/800 and 1/2000 s was imposed and the sensibility of the CCD sensor was kept constant to 1600 ISO for each image.

7.3.3.1 BSD from manual detection

The first step that has characterized the determination of the bubble size distribution by manual detection has been the refinement of the method developed for the determination of the scaling factor necessary to convert the bubble size from pixels to millimetres. In particular, the extension of the depth of field was determined by evaluating the minimum and maximum distance of the in-focus test images, which have revealed that a DOF of 0.02 m is established. Moreover, it has been observed that this length extends 0.16 m behind the plane of focus and 0.04 m in front of it. Three different scaling factor were evaluated (for the plane of focus and for the two planes placed at the limit position of the in-focus region) and an average scaling factor were determined.

The influence of the optical disturbance due to the light reflection by the bubble surface was then evaluated. For the reason described inside paragraph 5.4.2, four different transparent crystal glass (soda-lime glass) spheres of diameter ranging from 1 to 4 mm were adopted in order to best simulate the characteristics of a gas bubble. The manufacturing of the product ensured a precision of ±0.01 mm of the sphere size. Appling the determined scaling factor (SF) to the detected diameter in pixel (Dpx) of in focus sphere images (Figure 7.18) and knowing the real sphere diameter (Ds) the error associated with the detection of each sphere ($\Delta D_{\%}$)has been found. The related results are listed in Table 7.2.

Table 7.2 shows that the greater detection error concerns the smaller bubbles; however, the magnitude of the error can be considered acceptable and therefore the optical detection method has been considered to be suitable for the determination of BSD as the input of the numerical model.

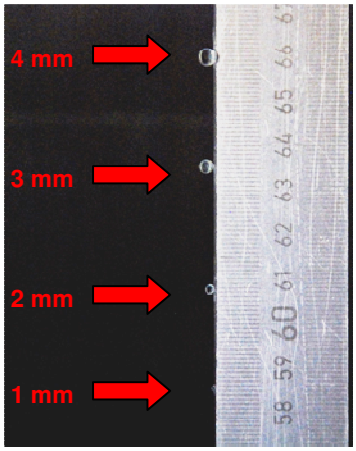

Figure 7.18 Crystal glass spheres used in order to validate the bubble detection method

Ds (mm)	Dpx (px)	SF (mm/px)	Dm (mm)	ΔD (mm)	$\Delta D_{\%}$ (%)
1.00±0.01	24	0.0392	0.941	-0.059	-6%
2.00±0.01	51.8	0.0392	2.030	0.030	2%
3.00±0.01	78.5	0.0392	3.077	0.077	3%
4.00±0.01	105	0.0392	4.115	0.115	3%

Table 7.2 Parameters of conversion of the sphere diameter from pixel to mm and related detection errors.

7.3.3.2 BSD from circular Hough transform

Adopting the semi-automatic method described in paragraph 5.4.1 to post-process the eighteen digital images, the BSD distribution describing the volume percentage p associated with each dimensional class d was calculated (as depicted inside Figure 7.19). A total number of 7009 bubbles was detected, with diameters ranging from 0.15 to 6 mm. The bubble mean diameter of the distribution d_{mean} (weighted mean diameter on the percentage volume of each dimensional class) has been found equal to 2.48 mm, while the standard deviation d_{sd} is 0.93 m.

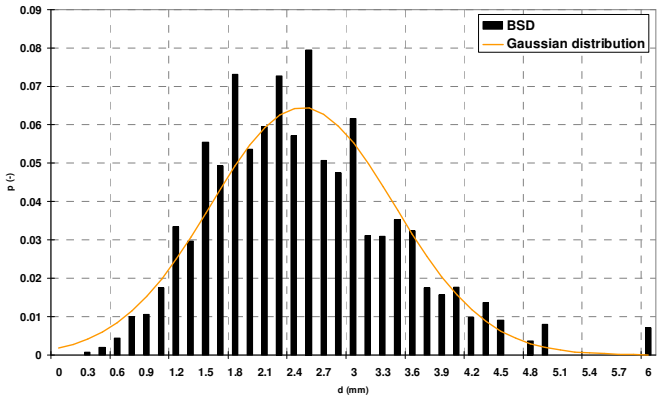

Figure 7.19 BSD derived from the application of the circular Hough transform compared with the correspondent Gaussian distribution

The statistical analysis of the distribution compared with the confidence intervals (*3-sigma rule*) of the Gaussian probability distribution is summarised in Table 7.3.

	$d_{mean}\pm d_{sd}$ (%)	$d_{mean}\pm 2d_{sd}$ (%)	$d_{mean}\pm 3d_{sd}$ (%)
BSD_Hough	75.7	96.9	99.2
Gaussian distribution	68.3	95.5	99.7

Table 7.3 Comparison of the BSD distribution derived from the application of the Hough transform with a Gaussian distribution

In order to limit the number of the dimensional classes given as input to the E-L model, a manipulation on the total number of the dimensional classes detected has been performed. A grouping procedure has been adopted by calculating a mean diameter of the dimensional classes added together until that their volume percentage did not reach the 5%. A definitive number of 18 classes of bubble with different diameters were considered.

The BSD derived from the manual detection method is instead shown inside Figure 7.20. The total number of bubbles recognized has been 6657 belonging to 346 different dimensional classes. The weighted mean diameter on the percentage volume of each dimensional class d_{mean} (equal to 2.28 mm) and the standard deviation of the sample d_{sd} (equal to 0.88 mm) have been used to calculate the confidence intervals $d_{mean}\pm\alpha d_{sd}$ (with α ranging from 1 to 3). The comparison of the calculated values with the characteristics confidence intervals of a Gaussian distribution is reported inside Table 7.4.

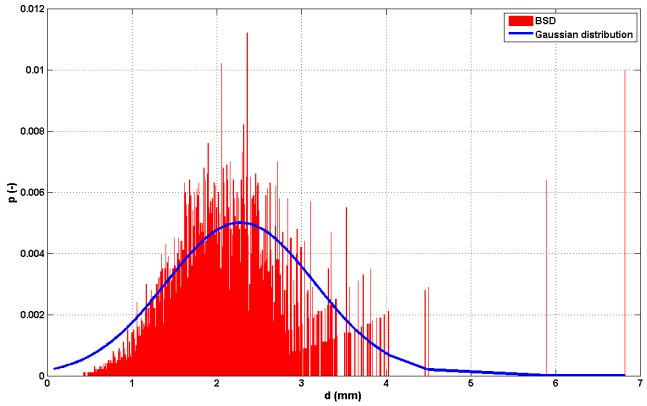

Figure 7.20 BSD derived from the application of the manual detection method compared with the correspondent Gaussian distribution

	$d_{mean}\pm d_{sd}$ (%)	$d_{mean}\pm 2d_{sd}$ (%)	$d_{mean}\pm 3d_{sd}$ (%)
BSD	77.8	97.7	98.4
Gaussian distribution	68.3	95.5	99.7

Table 7.4 Comparison of the BSD distribution derived from the manual detection method with a Gaussian distribution

The detected BSD has been elaborated in order to obtain a size distribution suitable to be used as input for the numerical model. To this end, the Sauter mean diameter (d_{Sauter}) of the distribution has been firstly calculated. The Sauter mean diameter is a representative diameter often used to characterize the size distribution, calculated through the relation:

$$d_{Sauter} = \frac{\sum_{i=1}^{N} d_i^3}{\sum_{i=1}^{N} d_i^2} \tag{7.3.1}$$

where N is the total number of bubbles.

The Sauter mean diameter ($d_{\_Sauter}$) was considered a reference diameter for the subdivision of the bubble distribution on logarithmic basis. Ten dimensional classes in the range d_{min}-$d_{\_Sauter}$ (d_{min} = minimum diameter of the bubble size distribution)and ten classes in the range $d_{\_Sauter}$-d_{max} (d_{max} = maximum diameter of the bubble size distribution) were calculated. The volume percentage p of bubbles that fall between the extremes and a mean diameter for each designed interval were determined. The only exception made concerned the dimensional class with the larger diameter, inside which a single bubble fell. For this reason, the diameter of the greatest measured bubble has been directly attributed to the last interval. In addition, no bubbles belonging to the nineteen dimensional class were found.

The final bubble size distribution obtained and used as input for the numerical model is shown in Figure 7.21.

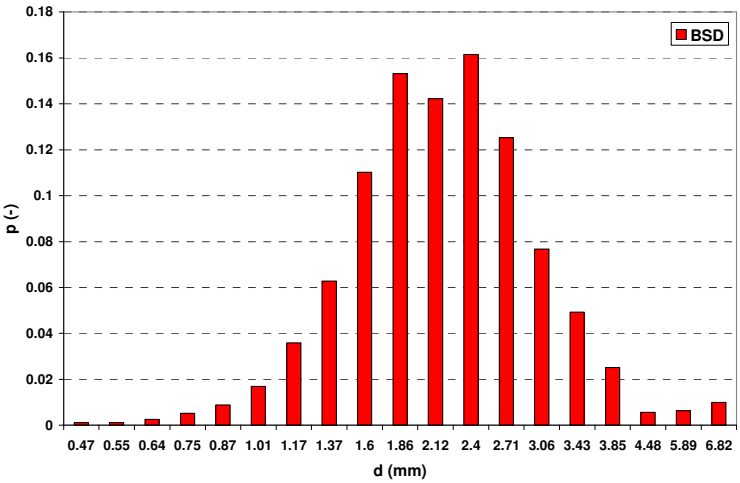

Figure 7.21 Final BSD used as input of the E–L model

A comparison between the characteristic dimensional distribution of bubbles obtained from the manual detection method (*BSD*) and the bubble size

distribution obtained from the semi-automatic detection method (*BSD_Hough*) is given in Figure 7.22

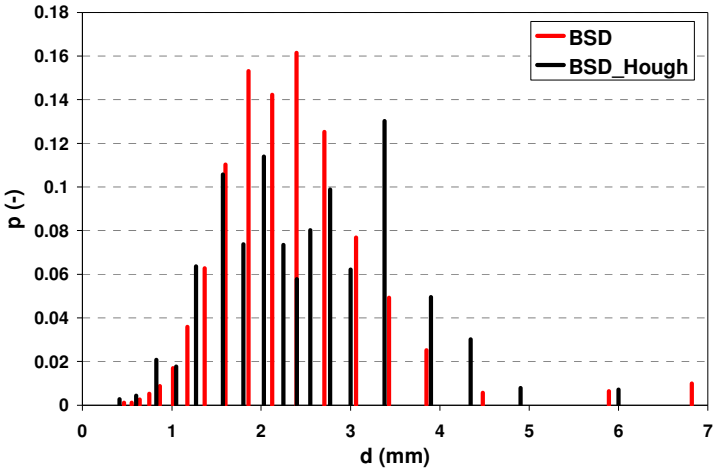

Figure 7.22 Comparison between the final BSD obtained through the manual detection method (BSD) and the BSD obtained by means of the semi-automatic method (BSD_Hough)

7.4 Dissolved oxygen measurements

In order to perform the validation of the developed E-L model, experimental measurements of dissolved oxygen concentration were carried out during laboratory oxygenation tests.

The oxygenation has been carried out until the equilibrium conditions in the tank were reached. After a period of 8000 seconds the concentrations inside the tank were very near the equilibrium value, but the concentration field during the oxygenation test has been monitored studied for a longer time (about 6 hours for the case study and 4 hours for the case study 2).

A deoxygenation of the oversaturated liquid volume has been followed too, in order to obtain the needed number of points for the calculation of the overall mass transfer coefficient ($k_l a$) as described in section 4.3.2.4.2. During the deoxygenation test the mixing system has been kept working.

During the test run, the same gas flow rate and the same operating conditions of the jet-pump system that characterized the earlier experimental stages were kept.

At the same time with the measurement of dissolved oxygen concentration, the temperature inside the tank has been monitored. An average temperature of 20° C was recorded during the oxygenation test of case study 1, while a mean temperature of 25° C characterized the case study 2.

The dissolved oxygen concentration measurement was performed by means of a portable galvanic dissolved oxygen meter (Oxi 330/SET), whose operating principle is based on redox reactions that involve an electrolytic solution were a pair of electrode are located. Electrode and controlectrode are separated from the sample by means of a gas-permeable membrane. The working electrode reduces the oxygen molecules to hydroxide developing an electrical current that flows from the working electrode to the controelectrode. The intensity of the produced signal is proportional to the dissolved oxygen concentration in the sample.

The measurement error within the operational measurement range is estimated as the 0.5% of the measured DO concentration value.

Several points inside the tank were monitored during the experimental procedure. The localisation of the monitoring points of case study 1 is shown in Figure 7.23.

An example of the oxygenation and deoxygentaion curves obtained for the monitoring points 6 and 4 is shown in Figure 7.24.

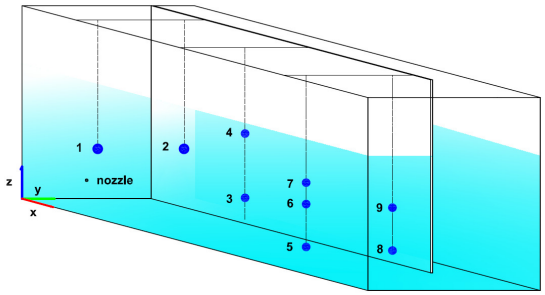

Point	Position (x,y,z) (m)
1	0.4,0.1,0.3
2	0.4,0.5,0.3
3	0.9,0.3,0.2
4	0.9,0.3,0.5
5	1.4,0.1,0.1
6	1.4,0.1,0.3
7	1.4,0.1,0.4
8	1.4,0.5,0.1
9	1.4,0.5,0.3

Figure 7.23 Localisation of the DO measurement points for case study 1

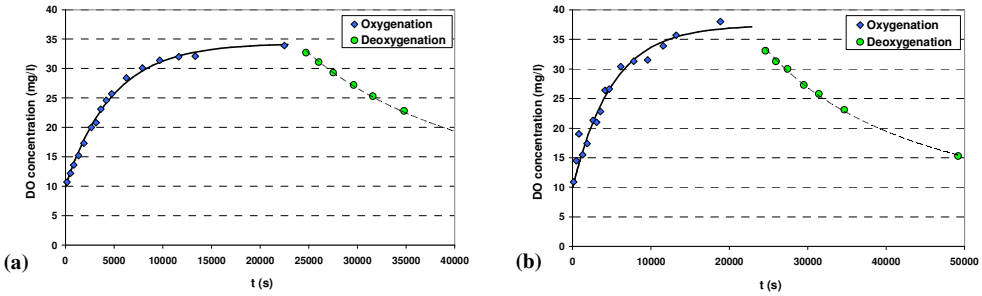

Figure 7.24 Oxygenation and deoxygenation curves for case study 1; (a) Point 6, (b) Point 4

The point 6 is located far downstream the jet nozzle within a lateral region slightly interested by the bubbly flow and characterized by lower velocities if compared with point 4, located instead inside a zone directly involved by the bubbly flow and characterized by higher velocity. The different position occupied by the measurement points can be noticed looking at the greater variability of the dissolved oxygen measures in correspondence of the point 4, while the point 6 shows a more uniform trend. The oscillation of the

experimental measurements observed at point 4 it is possibly due to the fact that some bubbles remain on the membrane of the dissolved oxygen meter leading to an inaccurate final measured value.

In order to minimize the interference of the measuring procedure on the dissolved oxygen concentration field, only three measurement positions were considered for the case study 2. The location of the measurement points is listed in Figure 7.25. In Figure 7.26 the oxygenation and deoxygenation curves relative to the measurement points 1b and 3b are depicted. It can be noticed that the final equilibrium concentration reached at point 1b (downstream the transversal baffle) is only slightly lower than that upstream the partitioning wall.

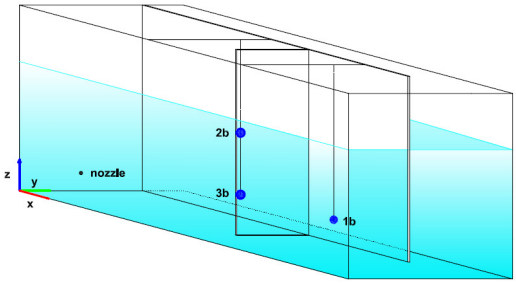

Point	Position (x,y,z) (m)
1b	1.12,0.45,0.15
2b	0.65,0.45,0.45
3b	0.65,0.15,0.15

Figure 7.25 Localisation of the DO measurement points for case study 2

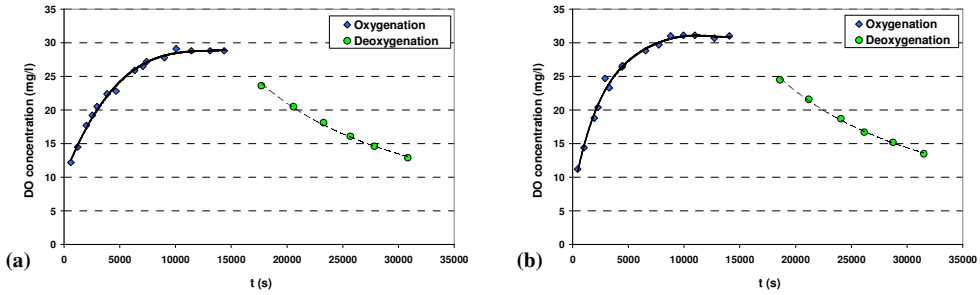

Figure 7.26 Oxygenation and deoxygenation curves for case study 2; (a) Point 1b, (b) Point 3b

7.5 Discussion of the results

The ability of the developed numerical model to describe the DO concentration evolution in time is evaluated by simulating the described laboratory test cases. The liquid velocity field determined as described in paragraph 7.3.1 and 7.3.2, for the case study 1 and 2 respectively, and the BSD determined as proposed in paragraph 7.3.3.1 are used as input for the E-L model. The final results are then compared with the DO measurements at some of the points individuated inside paragraph 7.4.

The computational domain of the E-L model of each case study has been considered as a parallelepiped of dimension 1.66 m x 0.6 m x 0.6 m, hence the part of the tank behind the jet nozzle has been truncated. The size of the cells of the computational grid for the dissolved oxygen concentration has been set equal to the one of the computational grid for bubble dynamics (0.01 m x 0.01 m x 0.01 m)

7.5.1 Numerical simulation of DO concentration: case study 1

A snapshot of the bubble motion inside the tank of case study 1 after few seconds of calculation is shown in Figure 7.27. It can be observed that, consistently with observations, the bubbles with larger diameters move upwards just downstream the nozzle exit, while the smaller are transported by the liquid flow.

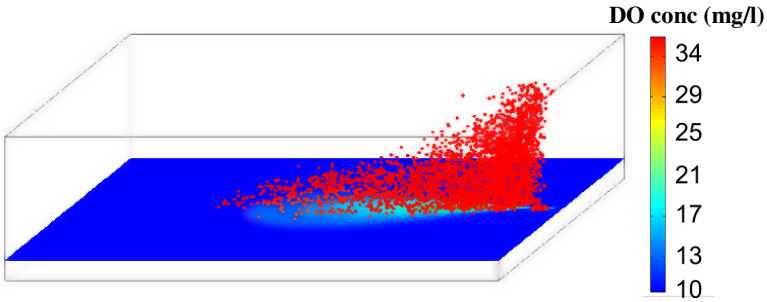

Figure 7.27 Snapshot of bubble motion and of the DO concentration at the nozzle elevation

During the evaluation of the numerical results regarding the case study 1, two main aspects were identified as the most significant to affect the expected results: the transfer model implemented to represent the source term concerning the mass transfer from the bubbles to the liquid phase and the BSD provided as input. For this reason, for the case study 1 a sensitivity analysis has been conducted on them.

The influence on the dissolved oxygen concentration of the uncertainty in the determination of the gas flow rate and on the refinement of the computational grid for the numerical solution of the concentration equation have been also evaluated.

7.5.1.1 Sensitivity analysis on mass transfer model

The influence of the model adopted to describe the mass transfer from the bubble to the surrounding liquid has been evaluated by implementing eight different relations for the mass transfer coefficient (k_L) of equation (4.3.10). A detailed description of the relations used is reported in the following.

The influence of each model adopted on the predicted dissolved oxygen concentration evolution in time is considered either for the monitoring points 4 and 6.

The discussion and comparison between the results are intended to highlight both the differences arising from the application of the mass transfer models which are distant from a conceptual point of view and the differences and variations which derive by adopting the same kind of mass transfer model.

- *Transfer model 1: Ahmed and Semmens + Higbie (tm1)*

The mass transfer model has been evaluated considering two different transfer models based on the "slip velocity models" as described in paragraph 2.1.2.4. In particular, the relation (2.1.27) proposed by Ahmed and Semmens (2003) has been used for bubbles with diameter lower than 1.5 mm, while the

standard Higbie's theory (2.1.23) has been applied to gas bubbles having diameter higher than 1.5 mm, for which the exposure time, t_e, has been evaluated considering the rise velocity of the bubble V as $t_e = d/V$

The threshold on the bubble diameter has been selected after the evaluation of some simulation results and considering that, as discussed in paragraph 2.1.2.4, the diameter from which a bubble stops to behave as one with a mobile surface and begins to behave like a rigid sphere is not of easy determination, but depends on the concentration of contaminants within the water.

- *Transfer model 2: Eddy model c=0.72 (tm2)*

The mass transfer model implemented belongs to the "eddy models" since the relation used to define the mass transfer coefficient, k_l, considers the equation (2.1.25). The value 0.72 has been considered for the coefficient c. This value appears to be reasonable since it falls within the range of values given in the literature (1.12 – 0.4) as previously discussed in paragraph 2.1.2.4.

- *Transfer model 3: Higbie model (tm3)*

The mass transfer coefficient implemented in the code has been calculated using the relation given by Higbie's penetration theory (equation (2.1.23)) in its classical formulation, where the exposure time of the bubble, t_e, has been evaluated as the ratio between the bubble diameter and the bubble rise velocity.

So each bubble has been considered as having a mobile surface and no differentiation has been made for bubbles with small diameter.

- *Transfer model 4: Eddy model (Prasher and Wills) (tm4)*

The mass transfer coefficient has been evaluated by means of equation (2.1.25) but, differently from transfer model *tm2*, the value attributed to the

constant c was the value identified by Prasher and Wills (1973) for a stirred tank reactor (c = 0.592).

- *Transfer model 5: Eddy model c=0.72/Higbie (tm5)*

The mass transfer coefficient has been evaluated considering the exposure time t_e as the minimum value between the exposure time indicated by Higbie himself (the ratio between the bubble diameter and the bubble rise velocity) and the exposure time of a "eddy model" (the square root of the ratio between the kinematic viscosity of the liquid and the turbulence dissipation rate).

If the resulting minimum value was corresponding to the standard Higbie's relation, the equation (2.1.23) was then applied, otherwise relation (2.1.25) was considered, taking into account a value of 0.72 for the coefficient c.

- *Transfer model 6: Motarjemi and Jameson + Higbie (tm6)*

Two different relations were adopted to describe the mass transfer coefficient depending on the bubble diameter. For bubbles having diameter lower than 2 mm an interpolating relation was used, which has been evaluated by considering the experimental results reported by Motarjemi and Jameson (1978) and shown inside Figure 2.5. For bubbles with diameter greater than 2 mm the standard Higbie penetration theory was adopted.

The threshold value of 2 mm has been chosen by observing the behaviour of the experimental data reported in Figure 2.5, where a change in the trend of the experimental data can be noticed for a bubble diameter equal to 2 mm.

- *Transfer model 7: Frossling + Higbie (tm7)*

The mass transfer coefficient has been evaluated with the Frossling relation (equation (2.1.26)) for bubbles having diameter lower than 1.5 mm and with the standard Higbie's penetration theory for bubbles with diameter greater than 1.5 mm.

This transfer model was selected in order to allow a comparison with the *tm1* model and then to evaluate the effect of using the classical relation of Frossling (1938) than the one recently proposed by Ahmed and Semmens (2003).

- *Transfer model 8: Eddy model c=0.72 + Frossling + Higbie (tm8)*

The mass transfer coefficient has been evaluated by imposing a threshold value on the turbulent dissipation rate of the flow rather than the threshold value imposed on the bubble diameter used for *tm1*, *tm6* and *tm7* model.

In particular, if the turbulent dissipation rate of the computational cell occupied by the bubble is higher than 0.1 m^2/s^3 the relation (2.1.25) was applied imposing $c = 0.72$, otherwise the transfer model *tm7* was considered to perform the calculation of the mass transfer coefficient.

The threshold value on the turbulent dissipation rate has been selected after some analysis and considering the concluding remarks of Alves et al. (2006) discussed inside paragraph 2.1.2.4.

The comparison between the simulation results obtained by considering the mass transfer model from the oxygen bubbles as calculated by means of the Higbie standard penetration theory (*tm3*) and the results concerning the implementation of the eddy cell model as proposed by Prasher and Wills (1973) (*tm4*) is shown in Figure 7.28.

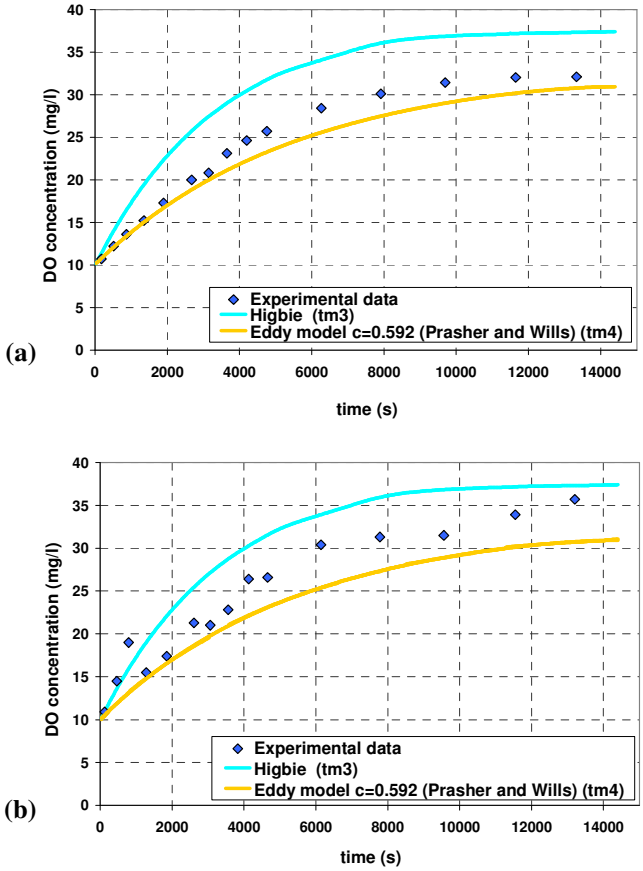

Figure 7.28 Sensitivity analysis on mass transfer model: comparison between DO measurements (diamond markers) and numerical results relative to *tm3* and *tm4* models (continuous line), (a) Point 6, (b) Point 4

It can be noticed that none of them is able to predict the behaviour of the experiments sufficiently well. The classical Higbie's penetration model without any differentiation in the treatment of bubbles of small size leads to a clear overestimation of the measurements, while *tm4* model which involves the turbulence dissipation rate of the liquid flow to calculate the bubble exposure

time leads to an underestimation of the amount of oxygen transferred from the bubbles to the surrounding liquid.

The effects on the evolution of the dissolved oxygen concentration due to the adoption of different mass transfer models which consider a differentiation based on the diameter owned by the bubbles for the calculation of the mass transfer coefficient are shown in Figure 7.29. First, it can be noted that the comparison with the original model of Higbie reveals that a significant improvement in the prediction of the experimental results is introduced for any considered transfer model with a threshold on bubble diameter.

In particular, the mass transfer model based on Ahmed and Semmens relation for bubbles smaller than 1.5 mm (*tm1*) leads to the nearest estimation of the dissolved oxygen measurements, especially for the monitoring point located far downstream the jet exit (Point 6). Using the Frossling relation instead of the Ahmed and Semmens one (*tm7*) no such relevant variation on the total amount of the transferred oxygen can be noticed, even if the *tm7* model leads to a little increase of the dissolved oxygen contents inside the tank. The mass transfer model based on the relation determined by the interpolation of the experimental data of Motarjemi and Jameson for bubbles lower than 2 mm, leads to an overestimation of the oxygen transferred into the system.

It can be observed that the imposition of a lower threshold value on the bubble diameter leads generally to an increase of the oxygen transferred from the bubbles to the surrounding liquid phase. Actually, this effect is the results of two interrelated issues. The first one concerns with the fact that the mass transfer coefficient predicted by the Higbie model (or more generally a model for bubbles with mobile surface) is greater than the one calculated by means of a mass transfer relation for bubbles with rigid surface, hence the global oxygen transfer is higher. The second issue regards the fact that the smallest bubbles persist inside the system for a longer period of time and so does the transfer of oxygen from them. This phenomena will be highlighted more deeply inside the following section 7.5.1.2.

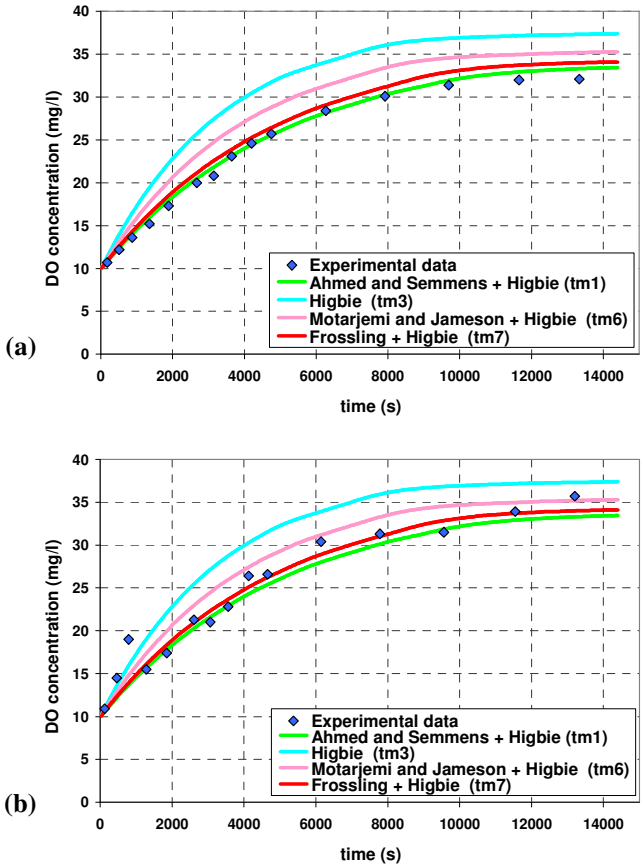

Figure 7.29 Sensitivity analysis on mass transfer model: comparison between DO measurements (diamond markers) and numerical results relative to *tm1*, *tm3*, *tm6* and *tm7* models (continuous line), (a) Point 6, (b) Point 4

The comparison between the two "eddy models" considered for the sensitivity analysis (i.e. *tm2* and *tm4* models) is proposed inside Figure 7.30. It can be noticed that the mass transfer model characterized by the higher value of the coefficient c of equation (2.1.25) describes best the trend of the experimental data.

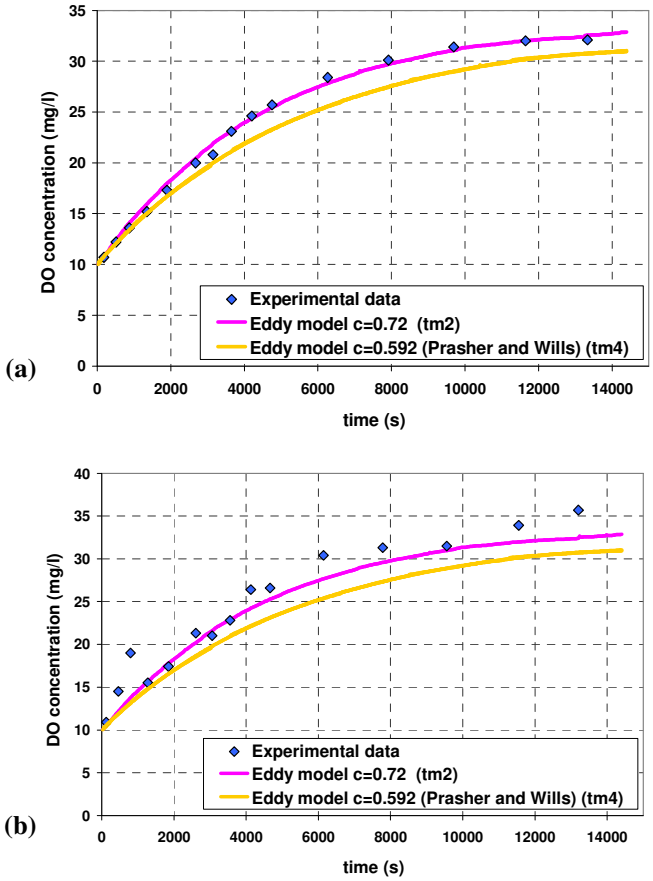

Figure 7.30 Sensitivity analysis on mass transfer model: comparison between DO measurements (diamond markers) and numerical results relative to *tm2* and *tm4* models (continuous line), (a) Point 6, (b) Point 4

This result indirectly highlights that if the value 1.13 is attributed to c, the resulting curves will overestimate the DO concentrations reached in the system. So, by considering the standard Higbie model where the exposure time is calculated as proposed by the eddy type models, it leads to an incorrect prediction of the oxygen concentration evolution.

Considering the mass transfer models implemented in the code, it can be noticed that *tm1* and *tm2* models seem the most adequate to evaluate the dissolved oxygen concentration inside the tank, especially for the measurement point 6, while for the monitoring point 4 also the *tm7* transfer model presents a good agreement with the experimental measurements.

The fact that two conceptually different mass transfer models both lead to satisfactory results (*tm1* and *tm2* models) has been further investigated. In the first instance, the inaccuracy made in considering a transfer model that evaluates the exposure time of the bubble as the lesser between the time provided by the classical theory of Higbie and the one based only on the characteristics of turbulent flow field (*tm5*) has been assessed. The result has been completely unsatisfactory, as it yielded the maximum overestimation of the dissolved oxygen concentration among all the mass transfer models considered.

Considering the work of Alves et al. (2006), and having already seen how the use of Higbie's model (*tm3*) leads to an overestimation of the mass transfer, the possibility of identifying a threshold such that the characteristics of the flow field begin to prevail on the characteristics of the transfer based on the dimensional characteristics of the bubbles has been researched (*tm8*).

The comparison among the mass transfer model *tm2*, *tm5* and *tm8* is shown in Figure 7.31. The research of this "limit" value would probably require further investigation by the experimental point of view.

In fact, considering a threshold on the turbulence dissipation rate slightly higher than that indicated by the authors (Alves et al., 2006), an overestimation of the oxygen mass transfer in the tank still occurs. The individuation of the separation value is complicated by the fact that with a lower threshold value, the percentage of computational cells for which the k_l coefficient depends on the turbulent dissipation rate increases, consequently the corresponding exposure time is higher, but the dissolved oxygen concentration may be higher, due to the

fact that the transfer is also influenced by the number and the dimension of the bubbles that occupy a given cell.

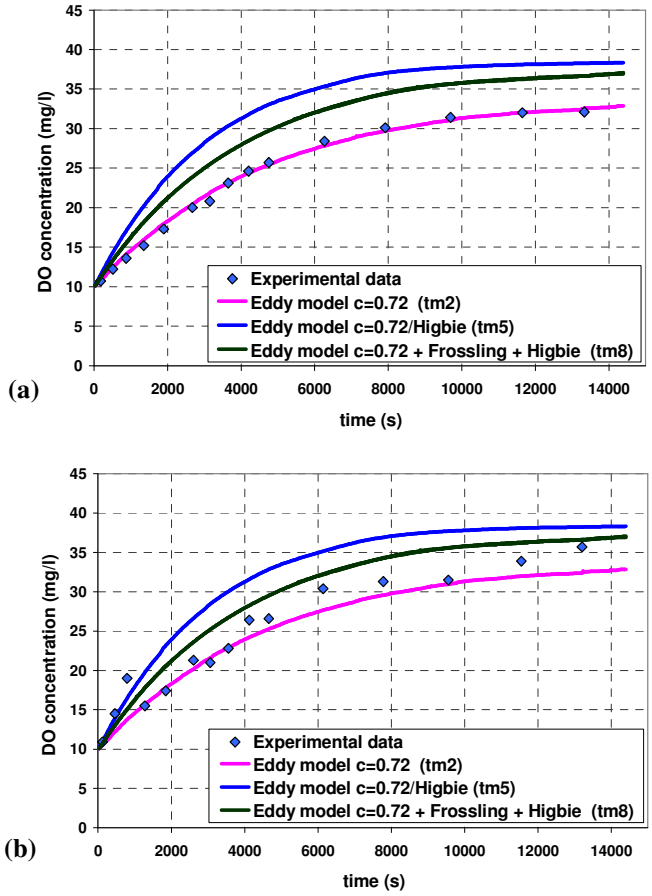

Figure 7.31 Sensitivity analysis on mass transfer model: comparison between DO measurements (diamond markers) and numerical results relative to tm2, tm5 and tm8 models (continuous line), (a) Point 6, (b) Point 4

7.5.1.2 Sensitivity analysis on BSD and bubble mean diameter

The effects of the bubble size distribution given as input to the E-L numerical model have been evaluated by means of a sensitivity analysis carried out by comparing the results obtained using the BSD distribution calculated in section 7.3.3.1 considering the mass transfer models *tm1* and *tm2* (section 7.5.1.1) with five different dimensional distributions of bubbles. A description of each BSD distribution adopted is given in the following.

- *Mean diameter weighted on the bubble volume percentage (d_mean)*

A BSD distribution constituted of a single dimensional class with the mean diameter d_{mean}:

$$d_{mean} = \sum_{i=1}^{N} p_i d_i \tag{7.5.1}$$

has been considered, where d_i is the diameter of the *i-th* bubble of the distribution, p_i is its volume fraction and N is the total number of bubbles. The value of d_{mean} computed on the reference BSD was equal to 2.28 mm.

- *Sauter mean diameter (d_Sauter)*

The Sauter mean diameter calculated by means of equation (7.3.1) has been attributed to a single dimensional class considered as representative of the entire BSD. The Sauter mean diameter computed on the reference BSD was equal to 1.99 mm.

- *BSD distribution obtained through the semi-automatic method (BSD_Hough)*

The BSD distribution obtained from the semi-automatic detection method - which involves as a crucial step the application of the circular Hough transform algorithm (see section 5.4.1) - has been considered. The BSD distribution given as input at the E-L model presents the characteristics described in paragraph 7.3.3.2.

- *BSD translated towards high diameters (BSD_p)*

The dimensional distribution has been calculated in a similar manner to that observed in section 7.3.3.1. The reference diameter (d_{ref}) considered in order to arrange the dimensional classes has been considered 1.5 times the Sauter mean diameter (equation (7.3.1)). Ten dimensional classes were then calculated on logarithmic basis both in the range d_{ref}-d_{max} (d_{max} = maximum bubble diameter of the distribution) and in the range d_{min}-d_{ref} (d_{min} = minimum bubble diameter of the distribution). Then, the mean diameter between the extremes of each dimensional class has been calculated and assigned to the dimensional class. Finally, the same volume fraction (p) determined for each class of the original distribution (BSD) has been attributed to the translated distribution. The resulting dimensional distribution (*BSD_p*) is shown in Figure 7.32(a).

- *BSD translated towards low diameters (BSD_m)*

The same procedure adopted to calculate *BSD_p* has been considered, but the reference diameter adopted has been assumed equal to 0.5 times the Sauter mean diameter. The bubble size distribution translated towards small diameters (*BSD_m*) is represented in Figure 7.32(b).

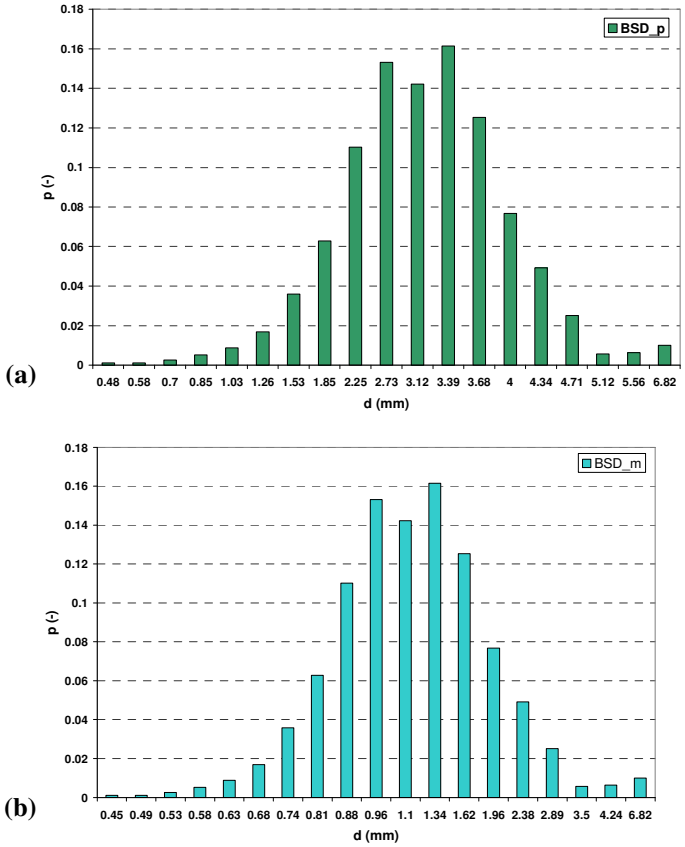

Figure 7.32 (a) BSD translated towards high diameters (BSD_p) , (b) BSD translated towards low diameters (BSD_m)

The results concerning the sensitivity analysis on BSD considering the mass transfer models *tm1* and *tm2* are shown in

Figure 7.33 and

Figure 7.34 respectively. Both the monitoring points 4 and 6 are considered.

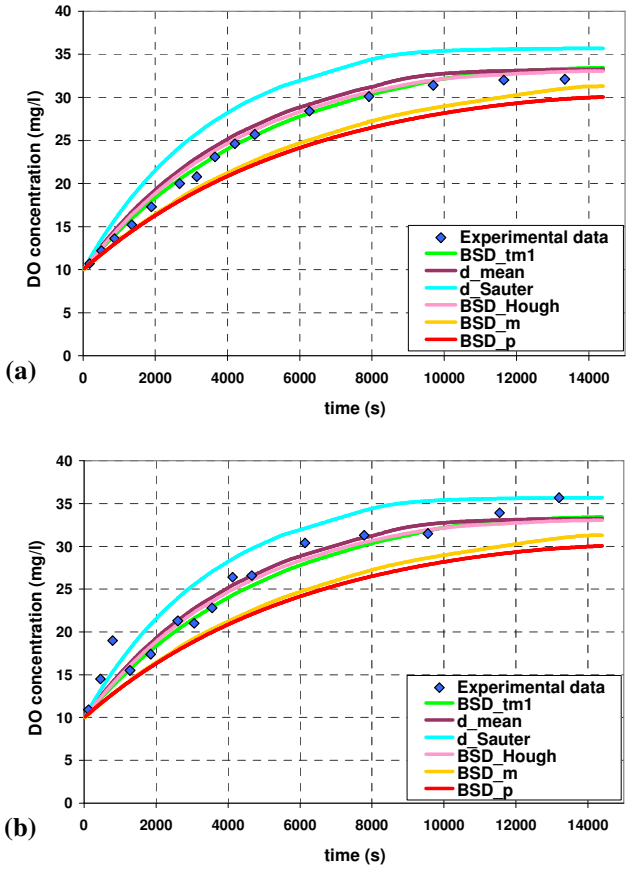

Figure 7.33 Sensitivity analysis on BSD with *tm1* model: comparison between DO measurements (diamond markers) and numerical results (continuous line), (a) Point 6, (b) Point 4

Despite the fact that non appreciable differences subsist between the two monitoring points considering the same mass transfer model, a substantial difference can be noticed by comparing the trend of curves related to mass transfer models *tm1* and *tm2*. The first macroscopic difference is related to the quite similar behaviour of BSD distributions *BSD_m* and *BSD_p* for the mass

transfer model *tm1*, while their behaviour is completely different when adopting the *tm2* model.

This difference can be ascribed to the fact that *tm1* model limits the mass transfer for small bubbles (less than 1.5 mm) since it makes use of the Ahmed and Semmens (2003) relation (2.1.27). So, small bubbles remain inside the tank for long periods of time but their mass transfer is limited (*BSD_m* curve). On the other hand, large bubbles (*BSD_p* curves) can transfer a lot of oxygen but their permanence inside the tank is smaller. Hence the two effects tend to balance each other.

It can be noticed that the BSD characterized by the *d_Sauter* diameter transfers more if compared with the one that considers the *d_mean* diameter.

The reason can be attributed to the fact that the Sauter diameter is, in this case, greater than the threshold value of 1.5 mm consequently, for most of the bubbles within the system, the Higbie's relation (2.1.23) is used. Moreover the diameter is smaller than the mean one, so the bubble population characterized by it spends a longer period of time within the tank leading to a greater oxygen transfer.

Considering the mass transfer model *tm2*, the greater transfer occurs for the size distribution shifted toward smaller diameters (BSD_m), as shown in

Figure 7.34. The motivation can be due to the fact that small bubbles remain in the system for longer periods of time and since no threshold value on mass transfer coefficient is defined on the basis of the bubble diameter, the highest dissolved oxygen concentration is achieved by them.

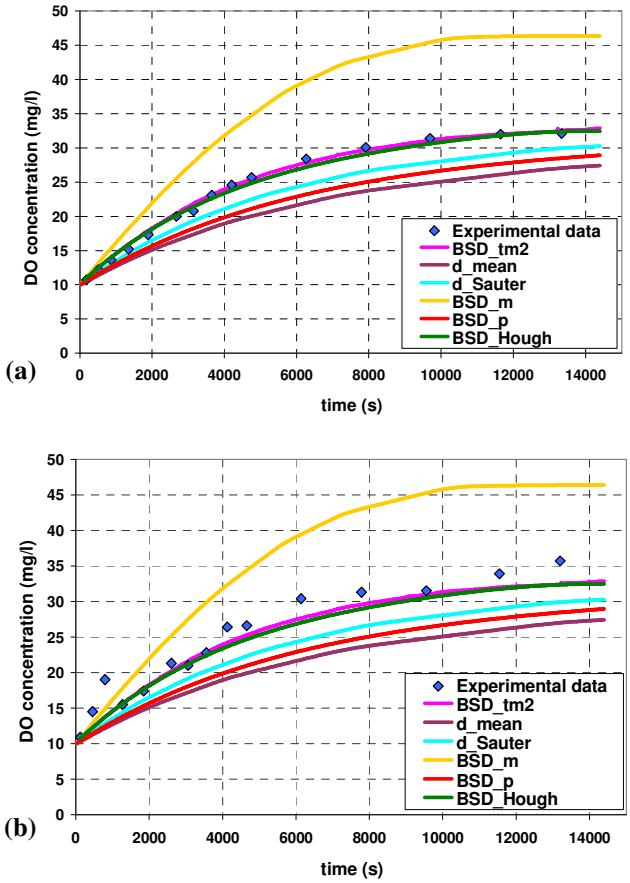

Figure 7.34 Sensitivity analysis on BSD with *tm2* model: comparison between DO measurements (diamond markers) and numerical results (continuous line), (a) Point 6, (b) Point 4

The distribution characterized by the Sauter one transfers a larger amount of oxygen compared to the one characterized by the mean diameter. Less obvious is the justification of the tendency of the curve *BSD_p* which is located at an intermediate position between the curves involving a single representative diameter of the entire BSD. Probably the amount of small bubbles inside the

system, although low in percentage terms, allows a greater oxygen transfer than the distribution defined on the single mean diameter.

Finally, it can be noticed that for both of the transfer models *tm1* and *tm2* adopting the BSD distribution obtained through the semi-automatic method (BSD_Hough) subsists a really great agreement with the experimental data. Looking at Figure 7.33 and Figure 7.34 it can also be noticed the good agreement of the BSD_Hough curves with those obtained considering as input for the E-L model the BSD obtained by means of the manual detection method. This means that despite some differences between the two distributions, the overall behaviour of the two is very similar to each other and thus that the semi-automatic method can be considered as a reliable procedure for the evaluation of the bubble size distribution.

7.5.1.3 Sensitivity analysis on gas flow rate

The effects of the overestimation and of the underestimation of the gas flow rate on the simulated dissolved oxygen concentration over time have been evaluated. The original BSD and the mass transfer model *tm1* have been considered for the two analysis.

The lower gas flow rate (*Q_m*) has been imposed equal to 0.5 times the measured gas flow rate (Q_g), while the greater gas flow rate (*Q_p*) has been calculated as 1.5 times Q_g..

The results are presented inside Figure 7.35, where it can be seen that, as expected, a greater gas flow rate corresponds to a greater dissolved oxygen concentration transferred from the bubbles to the surrounding environment. Anyway, it can be noticed that the increase in the dissolved oxygen concentration doesn't follow a linear relation, since the underestimation of the gas flow rate leads to a greater absolute error with respect to BSD_tm1 curve than the overestimation does.

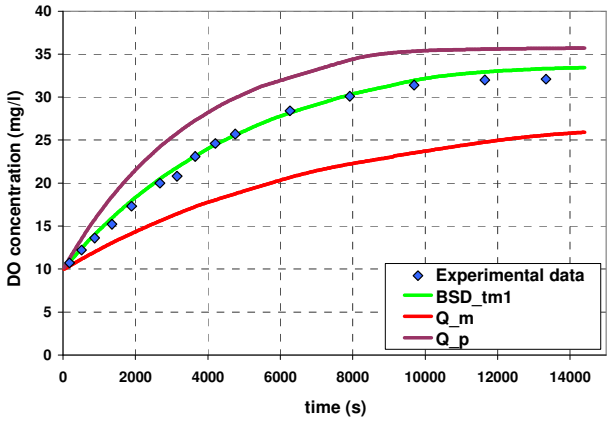

Figure 7.35 Sensitivity analysis on gas flow rate, comparison between DO measurements (diamond markers) and numerical results (continuous line)

7.5.1.4 Effects due to a coarser computational grid for concentrations

A computational grid for concentrations made up of cells of dimensions twice larger than those considered for the previous sensitivity analysis has been adopted in order to evaluate the errors that have to be paid to gain a reduction of the computational efforts. To this end, only the effects due to the lower spatial discretization have been considered by imposing the same time step of the previous simulations. This choice allows a reduction of about 1/8 of the calculation times (instead of about 1/16), however, the uncertainty associated with the slightly different trajectory followed by the bubbles is excluded.

The original BSD and the mass transfer model *tm1* have been considered for the comparison between the reference case (*BSD_tm1*) and the results of the coarser grid for concentrations (*BSD_tm1_coarse*).

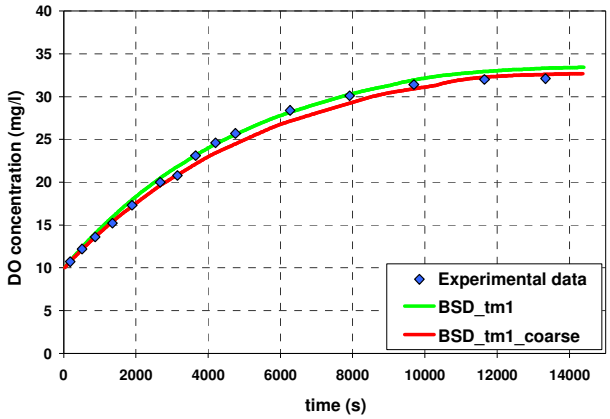

Figure 7.36 Effects due to a coarser grid for concentrations, comparison between DO measurements (diamond markers) and numerical results (continuous line)

A slight underestimation of the DO concentration during the four hours of calculation can be noticed by observing Figure 7.36. The reason of this shift may be attributed to the unavoidable coarser identification of the outlet/inlet boundary areas on the computational grid for concentrations. However, the results obtained with the coarse mesh appear to be satisfactory.

7.5.2 Numerical simulation of DO concentration: case study 2

The modification of the computer code in order to permit the modelling of the presence of a partitioning wall inside the computational domain has been carried out.

In particular, a small domain approach has been adopted by separating the computational domain in three different zones (upward, downward and lateral with respect to the partitioning wall) and by solving the partial differential equation of DO concentration in these zones separately with appropriate boundary conditions and interface conditions between the different blocks of cells.

The values of physical parameters such as water and gas densities, Henry constant, oxygen diffusivity, etc. have been updated to the new environmental conditions, since the water temperature was of 25°C during the oxygenation test (instead of 20°C registered for case study 1).

Although an extensive recirculation region has been detected (see Figure 7.11), the test case was not able to yield meaningful concentration gradients in space an almost uniform concentration field both upstream and downstream of the partitioning wall can be observed.

A snapshot of the bubble motion inside the tank after 6000s of calculation is shown in Figure 7.37. The bubbles seem to move as expected: they are bounced from the partitioning wall and a great part of them leave the system driven by the buoyancy force. Only few bubbles turn around the portioning wall as observed during the experimental stage.

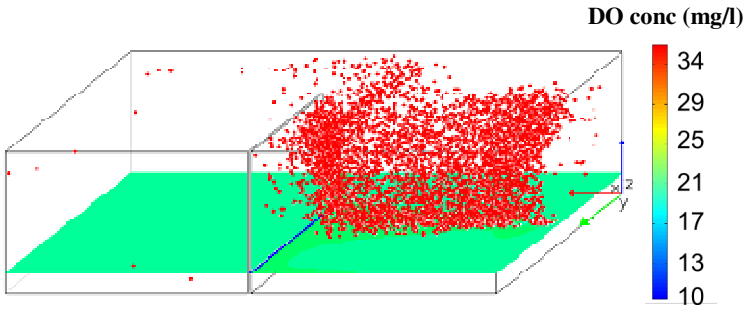

Figure 7.37 Snapshot of bubble motion and of the DO concentration at the nozzle elevation

The same bubble size distribution given as input for the simulation of the case study 1 and the mass transfer models *tm1* and *tm2* have been considered to obtain the dissolved oxygen concentration over time through the E-L model applied to the case study 2.

The comparison between numerical results and experimental measurements for the monitoring points 1b and 3b is given in Figure 7.38.

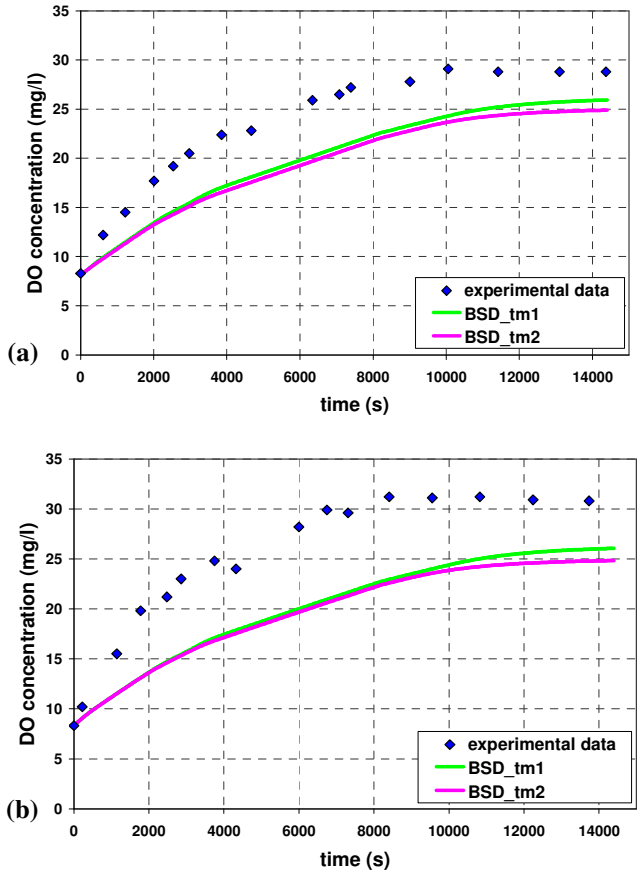

Figure 7.38 Case study 2: comparison between DO measurements (diamond markers) and numerical results (continuous line), (a) Point 1b, (b) Point 3b

Two interesting insights arise by observing Figure 7.38.

First, the numerical simulations, independently from the mass transfer model considered, lie below the experimental measurements of dissolved oxygen

concentration. The reason for this gap can be probably attributed to the bubble size distribution given as input to the numerical model, since no new BSD was obtained in this case. Particular care has been taken to reproduce the same operational conditions observed during test case 1 (gas and liquid flow rates), even though no possibility to control the environmental temperature was possible. This condition may have played an important role in the determination of the actual BSD of case study 2. Further investigations will be carried out in order to evaluate the dependencies of BSD on this external factor.

Second, the experimental configuration has proven to be unsatisfactory, as said, to ensure the formation of non-uniform concentration areas in the tank. In fact, the dimension of the experimental apparatus is likely to determine a nearly uniform concentration in a short time, even with the presence of a partitioning transversal wall which interferes with the bubbly flow and which creates low velocity regions.

7.5.3 Applicability of the complete numerical model

The results discussed in paragraph 7.5.2 on the behaviour of the system in the configuration of case study 2 prevented from the possibility to apply the complete model (including therefore also the time evolution of the concentration of biomass and substrate as dissolved oxygen concentration as well) to the case study.

It would be actually meaningless to apply the complete implemented model to this case, because the variation in time of biomass and substrate concentrations would not be affected by the concentration of dissolved oxygen in the system (which still keeps higher than the limiting value at every point of the tank) since no appreciable difference subsists among the DO concentration of the computational cells. Even starting with an non-uniform concentration of biomass and substrate, in a very short period a uniform concentration field for both of the two species would be reached.

Another problem that can be found concerns the characteristic times of the two phenomena (degradation of substrate / biomass growth and mixing inside the system) which are very different. This complicates the applicability of the model as it has been proposed, due to the computational effort required.

A significant case study, for which the geometric dimensions and the characteristics of the liquid velocity field are capable to highlight a different distribution of the dissolved oxygen concentrations in the system (both in space and time), should first be identified. This is indeed the starting point for the application of the complete model that has already been validated in of all its parts, as illustrated in the previous paragraphs of the present dissertation.

Conclusions

A "one-way coupling" E-L (Eulerian-Lagrangian) numerical model has been implemented in Fortran 90 environment in order to simulate the evolution in time of dissolved oxygen concentration (and possibly of other species) in a system mixed by a two-phase turbulent jet. The working hypothesis made possible to decouple the liquid phase and the gas phase dynamics. The velocity field that has to be provided as input to the numerical model was determined by CFD (Computational Fluid Dynamics) simulations using a finite volume method. The validation of the simulation results, for both the cases study examined, was performed by comparison with velocity measurements carried out by a 3D ADV velocimeter.

The comparison between numerical simulations and experimental velocity measurements has proved to be satisfactory with regard to the longitudinal mean velocity profiles measured at the horizontal and vertical reference locations. The turbulent kinetic energy profiles revealed, instead, a systematic overestimation of the numerical simulation results compared with the calculated values from the experimental measurements.

The qualitative analysis of the ADV raw signal showed that, despite the average SNR and correlation values of the measurement sample are in accord with the threshold quality values, slightly different results are obtained by the removal of each sample element lower than the fixed thresholds.

The application of the filtering method A (rejection of the elements of the sample that do not respect the threshold values on correlation and SNR,

application of the threshold filter based on the comparison between local and global deviation of the sample, application of the low pass filter) and of filtering method B (despiking method – elimination of the elements of the sample that do not respect the fixed threshold on correlation and SNR, despiking method) has highlighted the marked effect linked to the elimination of the nasty correlation values on the calculated turbulent kinetic energy, especially for the positions of higher velocities.

The effect of the low pass filter set to a cutoff frequency equal to the half of the sampling frequency, revealed a marked decrease in the standard deviation of the sample for higher velocities (for which also the lower correlation values are measured). For this reason, it has been hypothesised that the high frequency turbulent fluctuations that may characterize the positions closer to the jet axis are not sampled by the instrument operating at a sampling frequency of 25 Hz. Further comparison with velocity measurements made by an instrument operating at higher sampling frequency might help to better understand the relation between the standard deviations of the signal and the low correlation values, leading to a more complete critical analysis on the better filtering method to apply when the fluid is highly turbulent.

The analysis of the results of the velocity and of the concentration field of an organic dye transported by a turbulent jet discharging into a co-flowing stream simulated by means of the proposed numerical method showed a good agreement compared with the experimental literature data (Antoine at al., 2001). This result confirmed the reliability of the numerical method developed both for the simulation of the liquid velocity field (finite volume method) and for the numerical integration of the balance equation of a dissolved species. Only the eulerian part of the numerical model has been involved for the passive scalar transport simulation, hence a validation of the convective-diffusive terms has been carried out.

The comparison between the numerical results and the experimental data from literature concerning the evolution over time of the concentration of

biomass, substrate and BOD allowed the identification, by means of a regression analysis, of the kinetic constants of the Monod model. This last has been implemented within the computer code in order to predict the variation of the dissolved oxygen (DO), even after consumption by the heterotrophic biomass, and to observe the influence of the remaining dissolved oxygen concentration on the biomass growth and substrate removal.

The sensitivity analysis carried out for the case study 1, showed that, using the actual bubble size distribution (BSD), different mass transfer models lead to substantially equivalent DO concentration results over time.

In particular, the mass transfer model that differentiates the oxygen transfer on the basis of the bubble diameter (distinguishing from bubbles with rigid surface to bubbles with mobile surface) through the Ahmed and Semmens (2003) relation (*tm1*) and the transfer model that calculates the exposure time of the bubbles on the basis of the local turbulent kinetic energy dissipation rate of the flow field (*tm2*) lead to results in appreciable accord with the experimental measured DO concentration values. The prediction of the DO concentration appears to be satisfactory both for points located at monitoring positions far away from the gas stream and for those points most affected by the bubbly flow.

The sensitivity analysis on the BSD entering the system highlights the importance of an accurate determination of the BSD in order to predict the evolution of the DO concentration over time. In fact, the results obtained by adopting two different mass transfer models, *tm1* and *tm2*, but the same manipulated BSD, can lead to very far results from each other. This is particularly true for the BSDs obtained by translation of the original one towards the high and the small diameters keeping the volume fraction associated with each dimensional class unchanged.

The numerical results obtained by adopting the BSD derived through the semiautomatic detection method of high resolution digital images show a really good agreement with the results obtained by adopting the BSD derived by the manual detection method. This confirms the validity of the experimental

procedure and of the processing method adopted in order to obtain the representative distribution of the bubbly flow.

A coarser computational grid for concentrations (half refined with respect to that used for the sensitivity analysis on the mass transfer models and on the BSD) allows a reduction of about 1/8 of the computational time maintaining satisfactory results.

The application of the proposed numerical method to the case study 2, highlighted the necessity of a further investigation of the problem. In fact, the numerical results tend to underestimate the concentration values of dissolved oxygen inside the tank, appropriately reduced by placing a vertical partitioning wall perpendicular to the horizontal direction of the jet exit. The most plausible reason of the underestimation can be found in the incorrect BSD adopted as input to the E-L model for this specific case.

Indeed, although it has been given particular care in maintaining the same operating conditions that were observed during the experimental determination of the BSD (gas and liquid flow rate, positioning of the oxygen injection system, etc.), it was not possible to control the system temperature. Probably this aspect has affected the BSD characteristic of the case study 2. Moreover, both the experimental measurements and the numerical simulations have highlighted the inadequacy of the experimental apparatus to recreate a critical situation (i.e. a configuration characterized by a non-uniform oxygenation of the compartment). The small size of the experimental tank leads to the rapid mixing of the entire fluid volume, regardless of the low velocity values that are recorded in the part behind the partitioning wall which, moreover, is marginally involved by the flow of bubbles injected into the system. The application of the complete model (biomass+substrate+dissolved oxygen) to the case study 2 was therefore not carried out, although the computational code has been designed for the calculation of the evolution over time of different dissolved species, also considering the presence of several transverse baffles potentially placed inside

the computational domain. The application of the complete model to the case studies examined would have been unnecessarily burdensome in terms of computational effort because of the different time scales of the involved phenomena. Furthermore, the rapid attainment of uniform mixing conditions does not allow to highlight the different evolution of phenomenon within the regions with low velocity and don't reached from the bubbly flow.

For these reasons, in the next future, the research activity will be focused on the identification of a case study that allows the useful application of the complete numerical model, already tested in its entirety, as highlighted during the critical analysis and the several validation steps reported in the present dissertation.

In conclusion, the experimental and numerical approach developed to evaluate the evolution of the dissolved oxygen concentration during a transient inside a confined environment equipped with a two-phase turbulent jet system has shown several positive aspects, even if some phenomena have to be investigated more deeply.

In particular, the numerical procedure developed (FV simulation of the fluid flow + BSD + E-L model) based on a "one-way coupling" method seems to be satisfactory to predict the evolution of the concentration field over time, without involving a more detailed description of the interactions that actually take place between the bubbles and the liquid phase. It must also be observed that even if the number of total parameters required by the model is limited, the sensitivity of the model to the BSD given as input and to the mass transfer model considered can be of appreciable magnitude if not sufficient care is paid during each needed step.

Because of the multifaceted nature both of the problem and of the numerical approach that has been developed for its simulation, some issues still remain open and will require further investigation. Future research will be hopefully able to clarify these aspects.

References

Abramovich G. N. (1963). *The theory ofturbulent jets*, Eng. trans. pub. by M.I.T. Press, Massachusetts.

Ahmed T. and Semmens M. J. (2003). "*Gas transfer from small spherical bubbles in natural and industrial systems*", Journal of Environmental System, vol. 29(2), 101-123.

Albertson M. L., Dai y. B., Jensen R. A., Rouse H. (1950). "*Diffusion of submerged jets*", Trans. A.S.C.E., vol. 115, 639-697.

Alves S. S., Vasconcelos J. M. T., Orvalho S. P. (2006). "*Mass transfer to clean bubbles at low turbulent energy dissipation*", Chemical Engineering Science, vol. 61, 1334-1337.

Antoine Y., Lemoine F., Lebouché M. (2001). "*Turbulent transport of a passive scalar in a round jet discharging into a co-flowing stream*", European Journal of Mechanics - B/Fluids, vol. 20, 275-301.

Benefield L. D. and Randall C. W. (1980). *Biological Process Design for Wastewater Treatment*, Prentice-Hall, Inc., Englewood Cliffs, N. J..

Bertuzzi C. (A. A. 2008/2009). *Metodo Euleriano–Lagrangiano per il calcolo della concentrazione di ossigeno disciolto in un sistema a getti turbolenti*, Tesi di Laurea - Università degli Studi di Pavia.

Billet M. L. (1985). "*Cavitation nuclei measuremennts: A review*", In: Procedings of cavitation and multiphase flow forum ASME - Albuquerque N.M., 31-38.

Calderbank P. H. and Moo-Young M. B. (1961). "*The continuous phase heat and mass transfer properties of dispersions*", Chemical Engineering Science, vol. 16, 39-54.

Carpenter J. H. (1966). "*New measurements of oxygen solubility in pure and natural water*", Limnol. Oceanogr, vol. 11, 264-277.

Chanson H., Trevethan M., Aoki S. (2008). "*Acoustic Doppler velocimetry (ADV) in small estuary: Field experience and signal post-processing*", Flow Measurement and Instrumentation, vol. 19, 307-313.

Chapman T. D., Matsch L. C., Zander E. H. (1976). "*Effect of High Dissolved Oxygen Concentration in Activated Sludge Systems*", Journal (Water Pollution Control Federation), vol. 48(11), 2486-2510.

Chigier N. (1991). "*Optical imaging of sprays*", Progress in Energy and Combustion Science, vol. 17, 211-262.

Cigognetti A. (A. A. 2007/2008). *Misura dell'ossigeno disciolto e della distribuzione dimensionale delle bolle in un sistema di miscelazione e aerazione a getto*, Tesi di Laurea - Università degli Studi di Pavia.

Coulson J. M. and Richardson J. F. with Backhurst J. R. and Marker J. H. (1999). Coulson & Richardson's Chemical Engineering - *Fluid Flow, Heat Transfer and Mass Transfer*, Butter worth -Heinemann, Linacre House, Jordan Hill, Oxford.

Crowe C. T., Troutt R., Chung J. N. (1996). "*Numerical model for two-phase turbulent flows*", Annual Review of fluid mechanics, 11-43.

Cussler E. L. (2009*). Diffusion - Mass transfer in Fluid Systems*, Cambridge University Press, New York.

Danckwerts P. V. (1951). "*Significance of Liquid-Film Coefficients in Gas Absorption*", Industrial and Engineering Chemistry, vol. 43(6), 1460-1467.

Darmana D., Deen N. G., Kuipers J. A. M. (2005). "*Detailed modeling of hydrodynamics, mass transfer and chemical reactions in a bubble column using a discrete bubble model*", Chemical Engineering Science, vol. 60, 3383-3404.

Davis M.R. and Winarto H. (1980). "*Jet diffusion from a circular nozzle above a solid plane*", Journal of Fluid Mechanics, vol. 101, 201-221.

Delnoij E., Lammers F. A., Kuipers J. A. M., van Swaaij W. P. M. (1997). "*Dynamic simulation of dispersed gas-liquid two-phase flow using a discrete bubble model*", Chemical Engineering Science, vol. 52(9), 1429-1458.

Dukhin S. S., Miller R., Loglio G. (1998). *Physico-chemical hydrodynamics of rising bubble*, In: Möbius, D., Miller, R. (Eds.), Studies in Interface Science. Drops and Bubbles in Interfacial Research. Elsevier Science.

Fayolle Y.,Cockx A., Gillot S., Roustan M., Heduit A. (2007). "*Oxygen transfer prediction in aeration tanks using CFD*", Chemical Engineering Science, vol. 62, 7163-7171.

Fick A. (1855). "*Ueber diffusion*", Poggendorff's Annalen der Physik und Chemie, vol. 94, 59-86.

Frössling N. (1938). "*Über die Verdunstung fallender Tropfen*", Gerlands Beitr. Geophys., vol. 52, 170-216.

Frumkin A. and Levich V.G. (1947). "*On surfactants and interfacial motion*", Zh. Fizicheskoi Khimii, vol. 21, 1183-1204.

Garberi M. (A. A. 2010/2011). *Campo di moto indotto da un getto turbolento: misure ADV e analisi del segnale*, Tesi di Laurea - Università degli Studi di Pavia.

Goertler H. (1942). "*Berechnung von Aufgaben der freien turbulenz auf Grund eines neuen Naherungsansatzes*", Z.A.M.M., vol. 22, 244-254.

Gong X. , Takagi S., Huang H., Matsumotoa Y. (2007). "*A numerical study of mass transfer of ozone dissolution in bubble plumes with an Euler–Lagrange method*", Chemical Engineering Science, vol. 62, 1081-1093.

Gonzalez R.C., Woods R.E., Eddins S.L. (2004). *Digital image processing using MATLAB* ®, Upper Saddle River: Pearson.

Goring D. G. and Nikora V. I. (2002). "*Despiking Acoustic Doppler Velocimeter Data*", Journal of Hydraulic Enginnering, vol. 128(1), 117-126.

Gouesbet G. and Berlemont A. (1999). "*Eulerian and Lagrangian approaches for predicting the behaviour of discrete particles in turbulent flows*", Progress in Energy and Combustion Science, vol. 25, 133-159.

Higbie R. (1935). "*The rate of absorption of a pure gas into a still liquid during short periods of exposure*", American Institute of Chemical Engineering, vol. 31, 365-389.

Hinze J. O. and Zijnen B. G. Van der Hegge (1949). "*Transfer of heat and matter in the turbulent mixing zone of an axially symmetrical jet*", Journal of Applied Science Research, vol. A1, 435-461.

Huang W., Wu C., Xia W. (2009). "*Oxygen transfer in high-speed surface aeration tank for wastewater treatment: full-scale test and numerical modeling*", Journal of environmental engineering, vol. 135(8), 684-691.

Invernizzi J. (A. A. 2009/2010). *Impiego e taratura di un metodo ottico per la misura della distribuzione dimensionale delle bolle in un getto turbolento bifase acqua ossigeno*, Tesi di Laurea - Università degli Studi di Pavia.

Iwa Task Group on Mathematical Modelling of Design and Operation of Biological Wastewater Treatment (2000). *Activated Sludge Models ASM1, ASM2, ASM2D and ASM3 - Scientific and Technical Report*, Iwa Publishing, London.

Jayanti S. (2001). "*Hydrodynamics of jet mixing in vessels*", Chemical Engineering Science, vol. 56, 193-210.

Kalinske A. A. (1976). "*Comparison of air and oxygen activated sludge systems*", Journal (Water Pollution Control Federation), vol. 48(11), 2472-2485.

Kawase Y., Halard B., Moo-Young M. (1987). "*Theoretical prediction of volumetric mass transfer coefficients in bubble columns for Newtonian and non-Newtonian fluids*", Chemical Engineering Science, vol. 42, 1609-1617.

Khorsandi B., Mydlarski L., Gaskin S. (2009). "*A laboratory study of noise in turbulence measurements using acoustic Doppler velocimetry*", In: Proceedings of 33rd IAHR Congress: Water Engineering for a Sustainable Environment - Vancouver, British Columbia, 3551-3557.

Kleinstreuer C. (2003). *Two-phase flow: theory and applications*, Taylor & Francis.

Koku H., Eroglu I., Gunduz U., Yucel M., Turker L. (2003). "*Kinetics of biological hydrogen production by the photosynthetic bacterium Rhodobacter*

sphaeroides O.U. 001", International Journal of Hydrogen Energy, vol. 28(4), 381-388.

Krishna R. and van Baten J. M. (2003). "*Mass transfer in bubble columns*", Catalysis Today, vol. 79-80, 65-75.

Kulkarni A. A. (2007). "*Mass Transfer in Bubble Column Reactors: Effect of Bubble Size Distribution*", Industrial and Engineering Chemistry Research, vol. 46, 2205-2211.

Kulkarni A. A. and Joshi J. B. (2005). "*Bubble formation and bubble rise velocity in gas-liquid systems: a review*", Industrial & Engineering Chemistry Research, vol. 44, 5873-5931.

Laakkonen M., Moilanen P., Alopaeus V., Aittamaa J. (2007). "*Modelling local bubble size distributions in agitated vessels*", Chemical Engineering Science, vol. 62, 721-740.

Lain S., Bröder D., Sommerfeld M., Göz M. F. (2002). "*Modelling hydrodynamics and turbulence in a bubble column using the Euler-Lagrange procedure*", International Journal of Multiphase Flow, vol. 28, 1381-1407.

Lamont J. C. and Scott D. S. (1970). "*An eddy cell model of mass transfer into surface of a turbulent liquid*", AIChE Journal, vol. 16, 513-519.

Lapin A. and Lübbert A. (1994). "*Numerical simulation of the dynamics of the two-phase gas-liquid flows in bubble columns*", Chemical Engineering Science, vol. 49(21), 3661-3674.

Launder, B.E. and Spalding, D.B. (1974). "*The numerical computation of turbulent flows*", Computer Methods in Applied Mechanics and Engineering, vol. 3, 269-289.

Le Moullec Y., Potier O., Gentric C., Leclerc J. P. (2008). "*Flowfield and residence time distribution simulation of a cross-flow gas–liquidwastewater treatment reactor using CFD*", Chemical Engineering Science, vol. 63, 2436-2449.

Lehr F., Millies M., Mewes D. (2002). "*Bubble-size distributions and flow fields in bubble columns*", Fluid mechanics and transport phenomena, vol. 48(11), 2426-2443.

Lide D. R. and Frederikse H. P. R. (1995). *CRC Handbook of Chemistry and Physics*, CRC Press, Inc., Boca Raton.

Lima Neto I. E., Zhu D. Z., Rajaratnam N. (2008). "*Horizontal injection of gas–liquid mixtures in a water tank*", Journal of Hydraulic Engineering, vol. 134(12), 1722-1731.

Linek V., Kordač M., Moucha T. (2005). "*Mechanism of mass transfer from bubbles in dispersions - Part II: Mass transfer coefficients in stirred gas–liquid reactor and bubble column*", Chemical Engineering and Processing, vol. 44, 121-130.

Linton M. and Sutherland K. L. (1957). "*Dynamic surface forces, drop circulation and liquid–liquid mass transfer*", Second International Congress on Surface Activity, Butterworth - London, vol. 1, 494-501.

Lohrmann A., Cabrera R. and Kraus N.C. (1994). "*Acoustic Doppler velocimeter (ADV) for laboratory use*", In: Proceedings of Symposium On Fundamentals and Advancements in Hydr. Measurements and Experimentation, C. A. Pugh, ed.ASCE, 351-365.

Loomis A. G. (1928). *Solubilities of gases in water*, In: E. W. Washburn, C. J.West, N. E. Dorsey, F. R. Bichowsky, and A. Klemenc, editors, International Critical Tables of Numerical Data, Physics, Chemistry and Technology - McGraw Hill.

Martìn M. J., Burguillo F. J., Bardsley W. G. (2009). "*Modelling the simultaneous processes occurring during the BOD5 test using synthetic waters as a pattern*", Bioprocess Biosyst Engineering, vol. 32, 207-216.

McGinnis D. F. and Little J.C. (2002). "*Predicting diffused-bubble oxygen transfer rate using the discrete bubble model*", Water Research, vol. 36, 4627-4635.

Metcalf & Eddy (2006). *Ingegneria delle acque reflue - Trattamento e riuso*, McGraw-Hill

Mewes D. and Wiemann D. (2003). "*Two-phase flow with mass transfer in bubble columns*", Chemical Engineering Technology, vol. 26(8), 862-868.

Michaelis L. and Menten M. L. (1913). "Die *kinetik der invertinwirkung*", Biochem. Z, vol. 49, 333-369.

Monod J. (1949). "*The growth of bacterial coltures*", Annual review of microbiology, vol. 3, -371.

Morchain J., Maranges C., Fonade C. (2000). "*CFD modelling of a two-phase jet aerator under influence of a crossflow*", Water Research, vol. 34(13), 3460-3472.

Motarjemi M. and Jameson G. J. (1978). "*Mass transfer from very small bubbles the optimum bubble size for aeration*", Chemical Engineering Science, vol. 33, 1415-1423.

Newman B. G., Patel R. P., Savage S. B. and Tjio H. K. (1972). "*Three dimensional wall jet originating from a circular orifice*", Aero. Quart., vol. 23, 188-200.

Nikora V. I. and Goring D. G. (1998). "*ADV Measurements of Turbulence: Can We Improve Their Interpratation?*", Journal of Hydraulic Enginnering, vol. 124(6), 630-634.

Patwardhan A. W. (2002). "*CFDmodeling of jet mixed tanks*", Chemical Engineering Science, vol. 57, 1307-1318.

Pfleger D. and Becker S. (2001). "*Modelling and simulation of the dynamic flow behaviour in a bubble column*", Chemical Engineering Science, vol. 56, 1737-1747.

Prasher B. D. and Wills G. B. (1973). "*Mass transfer in an agitated vessel*", Industrial and Engineering Chemistry Process Design and Development, vol. 12, 351-354.

Raboni M. (2010). *Impiego di tecniche numeriche e sperimentali per l'analisi di fenomeni multiphysics*, PhD Thesis - Università degli Studi di Pavia.

Rainer B., Fonade C., Moser A. (1995). "*Hydrodynamics of a new type of ejector*", Bioprocess Engineering, vol. 13(2), 97-103.

Rajaratnam N. (1976). *Turbulent jets*, Developments in water science - Elsevier Sc. Publishing Co., Amsterdam and New York.

Ratulowski J. And H. C. Chang (1990). "*Marangoni effects of trace impurities on the motion of long gas bubbles in capillaries*", Journal of Fluid Mechanics.

Reichardt H. (1942) (second edition: 1951). "*Gesetzmassigkeiten der freien Turbulenz (Similarity in free turbulence)*", VDI-Forschungsh, vol. 414.

Reid R. C., Prausnitz J. M., Poling B. E. (1987). *The Properties of gases & liquids*, McGraw-Hill.

Sander R. (1999). "*Compilation of Henry's Law Constants for Inorganic and Organic Species of Potential Importance in Environmental Chemistry*", http://www.mpch-mainz.mpg.de/~sander/res/henry.html.

Schiller L. and Naumann Z. A. (1935). "*A drag coefficient correlation*", Z. Ver. Deutsch Ing., vol. 77, 318-320.

Sibilla S. and Raboni M. (2008). "*Indagine preliminare sulla miscelazione mediante getti turbolenti in ambienti confinati*", In: Procedings of 31° Convegno Nazionale di Idraulica e Costruzioni Idrauliche, Perugia, Italy.

Sokolichin A., Eigenberger G., Lapin A. (2004). "*Simulation of buoyancy driven bubbly flow: established simplifications and open questions*", Fluid mechanics and transport phenomena, vol. 50(1), 24-45.

Tang Y.L. (2008). "*Detects multiple disks (coins) in an image using Hough Transform*", Matlab® script available at Matlab Central http://www.mathworks.com/matlabcentral/index.html.

Tollmien W. (1926). "*Berechnung Turbulenter Ausbreitungsvorgiinge Z.*", Angew. Math. Mech., vol. 6, 468-478.

Vasconcelos J. M. T., Orvalho S. P., Alves S. S. (2002). "*Gas–Liquid Mass Transfer to Single Bubbles: Effect of Surface Contamination*", Fluid Mechanics and Transport Phenomena, vol. 48(6), 1145-1154.

Vasconcelos J. M. T., Rodrigues J. M. L., Orvalho S. C. P., Alves S. S., Mendes R. L., Reis A. (2003). "*Effect of contaminants on mass transfer coefficients in bubble column and airlift contactors*", Chemical Engineering Science, vol. 58, 1431-1440.

Voulgaris G. and Trowbridge J.H. (1998). "*Evaluation of the acoustic Doppler velocimeter (ADV) for turbulence measurements*", Journal of Atmospheric and Oceanic Technology, vol. 15, 272-289.

Welty J. R., Wicks C. E., Wilson R. E. (1984). *Fundamentals of Momentum, Heat, and Mass Transfer*, John Wiley & Sons, New York.

Whitman W. G. (1923). "*The Two-Film Theory of Gas Absorption*", Chemical and Metallurgical Engineering, vol. 29(4), 146-148.

Wiemann D. and Mewes D. (2005). "*Calculation of flow fields in two and three-phase bubble columns considering mass transfer*", Chemical Engineering Science, vol. 60, 6085-6093.

Wilhelm E., Battino R., Wilcock R. J. (1977). "*Low-pressure solubility of gases in liquid water*", Chem. Rev., vol. 77, 219-262.

Wilke C. R. and Chang P. (1955). "Correlation *of diffusion coefficients in dilute solutions*", A.E.CH.E. Journal, vol. 1, 264-270.

Wüest A., Brooks N. H., Imboden D. M. (1992). "*Bubble plume modeling for lake restoration*", Water resources research, vol. 28(12), 3235-3250.